Beate Klinger, Bakk.techn.

Lunar gravity field recovery: GRAIL simulations and real data analysis

MASTERARBEIT

zur Erlangung des akademischen Grades

Diplom-Ingenieur/in

Masterstudium Geomatics Science

Technische Universität Graz

Betreuer:

Dr.-Ing. Oliver Baur
Univ.-Prof. Dr.-Ing. Torsten Mayer-Gürr

Institut für Theoretische Geodäsie und Satellitengeodäsie

Graz, Juli 2013

Acknowledgements

First of all, I would like to thank my supervisor, Dr.-Ing. Oliver Baur, for suggesting the topic of this thesis and offering me the opportunity to work at the Space Research Institute of the Austrian Academy of Sciences. He provided me direction and supervision of my scientific work and gave me support with solving all the upcoming problems.

I also would like to thank my second supervisor, Univ.-Prof. Dr.-Ing. Torsten Mayer-Gürr, for providing me the GROOPS software package and helping me with all questions concerning the adaption of the software for the purpose of simulating and processing GRAIL data. I want to appreciate his great input and patience with solving a variety of problems.

These two people stand representative for the staff at the Space Research Institute and the Institute of Satellite Geodesy and Theoretical Geodesy, who made the accomplishment of this master thesis possible.

Further, I am also very grateful to my partner Daniel, who has been very supportive throughout the whole time.

And last but definitely not least, I would like to thank my parents and family for giving me the opportunity to complete my studies and for their great support during the past years.

Deutsche Fassung:
Beschluss der Curricula-Kommission für Bachelor-, Master- und Diplomstudien vom 10.11.2008
Genehmigung des Senates am 1.12.2008

EIDESSTATTLICHE ERKLÄRUNG

Ich erkläre an Eides statt, dass ich die vorliegende Arbeit selbstständig verfasst, andere als die angegebenen Quellen/Hilfsmittel nicht benutzt, und die den benutzten Quellen wörtlich und inhaltlich entnommenen Stellen als solche kenntlich gemacht habe.

Graz, am ……. ……..
(Unterschrift)

Englische Fassung:

STATUTORY DECLARATION

I declare that I have authored this thesis independently, that I have not used other than the declared sources / resources, and that I have explicitly marked all material which has been quoted either literally or by content from the used sources.

……. ……..
date (signature)

Abstract

The NASA mission GRAIL (Gravity Recovery and Interior Laboratory) makes use of low-low Satellite-to-Satellite Tracking (ll-SST) between the two spacecraft GRAIL-A and GRAIL-B to determine a high-resolution gravity field solution of the Moon. The mission concept is inherited from the GRACE project, a space-gravimetry mission mapping the terrestrial gravity field.
Since the Moon is in synchronous rotation with the Earth, direct tracking of satellites on the far-side is impossible, but GRAIL provides global coverage of inter-satellite tracking data. Furthermore, ll-SST observations are much more sensitive to gravitational features than ground-based orbit tracking. Therefore, compared to previous missions, GRAIL enables a more accurate estimation of the lunar gravity field. The accurate knowledge of the lunar nearside and farside gravity is essential to improve the understanding of the Moon's interior structure and its thermal evolution.

Based on simulated orbit positions and ll-SST observations a series of sensitivity studies was conducted. From the simulated observations the spherical harmonic coefficients, which represent the lunar gravity field, are estimated using an integral equation approach. This approach is based on the solution of Newton's equation of motion, formulated as a boundary value problem.

Furthermore, three months of real data are analyzed to derive a preliminary lunar gravity field model from GRAIL ll-SST measurements. Since the real data analysis done in this work does not include orbit determination, the GRAIL orbits provided by NASA's PDS (Planetary Data System) have been used.
The availability of global inter-satellite tracking data improves the spatial and spectral resolution of both the lunar nearside and farside compared to the reference gravity field model JGL165P1. Importantly, the GRAIL mission enables the estimation of a high-resolution gravity field model without any regularization.

Observation simulation and parameter estimation is accomplished using the GROOPS (Gravity Recovery Object Oriented Programming System) software package. Within the framework of this thesis the software has been adapted for the purpose of simulating GRAIL observations and processing GRAIL real data.

Kurzfassung

GRAIL (Gravity Recovery and Interior Laboratory) ist eine Satellitenmission der NASA, bestehend aus den beiden Satelliten GRAIL-A und GRAIL-B, welche den Erdmond umkreisen. Ziel der Mission ist die Bestimmung eines hochauflösenden lunaren Schwerefeldmodells aus den relativen Distanzänderungen zwischen den beiden Satelliten (low-low Satellite-to-Satellite Tracking (ll-SST) Prinzip). Das Missions-Konzept wurde von der GRACE-Mission, ein Projekt zur genauen Bestimmung des Erdschwerefeldes, übernommen.
Aufgrund der gebundenen Rotation zwischen Erde und Mond können Satelliten, welche sich auf der erdabgewandten Seite befinden, nicht direkt beobachtet werden. Mit Hilfe der ll-SST Beobachtungen kann allerdings eine globale Datenabdeckung des Mondes erreicht werden. Des Weiteren sind Relativmessungen weitaus sensitiver als erdgebundene Orbitbeobachtungen. Daher ermöglicht GRAIL im Vergleich zu bisherigen Mondmissionen die Schätzung eines räumlich und spektral weitaus hochauflösenderen Schwerefeldes. Die genaue Kenntnis des lunaren Schwerefeldes soll Aufschlüsse über den inneren Aufbau des Mondes und dessen thermaler Evolution geben.

Basierend auf simulierten Orbit und ll-SST Beobachtungen wurde eine Reihe von Sensitivitätsstudien durchgeführt, um den Einfluss unterschiedlicher Parameter zu untersuchen.
Mit Hilfe der simulierten Daten können die Potentialkoeffizienten eines lunares Schwerefeldmodells anhand des Integralgleichungsansatzes bestimmt werden. Dieser Ansatz basiert auf einer als Randwertaufgabe formulierten Lösung der Newton-Euler Bewegungsgleichung.

Neben den Simulationsstudien wurden auch Realdaten über einen Zeitraum von drei Monaten verwendet um ein Mondschwerefeldmodell zu schätzen. Da die Orbitbestimmung nicht Teil der Realdatenanalyse dieser Arbeit ist, werden die vom NASA PDS (Planetary Data System) zur Verfügung gestellten GRAIL Orbits verwendet.
Im Vergleich zu früheren Schwerefeldlösungen sind deutliche Verbesserungen sowohl auf der erdabgewandten, als auch auf der erdzugewandten Seite erkennbar. Diese Verbesserungen sind auf die globale Abdeckung der ll-SST Beobachtungen zurückzuführen. Ein weiterer wesentlicher Aspekt der globalen Datenverfügbarkeit besteht darin, dass für die Lösung des Ausgleichs keine Regularisierung notwendig ist.

Die Simulation und Auswertung der Beobachtungsdaten erfolgt mit Hilfe des Softwarepakets GROOPS (Gravity Recovery Object Oriented Programming System). Die Software wurde im Rahmen dieser Masterarbeit entsprechend erweitert, um die Simulation und die Analyse von GRAIL Daten zu ermöglichen.

Contents

Chapter 1

Introduction

1.1 Motivation

During history, the Moon, our closest neighbour in the solar system, always fascinated people and has been studied extensively. In 1609, Galileo Galilei drew one of the first pictures of the Moon's nearside using a telescope. He noted for the first time that the lunar surface was not smooth, but has visible features like mountains and craters. Direct lunar exploration began in 1959 when the farside was observed for the first time by the unmanned Russian Luna 3 mission, which orbited the Moon and took images of the lunar surface. The gravity field of the Moon was fist investigated in 1966 by the Russian Luna 10 mission, which first orbited the Moon (Akim, 1966). The discovery of mass concentrations (mascons) [1] from the Lunar Orbiter Doppler data was the first evidence of medium-wavelength gravity field variations on the Moon (Muller and Sjogren, 1968). Mascons, which are mainly found on the nearside, are significant positive gravity anomalies associated with areas of high density under rigid lowland maria [2]. They contain information about the impact processes leading to mascon formations and possibly contain information about the Moon's early thermal history. Besides, they were of immense practical importance during the Apollo missions.
On July 20, 1969 the NASA (National Aeronautics and Space Administration) mission Apollo 11 landed the first humans, the two astronauts Neil Armstrong and Edwin Aldrin, on the lunar surface. During NASA's Apollo program between 1969 and 1972 six manned landings on the lunar surface succeeded.

Satellite techniques enable scientists to use measurements from satellites to recover the lunar gravity field or to pursue other scientific purposes. Recent missions such as Lunar Prospector (LP), Chang'e 1 & 2 and Lunar Reconnaissance Orbiter (LRO) provide lunar gravity field estimates with a relatively high resolution compared to previous models. But there is still room for improvement; not only due to the lack of farside data, but also due to the sensitivity of orbit tracking data.

[1] A mass concentration (or mascon) describes a geologic structure that has a large positive gravitational anomaly associated with a feature that would have been expected to have a negative anomaly.

[2] The lunar maria (singular: mare) are large, dark, basaltic plains on the lunar surface formed by ancient volcanic eruptions. The plains were named maria, derived from the Latin word for seas, by early astronomers who mistook them for actual seas. The maria cover about 16 percent of the lunar surface and can be found mainly on the nearside.

LP achieved an improvement of the nearside gravity field by using a circular polar orbit with a low 100 km altitude (Konopliv et al., 1998). The Japanese Selenological and Engineering Explorer (SELENE) mission improved the farside gravity field of the Moon by using a relay subsatellite (Namiki et al., 2009). An extract of historic and recent lunar missions is listed in Table 1.1.

The Moon is the only natural satellite of the Earth and is compared to the size of the Earth the largest natural satellite in the solar system. To planetary science the Moon is significant, because it keeps the historical record of the solar system due to the lack of geological activities on the Moon.
As the Moon and the Earth are in a spin-orbit resonance, always the same side of the Moon (nearside) faces the Earth. Due to the synchronous rotation the Earth-based tracking of satellites orbiting the Moon is limited. Therefore, no direct radio tracking is possible if satellites fly over the lunar farside and are not in view from Earth. The lack of direct farside tracking makes the use of a-priori constraints (regularization) during the estimation process necessary. Therefore, most lunar gravity field models use a scaled Kaula rule to fit the gravity field over the farside (Floberghagen, 2002).

Now the following questions arise: How can the Gravity Recovery and Interior Laboratory (GRAIL) mission improve the lunar gravity field? And how can studying the lunar gravity field improve the knowledge about the Moon?

First of all, GRAIL provides global data coverage and improves the nearside and farside gravity field solution by the availability of global low-low Satellite-to-Satellite tracking data (cf. Chapter 8). For the first time ever (in planetary science) high-accurate and high-sensitive relative measurements are provided compared to pure orbit tracking data. GRAIL enables the recovery of the most accurate gravity field model of the Moon to date, which will improve the understanding of the Moon's interior structure and thermal evolution.
The combination of the high-resolution lunar gravity field with a topographical map allows conclusions to be drawn about the interior structure and composition of the Moon. Besides, it improves the understanding of the thermal evolution, the history of the Moon's heating and cooling, which gives insight into the Moon's origin and development. Furthermore, the gained knowledge could be extended to other rocky planets in the inner solar system: Mercury, Venus, Earth and Mars. GRAIL will help to reconstruct their evolutionary history.

Moreover, the accurate knowledge of the lunar gravity field will be an invaluable navigational aid for future lunar missions.

Table 1.1: Overview of past and recent lunar missions

Year	Mission	Country	Comment
1959	Luna 1	RUS	first flyby
1959	Luna 3	RUS	first pictures of the farside
1966	Luna 10	RUS	first lunar orbiter
1968	Apollo 8	USA	first manned lunar orbiter
1969	Apollo 11	USA	first manned landing on the lunar surface
1971	Apollo 15	USA	first manned lunar rover
1998	Lunar Prospector	USA	
2007	SELENE (Kaguya)	Japan	
2007	Chang'e 1	China	
2009	LRO	USA	ongoing
2010	Chang'e 2	China	
2011	GRAIL	USA	decommissioned

1.2 Concept of ll-SST

One of the measurement techniques used in satellite geodesy is the so-called "Satellite-to-Satellite Tracking (SST)", which is part of the Space-to-Space techniques. SST uses satellites to track other satellites; basically two types of SST are distinguished (cf. Figure 1.1):

- High-low Satellite-to-Satellite Tracking (hl-SST)
- Low-low Satellite-to-Satellite Tracking (ll-SST)

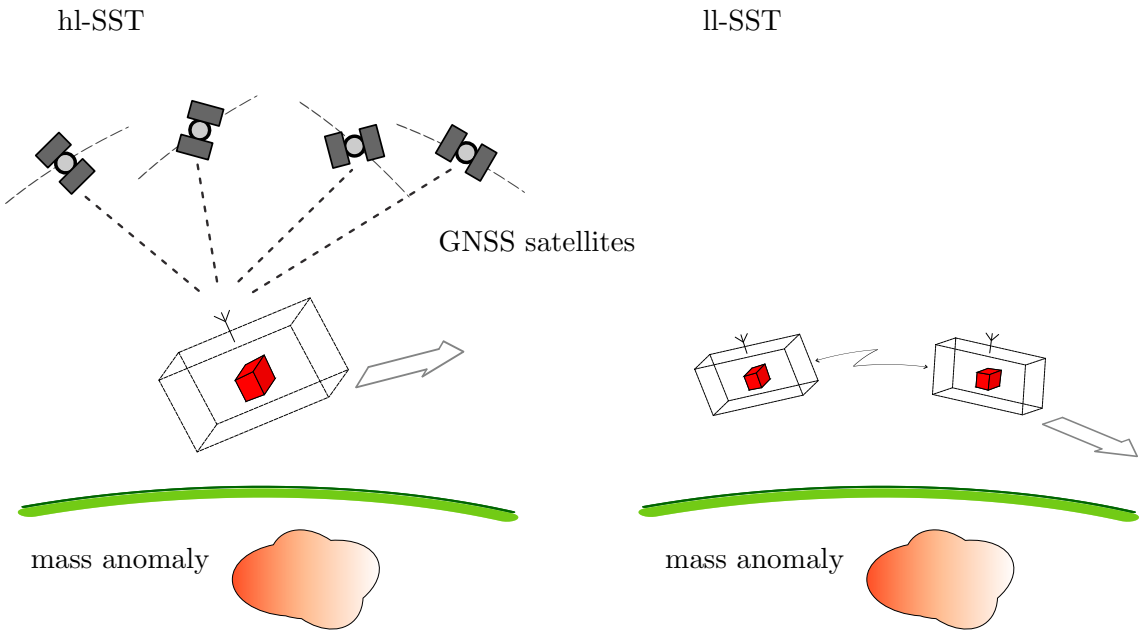

Figure 1.1: Concept of hl-SST and ll-SST

High-low Satellite-to-Satellite Tracking

The orbit of a low altitude spacecraft is determined using several high altitude satellites with accurately known orbits, such as GNSS (Global Navigation Satellite System) satellites, in case of the Earth.
In planetary science the SELENE mission used a relay-satellite to determine the orbit of the spacecraft on the lunar farside via Doppler tracking.

Low-low Satellite-to-Satellite Tracking

Two satellites are placed in the same orbit with a separation up to a few hundreds of kilometers. The changes in the relative distance between the two spacecraft are caused by irregularities in the gravity field and can be measured by an on-board ranging system.

The GRACE (Gravity Recovery And Climate Experiment) mission combines both techniques to determine the Earth's gravity field from continuous GPS (Global Positioning System) orbit tracking data (hl-SST) and inter-satellite tracking data (range, range rates and range accelerations; ll-SST). The successful GRACE concept can be transferred to GRAIL if some necessary adjustments are made (cf. Table 1.2, for details on GRAIL refer to Chapter 2). Since there is no GPS-tracking available, the spacecraft orbit on the nearside is determined using Earth-based Doppler tracking via the Deep Space Network (DSN).

GRAIL is the first lunar mission using the ll-SST concept, hence some advantages to previous missions (cf. Table 1.1) arise:

- Global data coverage (inter-satellite tracking data)
- More accurate Ka-band ranging measurements compared to ground-based orbit tracking
- Estimation of a high-resolution gravity field without regularization due to the availability of farside data

Table 1.2: Comparison - GRAIL vs. GRACE

	GRAIL	GRACE
	Mission Overview	
Operator	NASA	NASA, DLR
Launch	10-Sept-2011	17-March-2002
Launch site	Cape Canaveral (USA)	Plesetsk (RUS)
Mission status	decommissioned	active
	Orbit characteristics	
Orbital period	113 min	94.5 min
Altitude	∼55 km (± 35 km)	450-500 km
Inclination	89.9° w.r.t lunar equator	89°
Separation distance	82-218 km	∼220 km
	Payload	
Microwave ranging system	Ka-Band (32 GHz)	K-Band (24 GHz) and Ka-Band (32 GHz)
Orbit determination	Doppler Tracking via the Deep Space Network (DSN)	Global Positioning System (GPS)
Accelerometer	—	to measure non-gravitational forces
Time Transfer System (TTS)	to replace the GPS timing functionality	—

Chapter 2

GRAIL

2.1 Mission overview

The NASA mission GRAIL makes use of low-low Satellite-to-Satellite Tracking between two twin spacecraft to determine a high-resolution gravity field solution of the Moon. The two spacecraft GRAIL-A (Ebb) and GRAIL-B (Flow) were launched from the Cape Canaveral Air Force (CCAF) Station in Florida (USA) on 10^{th} September 2011 on-board a Delta II launch vehicle.

The mission concept is inherited from the GRACE project, a space gravimetry mission mapping the terrestrial gravity field (cf. Table 1.2). The two spacecraft are placed into the same orbit around the Moon and measure the changes in their relative motion very precisely. Since the orbit is perturbed by the gravity field of the Moon, areas of greater and lesser density cause variations in the relative distance and the spacecraft will move slightly toward and away from each other. If one of the probes flies over an area of greater density, caused by surface features such as mountains, mass concentrations (mascons) and craters or by masses hidden beneath the lunar surface, the attraction increases and the relative distance changes accordingly.

Since the Moon is in synchronous rotation with the Earth, direct (radio) tracking of the satellites on the farside is impossible, but GRAIL provides global coverage of inter-satellite tracking data. Furthermore, ll-SST observations are much more sensitive to gravitational features than ground-based orbit tracking. Therefore, compared to previous missions, GRAIL enables a more accurate estimation of the lunar gravity field, with a much higher spectral and spatial resolution.

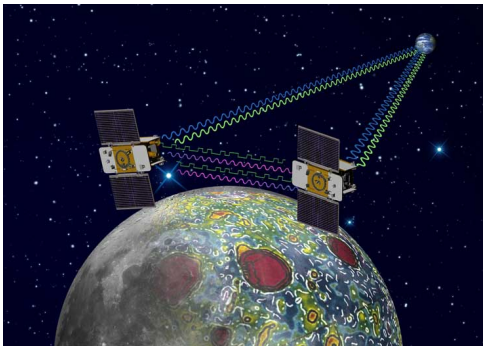

Figure 2.1: GRAIL satellite configuration and measurement principle (Source: NASA)

2.1.1 Science objectives

The accurate knowledge of the lunar nearside and farside gravity is essential to improve the understanding of the Moon's interior structure and its thermal evolution.

"These objectives will be accomplished by implementing the following lunar science investigations:

1. Map the structure of the crust and lithosphere.
2. Understand the Moon's asymmetric thermal evolution.
3. Determine the subsurface structure of impact basins and the origin of mascons.
4. Ascertain the temporal evolution of crustal brecciation and magmatism.
5. Constrain deep interior structure from tides.
6. Place limits on the size of the possible inner core." (Zuber et al., 2008, p.1)

Furthermore, the knowledge gained on the internal structure and thermal evolution of the Moon should be extended to other terrestrial planets in the inner solar system to improve the understanding of their evolution as well (Hoffman et al., 2010; Zuber et al., 2008).

2.2 Mission design

2.2.1 Spacecraft & payload

The two spacecraft GRAIL-A and GRAIL-B, named Ebb and Flow, are nearly identical. The main structure and propulsion systems of the Lockheed-Martin built spacecraft are based on the Experimental Small Satellite (XSS-11) bus. Other parts of the spacecraft are inherited from the Mars Reconnaissance Orbiter (MRO). The GRAIL spacecraft have a rectangular structure with a fully fuelled mass of about 307 kilograms. The spacecraft are shown in Figure 2.2.

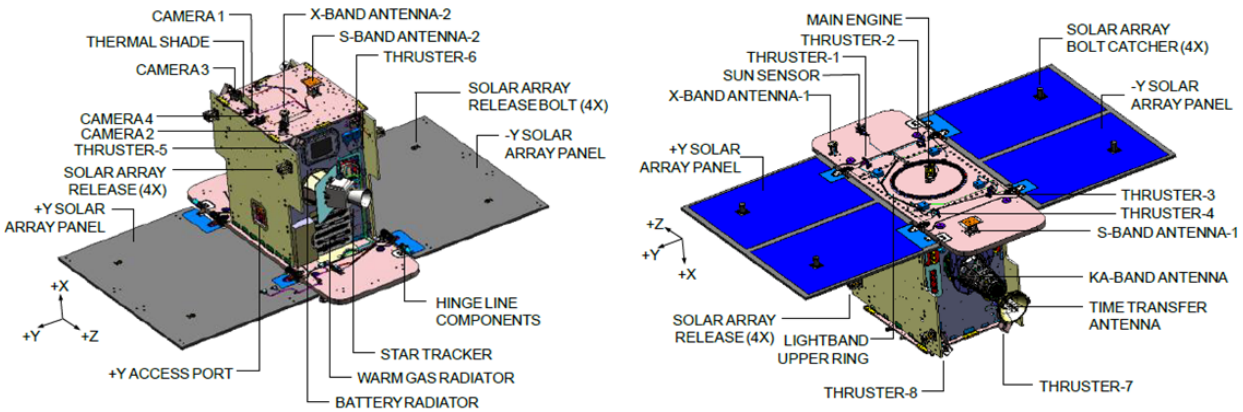

Figure 2.2: GRAIL spacecraft (top view and bottom view) from Spath (2012, p. 8)

The payload on each spacecraft consists of

- the Lunar Gravity Ranging System (LGRS) and
- the Education and Public Outreach (E/PO) MoonKAM (Moon Knowledge Aquired by Middle school students) System.

Lunar Gravity Ranging System

The science payload is the LGRS, which is derived from the GRACE mission. The instrument consists of the following elements:

Ka-band (32 GHz) transmitter-receiver: dual-one-way ranging measurement to measure the relative range differences between the two spacecraft.

S-Band (2 GHz) Time Transfer System (TTS): provides a two-way time-transfer link between the spacecraft to synchronize and measure the clock offset between the two LGRS clocks.

X-Band (8 GHz) Radio Science Beacon (RSB): provides a one-way signal to the ground to determine the orbit via Doppler Tracking.

Ultra-Stable Oscillator (USO): provides a steady reference frequency, that is used by all of the other instrument elements.

Education and Public Outreach Instrument - MoonKAM

The MoonKAM system consists of a digital video controller and a set of cameras to take images or videos of the lunar surface. Middle school children are involved in the image collection by operating the cameras (Hoffman et al., 2010; NASA Press Kit, 2011).

2.2.2 Mission phases

The GRAIL mission is subdivided into the following seven mission phases (cf. Figure 2.3):

Launch: initial spacecraft launch from the CCAF Station on 10^{th} September 2011

Trans-Lunar Cruise (TLC): 4 month low energy trajectory via the Sun-Earth Lagrange point to the Moon. On 31^{st} December 2011 GRAIL-A and on 1^{st} January 2012 GRAIL-B approach the Moon under its south pole.

Lunar Orbit Insertion (LOI): both spacecraft are placed into near-polar, elliptical orbits with an orbital period of 11.5 hours.

Orbit Period Reduction (OPR): a series of maneuvers is performed to reduce to near-polar, near-circular orbits with a mean altitude of 55 kilometers and an orbital period of just under two hours.

Transition to Science Formation (TSF): a series of maneuvers is performed to achieve the initial separation distance and to ensure that the satellites fly in formation, i.e. that GRAIL-B is ahead of GRAIL-A.

Science Phase: is subdivided into Primary Mission (PM) and Extended Mission (EM). This phase consists of the collection of gravity science data and imaging the lunar surface by the MoonKAM system.

Primary Mission: during the 82-day Science Phase three 27.3-day mapping cycles (lunar sidereal period) are completed, therefore the Moon rotates three times underneath the GRAIL orbit. The PM started on 1st March 2012 and lasted until 29th May 2012. During the PM the mean orbit altitude is 55 km ($\pm$ 35 km) and the separation distance varies between 82-218 km.

Extended Mission: the PM was planned to end on 4th June 2012, at the time of a partial lunar eclipse. The EM started on 30th August 2012, therefore GRAIL collected another three months of data at an even lower orbit altitude.

Decommissioning Phase: impact of the spacecraft on the lunar surface on 17th December 2012.

Further details on the GRAIL mission phases can be found in Hoffman et al. (2010) and NASA Press Kit (2011).

Table 2.1: Overview of GRAIL mission phases

Mission phases	
Launch	10-Sept-2011
Lunar Orbit Insertion	31-Dec-2011 (Ebb)
	01-Jan-2012 (Flow)
Science Mission	March-May 2012
Extended Mission Start	30-Aug-2012
Decommissioning	17-Dec-2012

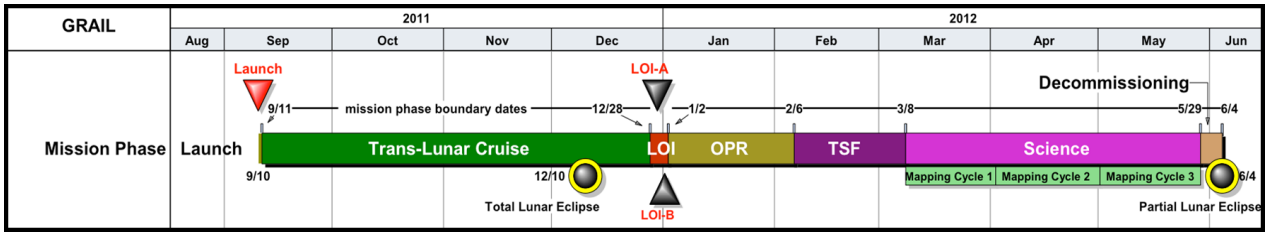

Figure 2.3: Initial GRAIL mission design time line from Havens and Beerer (2012, p. 2)

2.3 Data levels

All available data products related to GRAIL are archived and distributed by the Geosciences Node of NASA's Planetary Data System (PDS).

The GRAIL Science Data System (SDS) uses NASA processing levels, which are defined in Table 2.2. For the gravity field recovery calibrated data products (processing level 1B) are used. The LGRS CDR (Calibrated Data Record) data set contains calibrated and resampled data from the Lunar Gravity and Ranging System.

Table 2.2: Processing levels from Kahan (2012, p. 8)

NASA level	Description
Level 0	Corrected for telemetry errors and split or decommutated according to instrument. Sometimes called Experimental Data Record (EDR). Data are also tagged with time and location of acquisition.
Level 1a	Edited data that are still in units produced by instrument, but that have been corrected so that values are expressed in or are proportional to some physical unit such as radiance. No resampling, so original values can be recovered.
Level 1b	Data that have been resampled in the time or space domains in such a way that the original edited data cannot be reconstructed. Could be calibrated in addition to being resampled.
Level 2	Derived results, as maps, reports, graphics, etc.

Chapter 3

Synthesis - Orbit integration

In the case of simulation studies, orbit information and ll-SST measurements (ranges, range rates, range accelerations) have to be simulated at first. From the simulated observations the spherical harmonic coefficients, which represent the lunar gravity field, can be estimated in a second step (cf. Chapter 5). The first step is denoted as *synthesis* and includes the orbit integration from an a-priori reference field.

The relation between the satellite motion and all perturbing forces acting on the satellites has to be established. Therefore, a physical model, describing the orbital motion, is introduced. Since the equation of motion depends on the forces acting on the satellite, this forces have to be modeled in an accurate way.
The purpose of this chapter is to describe the modeling of the gravitational perturbing forces. In particular, the accelerations due to the gravity field of the Moon and the accelerations due to other celestial bodies, especially Earth and Sun, are described in more detail. Due to the reason that for Moon-orbiting satellites non-gravitational forces have much less influence than gravitational forces, they are not taken into account.

The equations of motion are only valid in a space-fixed, inertial reference system. Whereas, the gravitational potential is defined with respect to a body-fixed system. A body-fixed system is also required for the description of results derived from satellite geodesy (e.g. selenoid [1] heights) (Seeber, 1989).
Therefore, the necessity of transformations between both systems arises. All required transformations are described in this chapter as well.

Observation simulation and parameter estimation is accomplished using the GROOPS (Gravity Recovery Object Oriented Programming System) software package. An overview of the workflow of the synthesis is given in Figure 3.1.

The simulation of ll-SST observations is described in Chapter 4.

[1] undulations referred to the Moon. The word "seleno" denotes the Moon and is derived from the Greek Deity Selene.

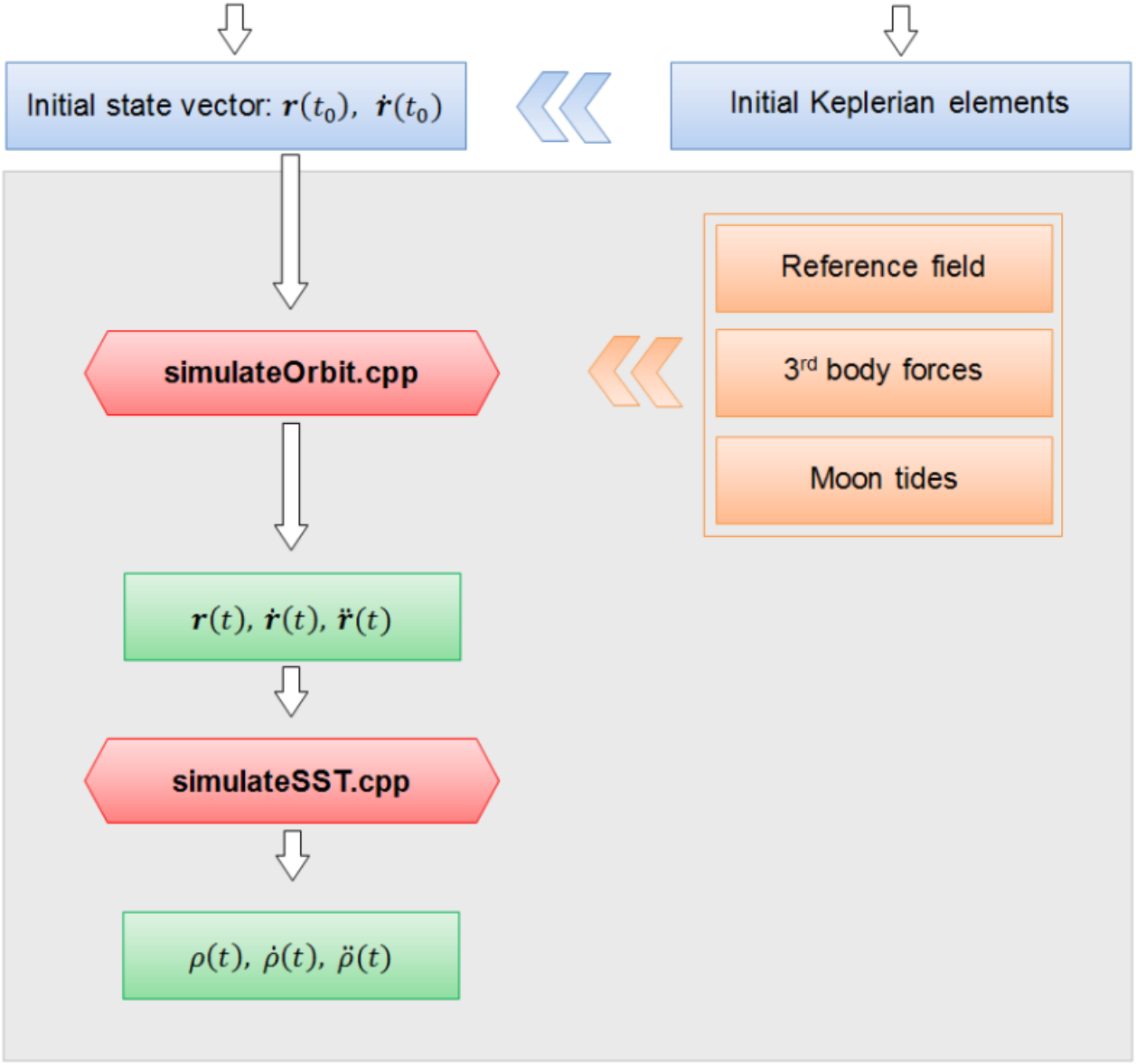

Figure 3.1: Workflow - Synthesis

3.1 Physical model

According to Newton's second law of motion

> *The rate of change of momentum of a body is proportional to the force impressed and is in the direction in which the force acts,*

the connection between the orbital motion of a satellite and all forces acting on it can be established. The second law of motion is valid in an inertial system:

$$\frac{\partial \mathbf{p}(t)}{\partial t} = \dot{\mathbf{p}}(t) = \mathbf{F}(t, \mathbf{r}, \dot{\mathbf{r}}). \tag{3.1}$$

The linear momentum is given by

$$\mathbf{p}(t) = m(t)\dot{\mathbf{r}}(t). \tag{3.2}$$

Substituting (3.2) in (3.1) and differentiating (3.2) with respect to time yields

$$m\ddot{\mathbf{r}}(t) + \dot{m}\dot{\mathbf{r}}(t) = \mathbf{F}(t, \mathbf{r}, \dot{\mathbf{r}}). \tag{3.3}$$

In general the mass of the satellite can be subject to changes, but the mass changes due to fuel consumption are negligibly small. Therefore, a constant mass $\dot{m} = 0$ is assumed. From this Newton's equation of motion becomes

$$m\ddot{\mathbf{r}}(t) = \mathbf{F}(t, \mathbf{r}, \dot{\mathbf{r}}). \tag{3.4}$$

Introducing the specific force $\mathbf{f} := \frac{1}{m}\mathbf{F}$, defined as the force per unit mass, gives

$$\ddot{\mathbf{r}}(t) = \mathbf{f}(t, \mathbf{r}, \dot{\mathbf{r}}). \tag{3.5}$$

The satellite experiences mainly accelerations due to the gravity field of the Moon, which are denoted as $\mathbf{g}$. Additionally, the satellite experiences accelerations because of perturbing forces, which are in particular:

- $\mathbf{a}_\mathrm{t}$: Accelerations due to other celestial bodies (Earth, Sun and planets)
- $\mathbf{a}_\mathrm{s}$: Accelerations due to the solid Moon tides
- $\mathbf{a}_\mathrm{sp}$: Accelerations due to solar radiation pressure
- $\mathbf{a}_\mathrm{a}$: Accelerations due to the albedo
- further non-gravitational forces (cf. Park et al., 2012)

The perturbing forces $\mathbf{a}_\mathrm{t}$ and $\mathbf{a}_\mathrm{s}$ are gravitational in nature, whereas the remaining forces are non-gravitational perturbations. Only the gravitational perturbations are modeled. Hence, the equation of motion can be re-formulated to

$$\ddot{\mathbf{r}}(t) = \mathbf{f}(t, \mathbf{r}, \dot{\mathbf{r}}) = \mathbf{g} + \mathbf{a} = \mathbf{g} + \mathbf{a}_\mathrm{t} + \mathbf{a}_\mathrm{s}. \tag{3.6}$$

3.2 Gravity field

The gravity field is a conservative vector field, i.e. it is a vector field which is the gradient of a scalar function $\mathbf{g} = \nabla V$, known as the gravitational potential V. Conservative vector fields have the property that the line integral from one point to another is path independent. Additionally, conservative vector fields are irrotational, meaning that they have vanishing curl and are source-free in the exterior. According to equation (3.7) the gravitational potential V in the exterior of a celestial body satisfies Laplace's equation

$$\langle \nabla, \nabla V \rangle = \Delta V = \frac{\partial^2 V}{\partial x^2} + \frac{\partial^2 V}{\partial y^2} + \frac{\partial^2 V}{\partial z^2} = 0, \tag{3.7}$$

where the Cartesian coordinates are body-fixed and rotating along with the celestial body in inertial space.

Functions satisfying Laplace's equation are called harmonic functions. Hence, the gravitational potential of the Moon, or selenopotential, is a harmonic function outside the celestial body and can be expressed in spherical harmonics (Heiskanen and Moritz, 1967)

$$V(r, \theta, \lambda) = \frac{GM}{R} \sum_{n=0}^{\infty} \left(\frac{R}{r}\right)^{n+1} \sum_{m=0}^{n} (\bar{c}_{nm} C_{nm}(\theta, \lambda) + \bar{s}_{nm} S_{nm}(\theta, \lambda)), \tag{3.8}$$

where r, θ, λ are the selenocentric spherical coordinates radius, co-latitude and longitude. The constants R and GM are the mean equatorial lunar radius and the gravitational parameter of the Moon, consisting of the gravitational constant G times the Moon's mass M. The normalized spherical harmonic coefficients of the expansion of degree n and order m are represented by $\bar{c}_{nm}$ and $\bar{s}_{nm}$. The normalized base functions C_{nm} and S_{nm} are given by

$$\begin{aligned} C_{nm}(\theta, \lambda) &= \cos(m\lambda) \bar{P}_{nm}(\cos\theta), \\ S_{nm}(\theta, \lambda) &= \sin(m\lambda) \bar{P}_{nm}(\cos\theta), \end{aligned} \tag{3.9}$$

with the fully normalized associated Legendre functions of the first kind $\bar{P}_{nm}(\cos\theta)$. The Legendre functions and the base functions are orthonormal, this is achieved by normalizing the orthogonal Legendre functions P_{nm}. The normalization is done according to Kaula (2000):

$$\bar{P}_{nm} = \sqrt{\frac{(2 - \delta_{0m})(2n + 1)(n - m)!}{(n + m)!}}\, P_{nm}. \tag{3.10}$$

The Legendre functions are derived from the so-called Legendre polynomials, which may be obtained by recursion formulae (Heiskanen and Moritz, 1967).

The relation between the selenopotential and the satellite motion is given by the acceleration due to the gravitational attraction. The acceleration $\mathbf{g}$ due to the selenopotential is given by the gradient of V:

$$\mathbf{g}(\lambda, \theta, r) = \nabla V(\lambda, \theta, r). \tag{3.11}$$

Usually, the field strength $\mathbf{g}$ is calculated by the partial derivatives of the base functions with respect to the spherical coordinates. But it can also be expressed in Cartesian body-fixed coordinates as a linear combination of the base functions (Ilk, 1983a), which then reads

$$\begin{aligned}\mathbf{g}(\lambda,\theta,r) &= \nabla V(\lambda,\theta,r) = \begin{pmatrix}\partial V/\partial x\\ \partial V/\partial y\\ \partial V/\partial z\end{pmatrix}\\ &= \frac{GM}{2R^2}\sum_{n=0}^{\infty}\left(\frac{R}{r}\right)^{n+2}\sqrt{\frac{2n+1}{2n+3}}\sum_{m=0}^{n}\left\{c_{nm}\begin{pmatrix}C^-_{nm}-C^+_{nm}\\ -S^-_{nm}-S^+_{nm}\\ -2C^0_{nm}\end{pmatrix}+s_{nm}\begin{pmatrix}S^-_{nm}-S^+_{nm}\\ C^-_{nm}+C^+_{nm}\\ -2S^0_{nm}\end{pmatrix}\right\}\end{aligned} \tag{3.12}$$

with

$$\begin{aligned}&C^-_{nm} = f^-_{nm}C_{n+1,m-1},\ C^0_{nm} = f^0_{nm}C_{n+1,m},\ C^+_{nm} = f^+_{nm}C_{n+1,m+1},\\ &S^-_{nm} = f^-_{nm}S_{n+1,m-1},\ S^0_{nm} = f^0_{nm}S_{n+1,m},\ S^+_{nm} = f^+_{nm}S_{n+1,m+1},\end{aligned} \tag{3.13}$$

and the factors

$$\begin{aligned}&f^-_{nm} = [(n-m+1)(n-m+2)(1+\delta_{1m})]^{1/2},\\ &f^0_{nm} = [(n-m+1)(n+m+1)]^{1/2},\\ &f^+_{nm} = [(n+m+1)(n+m+2)(1+\delta_{0m})]^{1/2},\\ &\text{with } C_{nm}=0 \text{ for } m<0 \text{ and } S_{nm}=0 \text{ for } m<1.\end{aligned} \tag{3.14}$$

The acceleration due to the selenopotential is given in a body-fixed system (cf. Section 3.5.2), therefore a transformation from the body-fixed system to the inertial system (cf. Section 3.5.1) is necessary:

$$\mathbf{x}_{\mathrm{BF}} = \mathbf{R}\ \mathbf{x}_{\mathrm{I}}. \tag{3.15}$$

The rotation matrix $\mathbf{R}$ relates the body-fixed coordinates subscripted by BF to the inertial coordinates subscripted by I. Hence, the acceleration in the inertial frame, which is used for force computation (cf. equation (3.6)) and orbit integration, is given by

$$\mathbf{g}_{\mathrm{I}} = \mathbf{R}^T\ \mathbf{g}_{\mathrm{BF}}. \tag{3.16}$$

Details on the used reference systems and transformation can be found in Section 3.5.

3.2.1 Functionals of the gravitational potential

In practice the series expansion of the gravitational potential V in equation (3.8) has to be limited to an upper maximum degree $n_{\max}$. The connection between the maximum resolved degree $n_{\max}$ and the spatial resolution D is

$$D = \frac{\pi R}{n_{\max}}, \tag{3.17}$$

where R is the mean equatorial lunar radius. The LP gravity field model JGL165P1 is complete up to degree and order 165, which corresponds to a spatial resolution of about 33 km.

Furthermore, the coefficients corresponding to degree $n = 0, 1$ are not assumed to be unknown. The central term ($n = 0$) of the series expansion in equation (3.8) is $\frac{GM}{R}$ and describes the gravitational potential of a homogeneous sphere. Usually, the origin of the body-fixed coordinate frame is chosen to coincide with the centre of mass. Consequently, the terms of degree $n = 1$ become zero.
The gravitational potential can be separated into the geometrically modeled normal potential U and the disturbing potential T, which represents the variations of the true gravity field due to the inhomogeneous mass distribution in the interior of the Moon:

$$V = U + T. \tag{3.18}$$

According to Bruns' formula, the selenoid heights N, representing the separation between the selenoid and the reference surface (geometrical analogue to the disturbing potential), are obtained by multiplying the disturbing potential by the reciprocal value of the normal gravity (Heiskanen and Moritz, 1967):

$$N \approx \frac{T}{\gamma}. \tag{3.19}$$

The normal gravity is expressed by its spherical approximation

$$\gamma \approx \frac{GM}{R^2}. \tag{3.20}$$

By differentiating the disturbing potential T (3.18) with respect to r once, one gets the gravity anomalies and gravity disturbances

$$\begin{aligned} \Delta g &= -\frac{\partial T}{\partial r} - \frac{2}{r}T, \\ \delta g &= -\frac{\partial T}{\partial r}. \end{aligned} \tag{3.21}$$

The second derivative with respect to r gives the radial gravitational gradient

$$V_{rr} = \frac{\partial^2 T}{\partial r^2}. \tag{3.22}$$

The radial derivations in equations (3.21) and (3.22), as well as a field continuation up to an arbitrary height $r = R+h$ can be described by introducing a factor depending on the degree n of the spherical harmonic expansion. These factors are represented in the spectral Meissl-scheme in Figure (3.2). The figure shows the disturbing potential along with its radial first and second derivatives at satellite altitude and at surface-height. The arrows indicate attenuation and amplification, which corresponds to differentiation.

The upward continuation to an arbitrary height causes an attenuation (low-pass filter), whereas the derivations can be interpreted as an amplification (high-pass filter) of the signal.
The decay of gravity fields depends on the distance from the source and the wavelength, i.e. short-wavelength anomalies are attenuated stronger than long-wavelength anomalies.

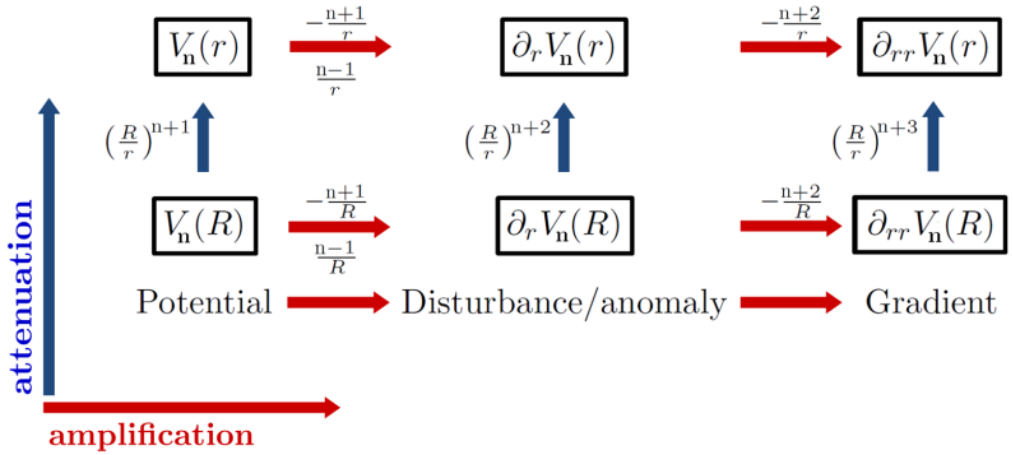

Figure 3.2: Meissl-scheme

3.2.2 Degree variances

In order to compare different gravity field solutions the variances of different functionals of the disturbing potential (cf. Section 3.2.1) are determined.
According to the orthogonality relations of the spherical harmonics the Power Spectral Density (PSD), which represents the energy content per degree of a gravity field (solution), can be expressed by the degree variances

$$\sigma_n^2 = \sum_{m=0}^{n} (c_{nm}^2 + s_{nm}^2). \tag{3.23}$$

To compare the gravity field solution with a reference field $(c_{nm}^{\text{ref}}, s_{nm}^{\text{ref}})$ the so-called error degree variances are used:

$$\Delta\sigma_n^2 = \sum_{m=0}^{n} ((c_{nm} - c_{nm}^{\text{ref}})^2 + (s_{nm} - s_{nm}^{\text{ref}})^2). \tag{3.24}$$

The error degree variances can be seen as a measure for the consistency of two solutions in the spectral domain.

The mean value of the signal per degree can be expressed by the RMS (Root Mean Square) of the degree-wise error variances

$$\text{DE-RMS}_n = \sqrt{\frac{1}{2n+1}\Delta\sigma_n^2}. \tag{3.25}$$

The functional relation between gravity field parameters (cf. Section 3.2.1) enables also the calculation of the RMS of the degree-wise error variances in selenoid heights:

$$\text{DE-RMS}_n(N) = R\sqrt{\frac{1}{2n+1}\Delta\sigma_n^2}. \tag{3.26}$$

According to the Kaula-rule of thumb (Kaula, 2000), the degree variances of the Moon can be approximated by

$$\sigma_n^2 \approx \sqrt{(2n+1)}\ \frac{2.5 \cdot 10^{-4}}{n^2}, \tag{3.27}$$

with the normalized coefficients having a zero mean value and the standard deviation corresponds to the square of n.

The formal errors follow equation (3.23), but instead of the coefficients c_{nm}, s_{nm} the variances of the coefficients $\hat{\sigma}(c_{nm}), \hat{\sigma}(s_{nm})$ are used:

$$\hat{\sigma}_n^2 = \sum_{m=0}^{n} (\hat{\sigma}^2(c_{nm}) + \hat{\sigma}^2(s_{nm})). \tag{3.28}$$

3.3 3rd body forces

In addition to the gravity field of the Moon, other time varying effects, such as the tidal accelerations of celestial bodies (Earth, Sun and planets) and the solid Moon tides, should be taken into account. In particular, the Earth because of its proximity to the Moon and the Sun due to its large mass are causing perturbing accelerations to the spacecraft. Because of the great distance the Earth, the Sun and other planets can be regarded as point masses.

According to Newton's law of gravitation

$$\ddot{\mathbf{r}} = \nabla \frac{GM}{r} = -GM \frac{\mathbf{r}}{||\mathbf{r}||^3}, \tag{3.29}$$

the acceleration of a spacecraft by the point mass of the Earth $M_\oplus$ is given by

$$\ddot{\mathbf{r}} = -GM_\oplus \cdot \frac{\mathbf{r} - \mathbf{r}_\oplus}{||\mathbf{r} - \mathbf{r}_\oplus||^3} = GM_\oplus \cdot \frac{\mathbf{r}_\oplus - \mathbf{r}}{||\mathbf{r}_\oplus - \mathbf{r}||^3}, \tag{3.30}$$

where $\mathbf{r}_\oplus$ is the position of the Earth and $\mathbf{r}$ is the position of the satellite with respect to the inertial frame. The coordinates of the celestial bodies can be obtained from the ephemeris JPL DE 421.
The value of $\ddot{\mathbf{r}}$ in (3.30) refers to an inertial reference system with its origin at the center of the Moon. But the Moon is not at rest, therefore the coordinate system is considered to be moving in space with the Moon but not rotating with it (revolution without rotation). Therefore, it is itself subject to an acceleration due to $M_\oplus$:

$$\ddot{\mathbf{r}} = GM_\oplus \cdot \frac{\mathbf{r}_\oplus}{||\mathbf{r}_\oplus||^3}. \tag{3.31}$$

To obtain the tidal acceleration of the satellite's Moon-centered position vector both values have to be subtracted. The tidal acceleration due to the Earth ($\oplus$) and the Sun ($\odot$) can be written as

$$\begin{aligned} \ddot{\mathbf{r}} &= GM_\oplus \cdot \left(\frac{\mathbf{r}_\oplus - \mathbf{r}}{||\mathbf{r}_\oplus - \mathbf{r}||^3} - \frac{\mathbf{r}_\oplus}{||\mathbf{r}_\oplus||^3} \right), \\ \ddot{\mathbf{r}} &= GM_\odot \cdot \left(\frac{\mathbf{r}_\odot - \mathbf{r}}{||\mathbf{r}_\odot - \mathbf{r}||^3} - \frac{\mathbf{r}_\odot}{||\mathbf{r}_\odot||^3} \right). \end{aligned} \tag{3.32}$$

In equation (3.32) the first part always depends on the position of the satellite, whereas the second part is constant and refers to the Moon's center (as shown in Figure 3.3).
The computation of the tidal accelerations are carried out separately for the individual two-body systems (Moon-Earth, Moon-Sun, etc.), and the results are subsequently added:

$$\mathbf{a}_\mathrm{t} = \mathbf{a}_\oplus + \mathbf{a}_\odot + \mathbf{a}_\mathrm{planets}. \tag{3.33}$$

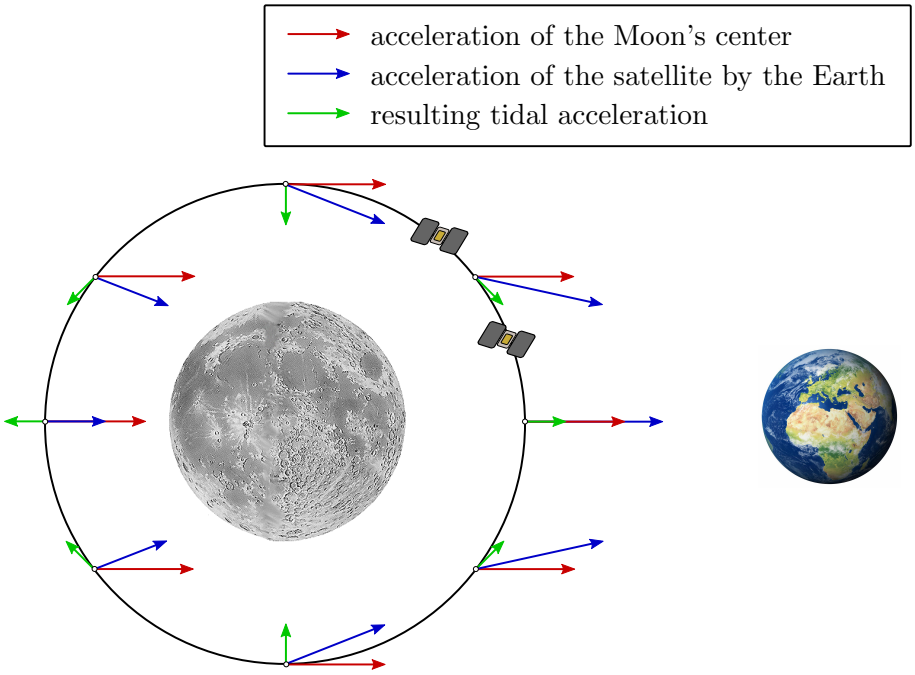

Figure 3.3: Tidal acceleration due to the Earth's gravitational pull

3.4 Lunar tides

Tidal accelerations influence not only the spacecraft, but also cause deformations and mass variations of the solid Moon, i.e. the Moon responds to the gravitational attraction of the Earth, the Sun and other planets. The lunar tides are the motions induced in the solid Moon and the changes in its gravitational potential caused by the tidal forces from celestial bodies. The changes in the gravitational potential have therefore also an indirect effect on satellite orbits.

The time-dependent changes of the gravitational potential due to the solid Moon tides can be modeled as variations in the normalized potential coefficients $\bar{c}_{nm}$ and $\bar{s}_{nm}$. The contributions to the normalized potential coefficients $\Delta\bar{c}_{nm}$ and $\Delta\bar{s}_{nm}$ are expressed in terms of the Love numbers k_{nm}.
The Moon is assumed to be elastic, because of that there is no phase lag in the deformational response of the Moon to the tidal forces. In the case of anelasticity, the deformational response is delayed and it causes the Love numbers to acquire small imaginary parts. The lunar tides are modeled according to the IERS Conventions 2010 (Petit and Luzum, 2010, p. 82).

Usually, the contributions to the potential coefficients are calculated in 3 steps (for details on the calculation refer to Petit and Luzum (2010)). Due to the assumed elasticity of the Moon, the changes in $\bar{c}_{nm}$ and $\bar{s}_{nm}$ are computed using the frequency-independent nominal values of k_{nm}. The Tide Generating Potential (TGP) can be expanded in spherical harmonics and therefore the time-varying corrections $\Delta\bar{c}_{nm}$ and $\Delta\bar{s}_{nm}$ can be modeled by

$$\Delta\bar{c}_{nm} - i\Delta\bar{s}_{nm} = \frac{k_{nm}}{2n+1} \sum_{j=\oplus,\mathfrak{O}} \frac{GM_j}{GM_{\mathfrak{Y}}} \left(\frac{R_{\mathfrak{Y}}}{r_j}\right)^{n+1} \bar{P}_{nm}(\sin\Phi_j) e^{im\lambda_j}. \tag{3.34}$$

k_{nm} ... frequency-independent Love number for degree n and order m

j ... tidal disturbing bodies (Earth and Sun)

$R_{\mathfrak{D}}$ ... equatorial Radius of the Moon

$GM_{\mathfrak{D}}$ ... gravitational parameter of the Moon

GM_j ... gravitational parameter of the Earth ($j = \oplus$) and of the Sun ($j = \mathfrak{O}$)

r_j ... distance from the Moon-center to the Earth or Sun

Φ_j ... body-fixed latitude of the Earth or Sun

λ_j ... body-fixed longitude of the Earth or Sun

If only degree two and three coefficients are considered, the contributions to the potential coefficients are given by:

$$\begin{aligned}
\Delta\bar{c}_{nm} &= \sum_{j=\oplus,\mathfrak{O}} \frac{GM_j}{GM_{\mathfrak{D}}} \sum_{n=2}^{3} \frac{1}{2n+1} \left(\frac{R_{\mathfrak{D}}}{r_j}\right)^{n+1} \sum_{m=0}^{n} \bar{P}_{nm}(\sin\Phi_j) \left(k_{nm}^{\mathrm{Re}} \cos(m\lambda_j) + k_{nm}^{\mathrm{Im}} \sin(m\lambda_j)\right), \\
\Delta\bar{s}_{nm} &= \sum_{j=\oplus,\mathfrak{O}} \frac{GM_j}{GM_{\mathfrak{D}}} \sum_{n=2}^{3} \frac{1}{2n+1} \left(\frac{R_{\mathfrak{D}}}{r_j}\right)^{n+1} \sum_{m=0}^{n} \bar{P}_{nm}(\sin\Phi_j) \left(k_{nm}^{\mathrm{Re}} \sin(m\lambda_j) + k_{nm}^{\mathrm{Im}} \cos(m\lambda_j)\right).
\end{aligned} \tag{3.35}$$

In equation (3.35) only the zonal real or elastic parts k_n^{Re} are considered. Therefore, the equations simplify to

$$\begin{aligned}
\Delta\bar{c}_{nm} &= \sum_{j=\oplus,\mathfrak{O}} \frac{GM_j}{GM_{\mathfrak{D}}} \sum_{n=2}^{3} \frac{1}{2n+1} \left(\frac{R_{\mathfrak{D}}}{r_j}\right)^{n+1} \bar{P}_{nm}(\sin\Phi_j) \left(k_n^{Re} \cos(m\lambda_j)\right), \\
\Delta\bar{s}_{nm} &= \sum_{j=\oplus,\mathfrak{O}} \frac{GM_j}{GM_{\mathfrak{D}}} \sum_{n=2}^{3} \frac{1}{2n+1} \left(\frac{R_{\mathfrak{D}}}{r_j}\right)^{n+1} \bar{P}_{nm}(\sin\Phi_j) \left(k_n^{Re} \sin(m\lambda_j)\right).
\end{aligned} \tag{3.36}$$

3.5 Reference systems

As mentioned before, the equations of motion, which describe the satellite motion, are only valid in an inertial reference system. Whereas, the gravitational potential is defined with respect to a body-fixed system.
Therefore, it is necessary to transform a set of coordinates from an inertial reference frame to a rotating body-fixed frame and vice versa. To accomplish these coordinate transformations well defined and reproducible inertial and body-fixed reference frames are required and a mutual relation between both frames has to be established.

In this section an overview of all used inertial and body-fixed reference systems and their practical realizations, denoted as reference frames, is given. Additionally, the required transformations are described in detail.

3.5.1 Inertial reference systems

An *inertial reference system* is a nonaccelerated system at rest or in a state of uniform translational motion free of rotation, i.e. it moves with constant velocity. In such an inertial reference system Newton's laws of motion apply and it is needed to model the ephemeris of celestial bodies and artificial satellites in space.
A *quasi-inertial reference system* also moves without rotational motion, but its origin is accelerated due to the fact that the system is orbiting the Sun, for example.

A *space-fixed system* (Celestial Reference System – CRS) is a quasi-inertial reference system; it is distinguished between dynamical and kinematic CRS. A dynamical CRS is based on the ephemeris of bodies of the solar system (planets, moon, and satellites). A kinematic CRS is defined by the positions and motions of stars and very distant extragalactic radio sources (quasars). An example for a kinematic CRS is the International Celestial Reference System (ICRS). The coordinates of a CRS are usually defined by an equatorial system of spherical astronomy.

There are several types of quasi-inertial frames in use. Here, the systems and frames used with respect to the satellite mission GRAIL are described. Details can be found in Olds (2009).

Earth-Centered Earth Mean Equator and Equinox of Epoch J2000 – EME2000

The Epoch J2000 corresponds to the Julian Date (JD) 2451545.0 or Modified Julian Date (MJD) 51544.5 or 1.5 January, 2000 Barycentric Dynamic Time (TDB). The axes of the EME2000 (cf. Figure 3.4) are defined as follows:

X_{EME}... Parallel to the Vernal Equinox of the Earth Mean Heliocentric Orbit of Epoch J2000,

Z_{EME}... Mean Earth Equator normal of Epoch J2000,

Y_{EME}... completed to a right-handed system.

"Access to the EME2000 system is provided by the so called FK5 star catalogue, which provides precise positions and proper motions of some 1 500 stars for the J2000 epoch and in the given reference frame. More recently, based upon certain dynamical difficulties in the definition of the ecliptic plane and the equinox, it has been decided to replace EME2000 with a new International Celestial Reference System, or in short ICRS. The practical realisation of the ICRS is designated the International Celestial Reference Frame (ICRF)" (Floberghagen, 2002, pp. 241).

EME2000 Lunar-Centered Solar System Barycentric Frame

This frame is used with respect to the Moon. It is the EME2000 inertial reference frame, re-centered at the Moon using the DE421 planetary ephemeris.

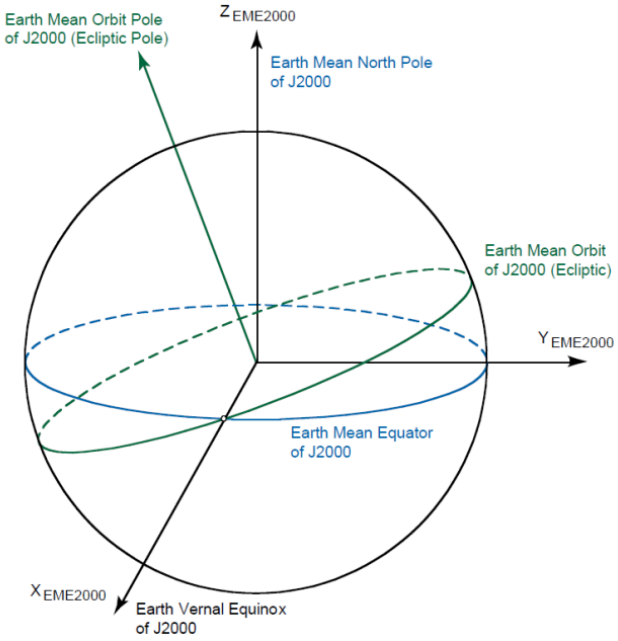

Figure 3.4: EME2000 from Roncoli (2005, p. 40)

3.5.2 Moonfixed reference systems

In contrast to an inertial reference system, a body-fixed system is rotating with its body, i.e. planetocentric coordinates are expressed as right-handed coordinates with the origin at the body's center of mass. For the Moon two slightly different body-fixed reference systems exist.

Mean Earth/polar axis system (ME)

The body-fixed ME system, sometimes called mean Earth/polar axis system, defines the z-axis along the Moon's mean axis of rotation. The x-axis is defined towards the the prime meridian (0° longitude), which is the mean direction to the Earth.
At the Moon's "mean sub-Earth point" the lunar equator intersects the prime meridian. A mean sub-Earth point is used to define the prime meridian, because it varies slightly due to orbital eccentricity, inclination and other factors (LRO Project, 2008).

Principal axis system (PA)

The body-fixed PA system, sometimes called axis of figure system, is aligned with the principal axes of inertia of the Moon.

The rotation axes of the PA and ME system do not coincide, because the Moon is not a synchronously rotating ellipsoid. Therefore, the axes of the two body-fixed systems differ and cause differences in the coordinates of a point on the lunar surface (Roncoli, 2005).
"The difference in the coordinates of a point on the surface of the Moon between these two systems is approximately 860 m" (Archinal et al., 2011, p. 114). Both systems are in use, but the ME system is recommended, because most cartographic products use the ME system. But the PA system is typically used with respect to gravity field purposes. The PA system is used for the GRAIL simulations and real data analysis.

3.5.3 Transformations - Elementary rotations

A rotation-based transformation between two Cartesian frames with identical origins is given by

$$\begin{bmatrix} x_{\mathrm{p'}} \\ y_{\mathrm{p'}} \\ z_{\mathrm{p'}} \end{bmatrix} = \mathbf{R} \begin{bmatrix} x_{\mathrm{p}} \\ y_{\mathrm{p}} \\ z_{\mathrm{p}} \end{bmatrix}. \tag{3.37}$$

The rotation matrix $\mathbf{R}$ realizes the coordinate transformation and rotates the vector $\mathbf{x}_{\mathrm{p}}$ into $\mathbf{x}_{\mathrm{p'}}$. Since the rotation matrix is orthogonal the inverse rotation is achieved by using the transposed matrix $\mathbf{R}^T$. The orthogonality implies the following fundamental properties

$$\mathbf{R}^T = \mathbf{R}^{-1} \quad , \quad \mathbf{R}\mathbf{R}^T = \mathbf{R}^T\mathbf{R} = \mathbf{I} \quad , \quad ||\det(\mathbf{R})|| = 1. \tag{3.38}$$

The rotation of a Cartesian coordinate frame can be performed by three sequential rotations about the x-, y-and z-axis by using elementary rotation matrices. The elementary rotation matrices, which describe for a right-handed frame a counter-clockwise rotation, are given by

$$\begin{aligned} \mathbf{R}_1(\alpha) &= \begin{bmatrix} 1 & 0 & 0 \\ 0 & \cos\alpha & \sin\alpha \\ 0 & -\sin\alpha & \cos\alpha \end{bmatrix}, \\ \mathbf{R}_2(\beta) &= \begin{bmatrix} \cos\beta & 0 & -\sin\beta \\ 0 & 1 & 0 \\ \sin\beta & 0 & \cos\beta \end{bmatrix}, \\ \mathbf{R}_3(\gamma) &= \begin{bmatrix} \cos\gamma & \sin\gamma & 0 \\ -\sin\gamma & \cos\gamma & 0 \\ 0 & 0 & 1 \end{bmatrix}. \end{aligned} \tag{3.39}$$

Any rotation in 3-dimensional space can be represented by three successive elementary rotations. In case of a so-called *Cartan rotation matrix* the composed rotation matrix consists of a specific sequence of rotations:

$$\mathbf{R} = \mathbf{R}_3(\alpha)\mathbf{R}_2(\beta)\mathbf{R}_1(\gamma) = \mathbf{R}_{\mathrm{c}}(\alpha, \beta, \gamma). \tag{3.40}$$

An alternative representation is the *Euler rotation matrix*:

$$\mathbf{R} = \mathbf{R}_3(\psi)\mathbf{R}_1(\theta)\mathbf{R}_3(\phi) = \mathbf{R}_{\mathrm{e}}(\phi, \theta, \psi). \tag{3.41}$$

Instead of describing a rotation between two frames by three rotation angles, quaternions can be used as well. The rotation matrix is expressed in terms of (normalized) parameters:

$$\begin{aligned} \mathbf{R} = \begin{bmatrix} q_1^2 - q_2^2 - q_3^2 + q_0^2 & 2(q_1q_2 + q_3q_0) & 2(q_1q_3 - q_2q_0) \\ 2(q_1q_2 - q_3q_0) & -q_1^2 + q_2^2 - q_3^2 + q_0^2 & 2(q_2q_3 + q_1q_0) \\ 2(q_1q_3 + q_2q_0) & 2(q_2q_3 - q_1q_0) & -q_1^2 - q_2^2 + q_3^2 + q_0^2 \end{bmatrix}, \\ \sqrt{q_0^2 + q_1^2 + q_2^2 + q_3^2} = 0. \end{aligned} \tag{3.42}$$

This representation is called *Hamilton parametrization*; compared to the Euler or Cartan representation it requires less arithmetic operations and is less susceptible to rounding errors.

3.5.4 Transformations - Cartesian coordinates ⇔ spherical coordinates

A point in space can either be expressed by Cartesian coordinates x, y, z or by its spherical coordinates, i.e. latitude φ , longitude λ and radius r.

The transformation of Cartesian coordinates to spherical coordinates can be done through

$$\begin{aligned} r &= \sqrt{x^2 + y^2 + z^2}, \\ \varphi &= \arctan\left(\frac{z}{\sqrt{x^2 + y^2}}\right), \\ \lambda &= \arctan(\frac{y}{z}). \end{aligned} \tag{3.43}$$

The inverse formulas are:

$$\begin{aligned} x &= r\ \cos\varphi\ \cos\lambda, \\ y &= r\ \cos\varphi\ \sin\lambda, \\ z &= r\ \sin\varphi. \end{aligned} \tag{3.44}$$

3.5.5 Transformations - Lunar libration

The lunar libration is described by means of three Euler libration angles ϕ, θ and ψ, which describe the rotation of the Moon between the ICRS and PA system (if derived from the JPL ephemeris). The libration angles describe the total libration, i.e. they account for both optical (geometrical) and physical librations.

Libration angles

The lunar libration angles describe the orientation of the PA system and are defined relative to the ICRS Earth equator and equinox. Components of any vector in the PA system can be rotated to the ICRS using the JPL libration angles. Using the inverse rotation any vector in the ICRS can be converted to the PA system (Taylor et al., 2010).

The three libration angles shown in Figure 3.5 are:

ϕ : the angle along the ICRS equator, counted from the ICRS X-axis to the ascending node of the lunar equator; nodal variations oscillating around 0°

θ : the inclination of the lunar equator to the ICRS equator; $23.44° \pm 1.54°$ with a period of 18.6 years

ψ : the angle along the lunar equator from the node to the lunar prime meridian (Archinal et al., 2011)

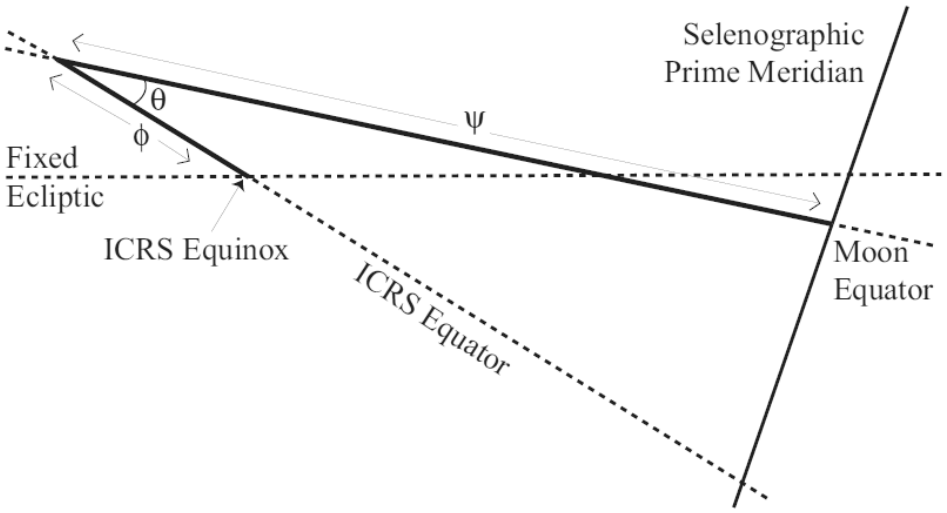

Figure 3.5: Euler libration angles ϕ, θ and ψ. The value of ϕ shown in this diagram is negative. Source: Taylor et al. (2010, p. 6)

The first rotation $\mathbf{R}_3(\phi)$ is performed to align the ICRS equinox with the ascending node. The second rotation $\mathbf{R}_1(\theta)$ aligns the ICRS equator with the lunar equator. Finally, the third rotation $\mathbf{R}_3(\psi)$ aligns the node with the prime meridian.
Hence, the composed rotation from the inertial system to the PA system becomes

$$\mathbf{x}_{\mathrm{PA}} = \mathbf{R}_3(\psi)\mathbf{R}_1(\theta)\mathbf{R}_3(\phi)\mathbf{x}_{\mathrm{ICRS}}. \tag{3.45}$$

The conversion between the two moon-fixed systems (ME and PA system), which is denoted as frame bias, can be done using the following expression (Williams et al., 2008, p. 10)

$$\mathbf{x}_{\mathrm{PA}} = \mathbf{R}_3(67''.92)\mathbf{R}_1(78''.56)\mathbf{R}_3(0''.30)\mathbf{x}_{\mathrm{ME}}. \tag{3.46}$$

The numerical values used for the rotations are specific to DE421 and cannot be used for past or future lunar ephemeris (Archinal et al., 2011).

JPL ephemeris

The Jet Propulsion Laboratory (JPL) provides a series of planetary and lunar ephemeris in the form of Chebyshev approximations. The Development Ephemeris (DE) are publicly available as ASCII file via FTP[2].

Currently, the DE421 ephemeris are considered the best available lunar ephemeris (Folkner et al., 2009b). The JPL ephemeris consist of past and future positions, velocities and accelerations of the Sun, Moon, and nine planets tabulated at equally spaced intervals of time, covering a specified span of years. In addition to planetary and lunar coordinates, the DE421 ephemeris file also contains numerical coefficients for Chebyshev polynomials representing the Euler lunar libration angles and the rates of the lunar libration angles in the PA system. An evaluation of the polynomials yields Cartesian coordinates in AU (Astronomical Unit) for planets and lunar libration angles in radians.

[2]ftp://ssd.jpl.nasa.gov/pub/eph/planets/

A comparison of the lunar libration angles ϕ, θ, ψ calculated from the JPL DE405 and DE421 ephemeris can be found in A.3.

Approximation

Apart from lunar libration angles there also exist closed formulas for the rotation from the ICRS to the ME system, but these formulas are approximated. Due to that reason they are only valid to a ∼150 m level of accuracy. Therefore, lunar ephemeris should be used to calculate the libration angles for the Moon (Archinal et al., 2011).

With the closed formulas the values for the direction of the north pole of rotation and the prime meridian can be calculated. The formulas can be found in Archinal et al. (2011, p.108). The direction of the north pole is specified by the value of its right ascension α_0 and declination δ_0. The location of the prime meridian is specified by W. For the calculation the standard epoch JD 2451545.0, i.e. 2000 January 1 12 hours TDB, is used:

$$\begin{aligned}
\alpha_0 &= 269^\circ.9949 + 0^\circ.0031T - 3^\circ.8787\ \sin E1 - 0^\circ.1204\ \sin E2 + 0.0700\ \sin E3 \\
&\quad - 0.0172\ \sin E4 + 0.0072\ \sin E6 - 0.0052\ \sin E10 + 0.0043\ \sin E13, \\
\delta_0 &= 66.5392 + 0.0130T + 1.5419\ \cos E1 + 0.0239\ \cos E2 - 0.0278\ \cos E3 + 0.0068\ \cos E4 \\
&\quad - 0.0029\ \cos E6 + 0.0009\ \cos E7 + 0.0008\ \cos E10 - 0.0009\ \cos E13, \\
W &= 38.3213 + 13.17635815d - 1.4 \times 10^{-12}d^2 + 3.5610\ \sin E1 + 0.1208\ \sin E2 \\
&\quad - 0.0642\ \sin E3 + 0.0158\ \sin E4 + 0.0252\ \sin E5 - 0.0066\ \sin E6 - 0.0047\ \sin E7 \\
&\quad - 0.0046\ \sin E8 + 0.0028\ \sin E9 + 0.0052\ \sin E10 + 0.0040\ \sin E11 + 0.0019\ \sin E12 \\
&\quad - 0.0044\ \sin E13,
\end{aligned} \tag{3.47}$$

$$\begin{aligned}
&E1 = 125^\circ.045 - 0^\circ.0529921d,\ E2 = 250^\circ.089 - 0^\circ.1059842d, \\
&E3 = 260^\circ.008 + 13^\circ.0120009d, E4 = 176.625 + 13.3407154d,\ E5 = 357.529 + 0.9856003d, \\
&E6 = 311.589 + 26.4057084d,\ E7 = 134.963 + 13.0649930d,\ E8 = 276.617 + 0.3287146d, \\
&E9 = 34.226 + 1.7484877d,\ E10 = 15.134 - 0.1589763d,\ E11 = 119.743 + 0.0036096d, \\
&E12 = 239.961 + 0.1643573d,\ E13 = 25.053 + 12.9590088d,
\end{aligned} \tag{3.48}$$

with

α_0, δ_0 ... ICRF equatorial coordinates at epoch J2000,

T ... interval in Julian centuries (of 36 525 days) from the standard epoch,

d ... interval in days from the standard epoch.

These lunar rotation angles in the ME system and in the standard α_0, δ_0, and W formulation can be converted with

$$\begin{aligned} \phi &= \alpha_0 + 90^\circ, \\ \theta &= 90^\circ - \delta_0, \\ \psi &= W, \end{aligned} \tag{3.49}$$

giving the Euler libration anlges.

3.6 Time systems

In this context, a uniform time scale is needed to model the motion of satellites. Additionally, a time system is necessary to describe the relative motion of the Moon with respect to inertial space and to date measurements and results.
To establish a time system a periodic process, a counter (to count the number of periods) and an origin where the counting starts are required, the time scale should be as uniform and stable as possible. In general there are three different groups of time systems in use

- **Sidereal Time or Universal Time:** a non-uniform time scale connected with the diurnal rotation of the Earth with respect to the inertial space
- **Ephemeris Time (ET), Dynamical Time (DT), Terrestrial Time (TT):** a conceptually uniform time scale based on the orbital motion of celestial bodies.
- **Atomic Time (TAI):** a practical realization of a uniform time scale, which is related to phenomena in nuclear physics and is based on atomic clocks.

The Dynamical Time (DT) replaced the ET. Within the Dynamical Time (DT) a distinction is made between:

- **TDB:** Barycentric Dynamical Time (orbital motions refer to the barycenter of the solar system)
- **TDT:** Terrestrial Dynamical Time (orbital motions reffer to the geocenter)

The forerunner of the DT was the ET, it was replaced by the TDT and the TDT was redefined as TT. TAI agrees with TT expect for a constant offset

$$\mathrm{TT} \equiv \mathrm{TDT} \equiv \mathrm{ET} \equiv \mathrm{TAI} + 32.184\,s. \tag{3.50}$$

TT and TDB mainly differ by periodic effects due to relativistic effects causing differences up to a few milliseconds. Within the provided GRAIL datasets TDB is used.

3.6.1 Julian Date and Modified Julian Date

For scientific applications continuous counting is preferred compared to a time scale counting with years, month and days with varying length (e.g. civilian calendar). Therefore, the Julian Date (JD), a continuous day count, has been introduced with a Julian Century of 36 525 days. The JD is the number of days since noon January 1, 4 713 BC. The counting started at noon

for historical reasons.

The adopted reference date J2000 is given by

$$\text{J2000} = \text{January 1.5, 2000} = \text{January 1, 2000 } 12^{\text{h}}, \tag{3.51}$$

which is equal to

$$\text{JD } 2\,451\,545.0. \tag{3.52}$$

The Modified Julian Date (MJD) has been introduced, because Julian day numbers have become quite large and counting is preferred to start at midnight. The MJD is defined as

$$\text{MJD} = \text{JD} - 2\,400\,000.5, \tag{3.53}$$

which corresponds to the number of days since midnight November 17, 1858. There exist several algorithms to transform the MJD to the Calendar date and vice versa (Montenbruck and Gill, 2001).

3.7 Orbit integration

For the computation of satellite orbits numerical methods for the solution of the equation of motion are used. Analytical methods cannot be used due to the presence of perturbing forces. A variety of methods has been developed for numerical integration, the method used in this context is described in Section 3.7.1. More details on numerical integration methods can be found in Montenbruck and Gill (2001).

The equation of motion (3.5) are second-order differential equations. If the perturbing forces are taken into account, the acceleration of a satellite is given by equation (3.6). The solution of the equation of motion corresponds to the 6-dimensional state vector $\mathbf{y}$ containing the position $\mathbf{r}(t)$ and the velocity $\dot{\mathbf{r}}(t)$ of the satellite

$$\mathbf{y}(t) = \begin{pmatrix} \mathbf{r}(t) \\ \dot{\mathbf{r}}(t) \end{pmatrix}, \tag{3.54}$$

which satisfies

$$\dot{\mathbf{y}}(t) = \frac{\partial \mathbf{y}(t)}{\partial t} = \mathbf{f}(t, \mathbf{y}(t)) = \begin{pmatrix} \dot{\mathbf{r}}(t) \\ \mathbf{a}(t, \mathbf{r}) \end{pmatrix}. \tag{3.55}$$

Here, the system of three second-order differential equations (3.54) is transformed to a system of six first-order differential equations (3.55).
The force function $\mathbf{a}(t, \mathbf{r})$ depends on the position $\mathbf{r}$. Since non-gravitational forces are neglected the force function is independent of the velocity of the satellite.

Starting with 6 initial values $[\mathbf{r}(t_0), \dot{\mathbf{r}}(t_0)]$ the positions and velocities of the orbit are determined with a constant sampling by numerical integration.

3.7.1 Numerical integration - Algorithm

The orbit is integrated from a given force function. The force function is given in terms of perturbing accelerations caused by the gravity field (cf. Section 3.2), 3$^{\text{rd}}$ bodies and tides (cf. Section 3.3 and 3.4):

$$\ddot{\mathbf{r}} = \mathbf{f}(t, \mathbf{r}) = \mathbf{g} + \mathbf{a}. \tag{3.56}$$

The orbit is calculated in the inertial frame, whereas the perturbing accelerations are given in a body-fixed frame. Therefore, a rotation is needed to transform the accelerations $\mathbf{g}$ and $\mathbf{a}$ from a body-fixed frame to an inertial frame and vice versa.
The integration starts with initial values (position and velocity) at a given time t_0. The orbit is then integrated for a given time span with an equal sampling Δt.
The algorithm uses a polynomial of a given degree M to integrate the force function and to extrapolate the new position and velocity of the satellite. In the following section the individual steps are described in detail.

First of all, the initial values are given as

- Keplerian elements $[a(t_0), e(t_0), i(t_0), \omega(t_0), \Omega(t_0), \nu(t_0)]$ or
- Initial state vector $[\mathbf{r}(t_0), \dot{\mathbf{r}}(t_0)]$

in an inertial frame. The formulas for the transformation between Keplerian elements and a state vector can be found in Appendix B.

The algorithm for the orbit integration and extrapolation consists of four steps:

1. In the first step initial estimates for the positions and velocities are determined using a Keplerian orbit. In total $M + 1$ initial estimates are necessary in order to enable a polynomial interpolation of degree M.

   - Transformation from initial state vector to Keplerian elements (cf. Appendix B)
   - Determination of position vectors $\mathbf{r}(\tau)$ and velocity vectors $\dot{\mathbf{r}}(\tau)$ with

     $$\begin{aligned} \tau &= t_k + \tau_j, \\ \tau_j &= (3 + j - M)\Delta t, \end{aligned} \tag{3.57}$$

     using a Keplerian orbit (cf. Appendix B).

   - Determination of acceleration vectors $\ddot{\mathbf{r}}(\tau)$ with

     $$\ddot{\mathbf{r}}(\tau) = \mathbf{R}^T \left[\mathbf{g}(\tau, \mathbf{R}\mathbf{r}(\tau)) + \mathbf{a}(\tau, \mathbf{R}\mathbf{r}(\tau))\right], \tag{3.58}$$

     where the rotation matrix $\mathbf{R}$ describes the rotation from the inertial to the body-fixed frame. The perturbing accelerations due to the gravity field $\mathbf{g}$ and the tides $\mathbf{a}$ are calculated according to equations (3.12), (3.32) and (3.35).

2. First refinement: According to equation (3.66) the positions are numerically integrated from the accelerations determined in step 1

$$\begin{aligned}\mathbf{r}(\tau) &= \mathbf{r}(t_k) + \dot{\mathbf{r}}(t_k) \cdot \tau_j, \\ \mathbf{r}(\tau) &= \mathbf{r}(\tau) + \sum_{n=0}^{M} \frac{1}{(n+1)(n+2)} \tau^{n+2} \sum_{j=0}^{M} w_{nj} \ddot{\mathbf{r}}(t_k + \tau_j).\end{aligned} \tag{3.59}$$

3. In the third step an improved value for the accelerations is calculated for the refined positions of step 2 according to equation (3.58).

4. Orbit integration: The final step contains the numerical integration and extrapolation to determine the orbit for the given time span (cf. Figure 3.6)

$$\begin{aligned}\mathbf{r}(\tau) &= \mathbf{r}(t_k) + \dot{\mathbf{r}}(t_k) \cdot \tau_j, \\ \dot{\mathbf{r}}(\tau) &= \dot{\mathbf{r}}(t_k), \\ \mathbf{r}(\tau) &= \mathbf{r}(\tau) + \sum_{n=0}^{M} \frac{1}{(n+1)(n+2)} \tau^{n+2} \sum_{j=0}^{M} w_{nj} \ddot{\mathbf{r}}(t_k + \tau_j), \\ \dot{\mathbf{r}}(\tau) &= \dot{\mathbf{r}}(\tau) + \sum_{n=0}^{M} \frac{1}{n+1} \tau^{n+1} \sum_{j=0}^{M} w_{nj} \ddot{\mathbf{r}}(t_k + \tau_j),\end{aligned} \tag{3.60}$$

with

$\tau_j = \Delta t,\ 2\Delta t$ and $3\Delta t$ for the positions,

$\tau_j = \Delta t$ for the velocities.

With equation (3.60) the position and velocity vector for $\tau = t_k + \Delta t$ are determined. With the extrapolated position and velcoity vector for $\tau = t_k + 3\Delta t$ the piecewise polynomial can be forwarded and evaluated for the next epoch (cf. Figure 3.6).
Steps 1-3 are needed to determine initial positions and velocities to enable the actual orbit integration and extrapolation in Step 4. The piecewise polynomial is forwarded gradually and Step 4 is repeated until the orbit is integrated over the whole time span.

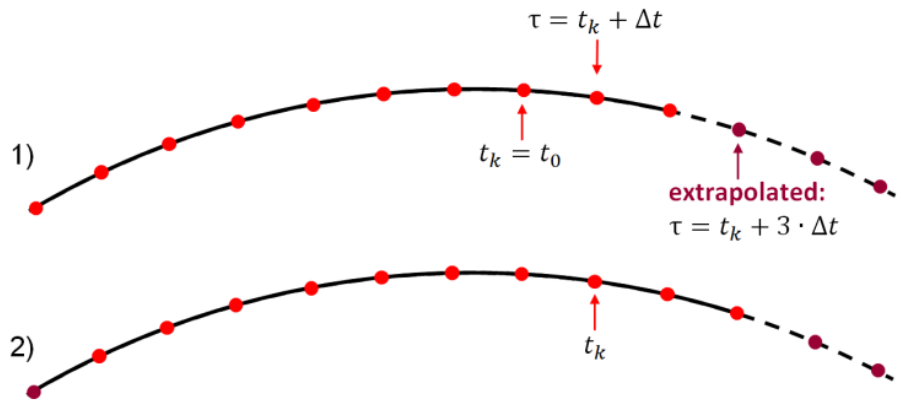

Figure 3.6: Orbit Integration - Polynomial interpolation

Numerical integration - Polynomial interpolation

The numerical integration of the accelerations $\ddot{\mathbf{r}}$ is done by integrating a piecewise adjusted polynomial (Mayer-Gürr, 2006). A polynomial of degree M is adjusted piecewise to the discrete and equally sampled accelerations, i.e. for each integrated position/time a new interpolation polynomial is adjusted:

$$\ddot{\mathbf{r}}(\tau) \approx \sum_{n=0}^{M} \mathbf{a}_n \tau^n. \tag{3.61}$$

The interpolation polynomial of degree M is unique with a given set of $M+1$ data points. The time variable τ is defined by the degree of the used polynomial and the sampling of the data points, where t_k represents the $M-3^{\text{th}}$ data point. Hence, the coefficients a_n of the polynomial for the data point t_k can be determined by solving a system of linear equations. The system of linear equations in matrix-vector form reads

$$\begin{pmatrix} \ddot{\mathbf{r}}(t_k+\tau_0) \\ \vdots \\ \ddot{\mathbf{r}}(t_k+\tau_M) \end{pmatrix} = \underbrace{\begin{pmatrix} 1 & \tau_0 & \tau_0^2 & \dots & \tau_0^M \\ \vdots & \vdots & \vdots & & \vdots \\ 1 & \tau_M & \tau_M^2 & \dots & \tau_M^M \end{pmatrix}}_{\mathbf{W}} \begin{pmatrix} \mathbf{a}_0 \\ \vdots \\ \mathbf{a}_M \end{pmatrix}, \tag{3.62}$$

with $\tau_j = (3+j-M)\cdot\Delta t$,

where Δt corresponds to the sampling. The time is chosen in a way that $\tau = 0$ corresponds to the $M-3^{\text{th}}$ data point $\ddot{\mathbf{r}}(t_k)$.

The polynomial coefficients are determined by solving the linear equation in (3.62):

$$\begin{pmatrix} \mathbf{a}_0 \\ \vdots \\ \mathbf{a}_M \end{pmatrix} = \mathbf{W}^{-1} \begin{pmatrix} \ddot{\mathbf{r}}(t_k+\tau_0) \\ \vdots \\ \ddot{\mathbf{r}}(t_k+\tau_M) \end{pmatrix}. \tag{3.63}$$

The coefficients of the inverse matrix $\mathbf{W}^{-1}$ are denoted as w_{nj}. Hence, the polynomial coefficients a_n can be expressed as a summation

$$\mathbf{a}_n = \sum_{j=0}^{M} w_{nj} \ddot{\mathbf{r}}(t_k+\tau_j). \tag{3.64}$$

Substituting equation (3.64) in equation (3.61) yields

$$\ddot{\mathbf{r}}(\tau) = \sum_{n=0}^{M} \tau^n \sum_{j=0}^{M} w_{nj} \ddot{\mathbf{r}}(t_k+\tau_j). \tag{3.65}$$

To obtain velocities from accelerations, the force function has to be integrated once. By integrating the force function twice one gets the positions:

$$\begin{aligned} \dot{\mathbf{r}}(\tau) &= \sum_{n=0}^{M} \frac{1}{n+1} \tau^{n+1} \sum_{j=0}^{M} w_{nj} \ddot{\mathbf{r}}(t_k+\tau_j), \\ \mathbf{r}(\tau) &= \sum_{n=0}^{M} \frac{1}{(n+1)(n+2)} \tau^{n+2} \sum_{j=0}^{M} w_{nj} \ddot{\mathbf{r}}(t_k+\tau_j). \end{aligned} \tag{3.66}$$

Chapter 4

Synthesis - SST

In order to enable simulation studies, ll-SST observations have to be simulated as well as orbit observations (cf. Chapter 3). These two steps are part of the *synthesis*.

The relation between the satellite orbits (positions, velocities and accelerations) and the Ka-band observations (ranges, range rates, range accelerations) has to be established. In particular, the simulated orbit data is used to derive ranges, range rates and range accelerations.
The purpose of this chapter is to describe the geometry of ll-SST observations in more detail.

4.0.2 Geometry of ll-SST

The position vectors of the two satellites A and B are represented by $\mathbf{r}_\mathrm{A}$ and $\mathbf{r}_\mathrm{B}$, respectively. Hence, the inter-satellite range vector ρ becomes

$$\rho(t) = ||\mathbf{r}_\mathrm{B}(t) - \mathbf{r}_\mathrm{A}(t)|| = \mathbf{e}_\mathrm{AB}(t) \cdot \mathbf{r}_\mathrm{AB}, \tag{4.1}$$

where $\mathbf{r}_\mathrm{A}$ and $\mathbf{r}_\mathrm{B}$ are expressed in inertial coordinates.

The Line-Of-Sight (LOS) unit vector $\mathbf{e}_\mathrm{AB}$ is defined by

$$\mathbf{e}_\mathrm{AB} = \frac{\mathbf{r}_\mathrm{AB}}{||\mathbf{r}_\mathrm{AB}||} = \frac{\mathbf{r}_\mathrm{AB}}{\rho}, \tag{4.2}$$

with the position difference vector $\mathbf{r}_\mathrm{AB}$ in the same direction as the unit vector $\mathbf{e}_\mathrm{AB}$.

The range rate $\dot{\rho}$ is obtained by differentiation of the range observable. The first derivative of equation (4.1) with respect to time gives

$$\dot{\rho} = \mathbf{e}_\mathrm{AB} \cdot \dot{\mathbf{r}}_\mathrm{AB} + \underbrace{\dot{\mathbf{e}}_\mathrm{AB} \cdot \mathbf{r}_\mathrm{AB}}_{0} = \mathbf{e}_\mathrm{AB} \cdot \dot{\mathbf{r}}_\mathrm{AB}, \tag{4.3}$$

which represents a projection of the relative velocity vector $\dot{\mathbf{r}}_\mathrm{AB}$ along the LOS (cf. Figure 4.1). Since the relative position vector $\mathbf{r}_\mathrm{AB}$ is perpendicular to the rate of the LOS unit vector change $\dot{\mathbf{e}}_\mathrm{AB}$ the second term $\dot{\mathbf{e}}_\mathrm{AB} \cdot \mathbf{r}_\mathrm{AB}$ equals zero. It should be noted that the obtained range rate is not the same in magnitude as the relative velocity vector magnitude.

The second derivative gives the range acceleration

$$\ddot{\rho} = \mathbf{e}_{AB} \cdot \ddot{\mathbf{r}}_{AB} + \dot{\mathbf{e}}_{AB} \cdot \dot{\mathbf{r}}_{AB}, \tag{4.4}$$

where the first term represents the projection of the relative acceleration vector $\ddot{\mathbf{r}}_{AB}$ along the LOS, and the second term represents the scalar product of the rate of the LOS unit vector change $\dot{\mathbf{e}}_{AB}$ and the relative velocity vector $\dot{\mathbf{r}}_{AB}$. To evaluate equation (4.4) the first derivative of the LOS unit vector $\dot{\mathbf{e}}_{AB}$ is required

$$\dot{\mathbf{e}}_{AB} = \frac{\partial}{\partial t}\left(\frac{\mathbf{r}_{AB}}{\rho}\right) = \frac{\dot{\mathbf{r}}_{AB}}{\rho} - \frac{\dot{\rho} \cdot \mathbf{r}_{AB}}{\rho^2} = \frac{1}{\rho}(\dot{\mathbf{r}}_{AB} - \dot{\rho} \cdot \mathbf{e}_{AB}). \tag{4.5}$$

Substituting equation (4.5) in equation (4.4) yields

$$\ddot{\rho} = \mathbf{e}_{AB} \cdot \ddot{\mathbf{r}}_{AB} + \frac{1}{\rho}(\dot{\mathbf{r}}_{AB}^2 - \dot{\rho}^2). \tag{4.6}$$

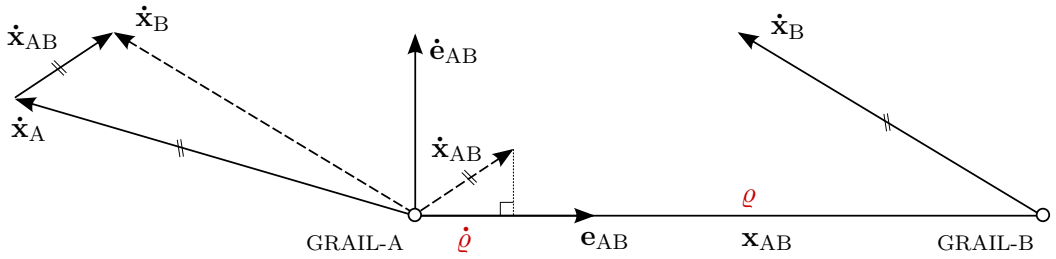

Figure 4.1: Geometry of ll-SST

Chapter 5

Analysis - Gravity field determination

The objective of this work is to estimate spherical harmonic coefficients, which represent the lunar gravity field, based on simulated data and real data. This chapter contains the second step, the so-called *analysis*, in which the contributions to the spherical harmonic coefficients of a reference gravity field are estimated.

Several approaches can be used to estimate spherical harmonic coefficients from ll-SST observations. Details on the approaches can be found in Mayer-Gürr (2006).
Here, the integral equation approach is used (Section 5.1). The solution of the equation of motion is formulated as a boundary value problem and the linearised observation equations for positions and Ka-band observations are set up. Then, the system of normal equations can be set up and solved in a Least Squares Adjustment (LSA) (Section 5.2).

Since the unknown parameter vector also contains arc-related unknowns, which are of no interest for further results, the elimination of parameters is discussed in Section 5.3.
Furthermore, variance component estimation can be used to weight the observation groups with respect to each other (Section 5.4).
The parameter estimation is accomplished using the GROOPS software package. An overview of the workflow of the analysis is given in Figure 5.1.

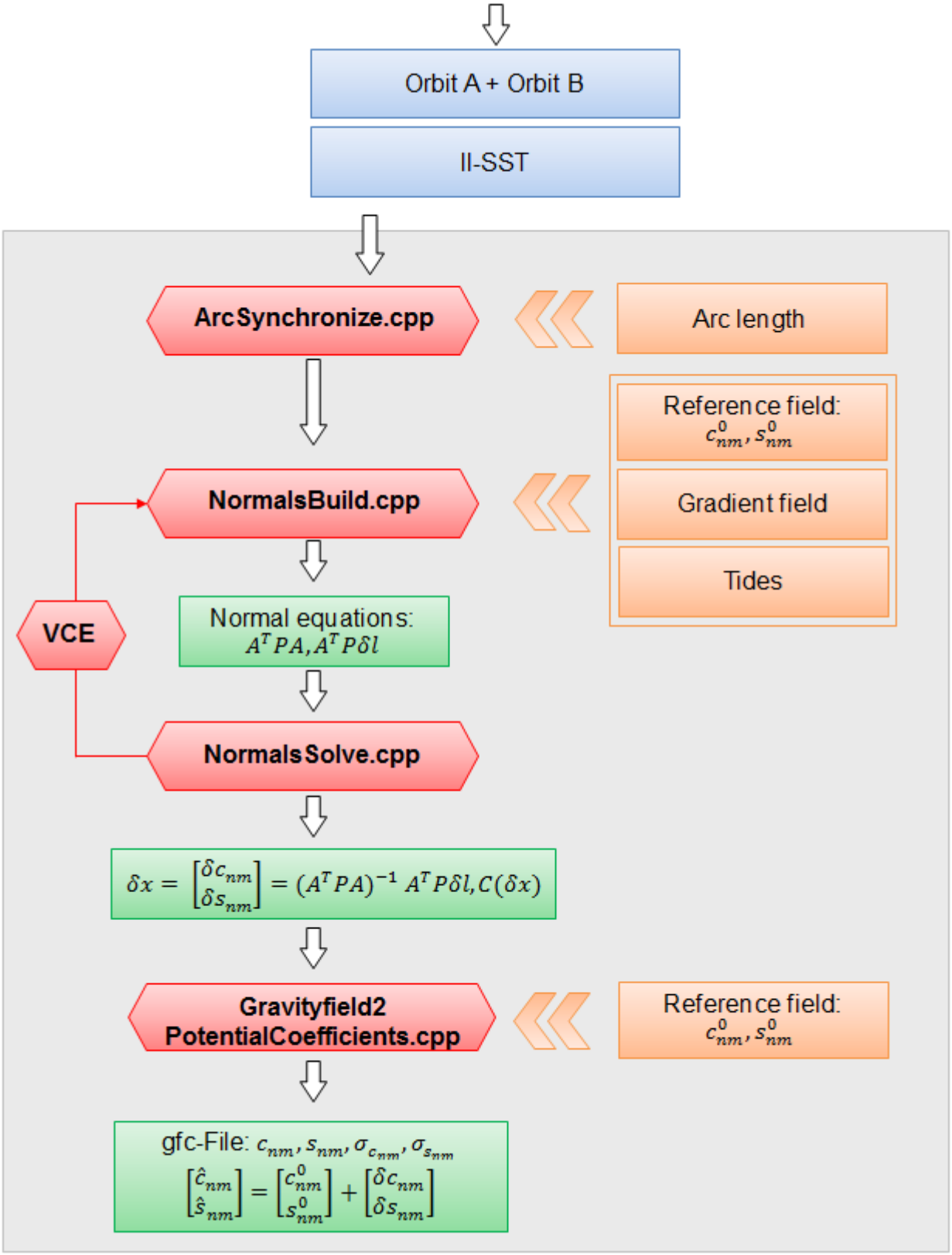

Figure 5.1: Workflow - Analysis

5.1 Integral equation approach

The integral equation approach is based on the solution of a boundary value problem. The solution of the Newton-Euler equation of motion formulated as a boundary value problem was first introduced by Schneider (1968). Based upon this, the integral equation approach was developed by Mayer-Gürr (2006) and was successfully utilized to derive gravity field models (e.g. ITG-GRACE). The integral equation approach is also denoted as short-arc approach, because the observations are subdivided into arcs, which then yields a normal equation for each arc (cf. Section 5.2).
The equations presented in this chapter are mainly taken from Mayer-Gürr (2006).

In a first step, the solution of the Newton-Euler equation of motion has to reformulated as a boundary value problem (cf. Section 5.1.1). Afterwards, the linearised observation equations can be formulated (cf. Section 5.1.2) and the system of normal equations can be established (cf. Section 5.2).

5.1.1 Boundary value problem

The Newton-Euler equation of motion is given by

$$\ddot{\mathbf{r}}(t) = \mathbf{f}(t, \mathbf{r}, \dot{\mathbf{r}}). \tag{5.1}$$

The differential equation in (5.1) is integrated twice and reformulated to form the equivalent integral equation. Using partial integration the double integral can be replaced by a single integral. The resulting integral equation is also referred to as Volterra integral equation

$$\mathbf{r}(t) = \mathbf{r}_\mathrm{A} + \dot{\mathbf{r}}_\mathrm{A}(t - t_\mathrm{A}) + \int_{t_\mathrm{A}}^{t} (t - t')\mathbf{f}(t')\, dt', \tag{5.2}$$

where $\mathbf{r}_\mathrm{A}$ and $\dot{\mathbf{r}}_\mathrm{A}$ represent the initial position and velocity. Therefore, equation (5.2) is denoted as the solution of an initial value problem.

Introducing the normalized time

$$\begin{aligned} &\tau = \frac{t - t_\mathrm{A}}{T}, \quad \tau \;\forall\; [0, 1] \\ &\text{with} \quad T = t_\mathrm{B} - t_\mathrm{A} \end{aligned} \tag{5.3}$$

and substituting equation (5.3) in equation (5.2) yields

$$\mathbf{r}(\tau) = \mathbf{r}_\mathrm{A} + \dot{\mathbf{r}}_\mathrm{A} T\tau + T^2 \int_0^{\tau} (\tau - \tau')\mathbf{f}(\tau')\, d\tau'. \tag{5.4}$$

With the epoch $\tau = 1$, the boundary value $\mathbf{r}_\mathrm{B}$ of one arc is found to be

$$\mathbf{r}_\mathrm{B} = \mathbf{r}_\mathrm{A} + \dot{\mathbf{r}}_\mathrm{A} T + T^2 \int_0^{1} (1 - \tau')\mathbf{f}(\tau')\, d\tau'. \tag{5.5}$$

By reformulating equation (5.5) to the initial velocity $\dot{\mathbf{r}}_\mathrm{A}$ and substituting this in equation (5.4)

one gets the solution of a boundary value problem

$$\begin{aligned}\mathbf{r}(\tau) &= \mathbf{r}_\mathrm{A}(1-\tau) + \mathbf{r}_\mathrm{B}\tau + T^2\int_0^\tau (\tau-\tau')\mathbf{f}(\tau')\,d\tau' - T^2\int_0^1 \tau(1-\tau')\mathbf{f}(\tau')\,d\tau' \\ &= \mathbf{r}_\mathrm{A}(1-\tau) + \mathbf{r}_\mathrm{B}\tau - T^2\int_0^\tau \tau'(1-\tau)\mathbf{f}(\tau')\,d\tau' - T^2\int_\tau^1 \tau(1-\tau')\mathbf{f}(\tau')\,d\tau',\end{aligned} \tag{5.6}$$

where the specific force function $\mathbf{f}(\tau')$ acting on the satellite along the arc and the boundary values $\mathbf{r}_\mathrm{A}$ and $\mathbf{r}_\mathrm{B}$ are unknown.

The two integrals in equation (5.6) can be summarized to

$$\mathbf{r}(\tau) = \mathbf{r}_\mathrm{A}(1-\tau) + \mathbf{r}_\mathrm{B}\tau + T^2\int_0^1 K(\tau,\tau')\mathbf{f}(\tau')\,d\tau', \tag{5.7}$$

representing the solution of the Newton-Euler equation of motion formulated as a boundary value problem. Equation (5.7) is also denoted as Fredholm integral equation of the second kind.

The integral kernel K is given by

$$K(\tau,\tau') = \begin{cases}\tau'(1-\tau) & \text{for } \tau' \le \tau \\ \tau(1-\tau') & \text{for } \tau' > \tau\end{cases}. \tag{5.8}$$

5.1.2 Linearisation

Positions

According to equation (5.7), the relation between the position $\mathbf{r}$ and the unknown parameters is non-linear. The position $\mathbf{r}$ depends on the boundary values $\mathbf{r}_\mathrm{A}, \mathbf{r}_\mathrm{B}$ and on the force function $\mathbf{f}$. Therefore, the relation to the spherical harmonic coefficients $\mathbf{x}$ is not given explicitly, but implicitly through the force function (using the chain rule of differentiation).

The parameter vector $\mathbf{x}$ summarizes the spherical harmonic coefficients up to the maximum degree n_max

$$\mathbf{x} = (c_{20}, c_{21}, s_{21}, c_{22}, s_{22}, \ldots, c_{n_\mathrm{max}n_\mathrm{max}}, s_{n_\mathrm{max}n_\mathrm{max}})^T. \tag{5.9}$$

Hence, the length of the parameter vector u is defined by the maximum degree n_max:

$$u = (n_\mathrm{max}+1)^2 - 4. \tag{5.10}$$

The linearisation according to a first-order Taylor series approximation with respect to the spherical harmonic coefficients $\mathbf{x}$ and the boundary values $\mathbf{b} = (\mathbf{r}_\mathrm{A}, \mathbf{r}_\mathrm{B})^T$ is given by

$$\mathbf{r} = \mathbf{r}_0 + \frac{\partial \mathbf{r}}{\partial \mathbf{f}}\frac{\partial \mathbf{f}}{\partial \mathbf{x}}\delta\mathbf{x} + \frac{\partial \mathbf{r}}{\partial \mathbf{b}}\delta\mathbf{b}. \tag{5.11}$$

Consequently, the representation of the linearised model of the satellite positions is given by equation (5.11).

Ka-band observations

To obtain the linearised model of the Ka-band observations, the relation between the Ka-band observations and the unknown parameters has to be established first. According to Section 4.0.2, the Ka-band observations are defined as

$$\begin{aligned}\rho &= \mathbf{e}_{\mathrm{AB}} \cdot \mathbf{r}_{\mathrm{AB}},\\ \dot{\rho} &= \mathbf{e}_{\mathrm{AB}} \cdot \dot{\mathbf{r}}_{\mathrm{AB}},\\ \ddot{\rho} &= \mathbf{e}_{\mathrm{AB}} \cdot \ddot{\mathbf{r}}_{\mathrm{AB}} + \frac{1}{\rho}(\dot{\mathbf{r}}_{\mathrm{AB}}^2 - \dot{\rho}^2).\end{aligned} \tag{5.12}$$

In equation (5.12) the relation to the unknown parameters is not given explicitly, but again implicitly through the satellite positions, which again depend on the gravity field parameters $\mathbf{x}$. Therefore, the Ka-band observations in equation (5.12) are linearised. For linearisation the partial derivatives with respect to the unknown parameters have to be build according to the chain rule, i.e. the Ka-band observations are derived with respect to the positions $\mathbf{r}$ and the positions are derived with respect to the unknown parameters $\mathbf{x}$ and $\mathbf{b}$ (cf. Equation (5.11)):

$$\begin{aligned}\frac{\partial \rho}{\partial \mathbf{x}} &= \frac{\partial \rho}{\partial \mathbf{r}_{\mathrm{AB}}}\left(\frac{\partial \mathbf{r}_{\mathrm{B}}}{\partial \mathbf{x}} - \frac{\partial \mathbf{r}_{\mathrm{A}}}{\partial \mathbf{x}}\right),\\ \frac{\partial \dot{\rho}}{\partial \mathbf{x}} &= \frac{\partial \dot{\rho}}{\partial \mathbf{r}_{\mathrm{AB}}}\left(\frac{\partial \mathbf{r}_{\mathrm{B}}}{\partial \mathbf{x}} - \frac{\partial \mathbf{r}_{\mathrm{A}}}{\partial \mathbf{x}}\right) + \frac{\partial \dot{\rho}}{\partial \dot{\mathbf{r}}_{\mathrm{AB}}}\left(\frac{\partial \dot{\mathbf{r}}_{\mathrm{B}}}{\partial \mathbf{x}} - \frac{\partial \dot{\mathbf{r}}_{\mathrm{A}}}{\partial \mathbf{x}}\right),\\ \frac{\partial \ddot{\rho}}{\partial \mathbf{x}} &= \frac{\partial \ddot{\rho}}{\partial \mathbf{r}_{\mathrm{AB}}}\left(\frac{\partial \mathbf{r}_{\mathrm{B}}}{\partial \mathbf{x}} - \frac{\partial \mathbf{r}_{\mathrm{A}}}{\partial \mathbf{x}}\right) + \frac{\partial \ddot{\rho}}{\partial \dot{\mathbf{r}}_{\mathrm{AB}}}\left(\frac{\partial \dot{\mathbf{r}}_{\mathrm{B}}}{\partial \mathbf{x}} - \frac{\partial \dot{\mathbf{r}}_{\mathrm{A}}}{\partial \mathbf{x}}\right) + \frac{\partial \ddot{\rho}}{\partial \ddot{\mathbf{r}}_{\mathrm{AB}}}\left(\frac{\partial \ddot{\mathbf{r}}_{\mathrm{B}}}{\partial \mathbf{x}} - \frac{\partial \ddot{\mathbf{r}}_{\mathrm{A}}}{\partial \mathbf{x}}\right).\end{aligned} \tag{5.13}$$

The linearised model of the Ka-band observations is given by

$$\begin{pmatrix}\rho\\ \dot{\rho}\\ \ddot{\rho}\end{pmatrix} = \begin{pmatrix}\rho_0\\ \dot{\rho}_0\\ \ddot{\rho}_0\end{pmatrix} + \mathbf{P}\begin{pmatrix}\delta\mathbf{r}_{\mathrm{AB}}\\ \delta\dot{\mathbf{r}}_{\mathrm{AB}}\\ \delta\ddot{\mathbf{r}}_{\mathrm{AB}}\end{pmatrix}, \tag{5.14}$$

with the matrix $\mathbf{P}$ containing the partial derivatives of equation (5.13)

$$\mathbf{P} = \begin{pmatrix}\frac{\partial \rho}{\partial \mathbf{r}_{\mathrm{AB}}} & 0 & 0\\ \frac{\partial \dot{\rho}}{\partial \mathbf{r}_{\mathrm{AB}}} & \frac{\partial \dot{\rho}}{\partial \dot{\mathbf{r}}_{\mathrm{AB}}} & 0\\ \frac{\partial \ddot{\rho}}{\partial \mathbf{r}_{\mathrm{AB}}} & \frac{\partial \ddot{\rho}}{\partial \dot{\mathbf{r}}_{\mathrm{AB}}} & \frac{\partial \ddot{\rho}}{\partial \ddot{\mathbf{r}}_{\mathrm{AB}}}\end{pmatrix}. \tag{5.15}$$

5.1.3 Observation equations

In this section, the formulation of the observation equations for positions and Ka-band observations is described.

Positions

The boundary value problem can be formulated according to equation (5.7) as

$$\mathbf{r}(\tau) = \mathbf{r}_{\mathrm{A}}(1-\tau) + \mathbf{r}_{\mathrm{B}}\tau - \underbrace{T^2 \int_0^1 K(\tau,\tau')\mathbf{f}(\tau')\,d\tau'}_{\mathbf{h}(\tau)}, \tag{5.16}$$

where $\mathbf{h}(\tau)$ represents the integral.

The partial derivatives of the integral with respect to the force function $\mathbf{f}$ is represented by the matrix $\mathbf{K}$, which contains a numerical integration (polynomial interpolation):

$$\mathbf{K} = \frac{\partial \mathbf{h}}{\partial \mathbf{f}} = \frac{\partial \mathbf{r}}{\partial \mathbf{f}}. \tag{5.17}$$

Equation (5.17) can be written as matrix-vector product

$$\mathbf{h} = \mathbf{K}\mathbf{f}. \tag{5.18}$$

The matrix $\mathbf{G}$ represents the linear relation between the gravity field parameters $\mathbf{x}$ and the specific force function $\mathbf{f}$. According to Section 3.2 this can also be formulated as a matrix-vector product

$$\begin{aligned} \mathbf{G} &= \frac{\partial \mathbf{f}}{\partial \mathbf{x}}, \\ \mathbf{f} &= \mathbf{G}\mathbf{x} + \mathbf{a}, \end{aligned} \tag{5.19}$$

where $\mathbf{a}$ represents the non-gravitational forces, tides and the reference field.

Hence, equation (5.11) can be reformulated to

$$\mathbf{r} = \mathbf{r}_0 + \mathbf{K}\mathbf{G}\mathbf{x} + \mathbf{B}\mathbf{b}, \tag{5.20}$$

with

$$\mathbf{B} = \frac{\partial \mathbf{r}}{\partial \mathbf{b}} = \begin{pmatrix} (1-\tau_1) & \tau_1 \\ \vdots & \vdots \\ (1-\tau_N) & \tau_N \end{pmatrix}, \quad \mathbf{b} = \begin{pmatrix} \mathbf{r}_\mathrm{A} \\ \mathbf{r}_\mathrm{B} \end{pmatrix}. \tag{5.21}$$

The relation between the observations and the unknown parameters $\mathbf{x}$ and $\mathbf{b}$ is given by equation (5.11), which can be written as equation (5.20).

To avoid errors due to inaccurate and noisy positions, the contribution of the positions to the gravity field and thus to the force function has to be taken into account. Due to the reason that the force function is depending on the position and on the gravity field, equation (5.11) has to be extended. Hence, the derivations with respect to the unknowns are given by

$$\begin{aligned} \frac{\partial \mathbf{r}}{\partial \mathbf{x}} &= \mathbf{K}\frac{\partial \mathbf{f}}{\partial \mathbf{r}}\frac{\partial \mathbf{r}}{\partial \mathbf{x}} + \mathbf{K}\frac{\partial \mathbf{f}}{\mathbf{x}}, \\ \frac{\partial \mathbf{r}}{\partial \mathbf{b}} &= \mathbf{B}\mathbf{b} + \mathbf{K}\frac{\partial \mathbf{f}}{\partial \mathbf{r}}\frac{\partial \mathbf{r}}{\partial \mathbf{b}}. \end{aligned} \tag{5.22}$$

The notation in equation (5.22) corresponds to the linearised variational equations. Reformulating equation (5.22) yields

$$\begin{aligned} \frac{\partial \mathbf{r}}{\partial \mathbf{x}}(\mathbf{I} - \mathbf{K}\frac{\partial \mathbf{f}}{\partial \mathbf{r}}) &= \mathbf{K}\frac{\partial \mathbf{f}}{\partial \mathbf{x}}, \\ \frac{\partial \mathbf{r}}{\partial \mathbf{b}}(\mathbf{I} - \mathbf{K}\frac{\partial \mathbf{f}}{\partial \mathbf{r}}) &= \mathbf{B}\mathbf{b}. \end{aligned} \tag{5.23}$$

Introducing the gravitational gradient tensor

$$\mathbf{T} = \frac{\partial \mathbf{f}}{\partial \mathbf{r}} = \begin{pmatrix} \nabla \mathbf{f}(\tau_1) & & 0 \\ & \ddots & \\ 0 & & \nabla \mathbf{f}(\tau_N) \end{pmatrix} \tag{5.24}$$

and substituting equation (5.24) in equation (5.23) yields

$$\begin{aligned} \frac{\partial \mathbf{r}}{\partial \mathbf{x}} &= (\mathbf{I} - \mathbf{KT})^{-1}\mathbf{KGx}, \\ \frac{\partial \mathbf{r}}{\partial \mathbf{b}} &= (\mathbf{I} - \mathbf{KT})^{-1}\mathbf{Bb}. \end{aligned} \tag{5.25}$$

The gravitational gradient tensor $\mathbf{T}$, which is often denoted as Marussi tensor, is comprised of the second derivatives of the gravitational potential V, this corresponds to the derivation of the force function $\mathbf{f}$ with respect to the position $\mathbf{r}$. The gravitational gradients, representing the elements of the symmetric tensor, are given by

$$\mathbf{T} = \nabla(\nabla V) = \begin{pmatrix} V_{xx} & V_{xy} & V_{xz} \\ V_{xy} & V_{yy} & V_{yz} \\ V_{xz} & V_{yz} & V_{zz} \end{pmatrix}, \tag{5.26}$$

where only five of the nine elements are mutually independent. The tensor has a vanishing trace and therefore satisfies Laplace's equation (according to equation (3.7)).
The position dependency of the observation equations is given by the gradient field.

With equation (5.25) the observation equations for the positions, velocities and accelerations of the two satellites A and B are given by

$$\begin{pmatrix} \mathbf{r}^{\mathrm{A/B}} \\ \dot{\mathbf{r}}^{\mathrm{A/B}} \\ \ddot{\mathbf{r}}^{\mathrm{A/B}} \end{pmatrix} = \begin{pmatrix} \mathbf{r}_0^{\mathrm{A/B}} \\ \dot{\mathbf{r}}_0^{\mathrm{A/B}} \\ \ddot{\mathbf{r}}_0^{\mathrm{A/B}} \end{pmatrix} + \begin{pmatrix} \mathbf{R}^{\mathrm{A/B}} \\ \dot{\mathbf{R}}^{\mathrm{A/B}} \\ \ddot{\mathbf{R}}^{\mathrm{A/B}} \end{pmatrix} \mathbf{G}^{\mathrm{A/B}}\mathbf{x} + \begin{pmatrix} \bar{\mathbf{B}}^{\mathrm{A/B}} \\ \dot{\bar{\mathbf{B}}}^{\mathrm{A/B}} \\ \ddot{\bar{\mathbf{B}}}^{\mathrm{A/B}} \end{pmatrix} \mathbf{b}, \tag{5.27}$$

with

$$\mathbf{R}^{\mathrm{A/B}} := \frac{\partial \mathbf{r}}{\partial \mathbf{f}}^{\mathrm{A/B}} = (\mathbf{I} - \mathbf{KT}^{\mathrm{A/B}})^{-1}\mathbf{K} \quad \text{and} \quad \bar{\mathbf{B}}^{\mathrm{A/B}} := \frac{\partial \mathbf{r}}{\partial \mathbf{b}}^{\mathrm{A/B}} = (\mathbf{I} - \mathbf{KT}^{\mathrm{A/B}})^{-1}\mathbf{B}. \tag{5.28}$$

Ka-band observations

Substituting equation (5.27) in equation (5.14) gives the observation equations of the Ka-band observations

$$\begin{pmatrix} \rho \\ \dot{\rho} \\ \ddot{\rho} \end{pmatrix} = \begin{pmatrix} \rho_0 \\ \dot{\rho}_0 \\ \ddot{\rho}_0 \end{pmatrix} + \mathbf{P} \begin{pmatrix} \mathbf{R}^{\mathrm{B}} - \mathbf{R}^{\mathrm{A}} \\ \dot{\mathbf{R}}^{\mathrm{B}} - \dot{\mathbf{R}}^{\mathrm{A}} \\ \ddot{\mathbf{R}}^{\mathrm{B}} - \ddot{\mathbf{R}}^{\mathrm{A}} \end{pmatrix} \begin{pmatrix} \mathbf{G}^{\mathrm{B}} \\ \mathbf{G}^{\mathrm{A}} \end{pmatrix} \mathbf{x} + \mathbf{P} \begin{pmatrix} \bar{\mathbf{B}}^{\mathrm{B}} - \bar{\mathbf{B}}^{\mathrm{A}} \\ \dot{\bar{\mathbf{B}}}^{\mathrm{B}} - \dot{\bar{\mathbf{B}}}^{\mathrm{A}} \\ \ddot{\bar{\mathbf{B}}}^{\mathrm{B}} - \ddot{\bar{\mathbf{B}}}^{\mathrm{A}} \end{pmatrix} \begin{pmatrix} \mathbf{b}^{\mathrm{B}} \\ \mathbf{b}^{\mathrm{A}} \end{pmatrix}. \tag{5.29}$$

Observation equations - Positions & Ka-band observations

The observation equations for satellite positions and Ka-band observations are given by

$$\mathbf{l}_{\mathrm{POD}}^{\mathrm{A/B}} = \mathbf{R}^{\mathrm{A/B}}\mathbf{G}^{\mathrm{A/B}}\mathbf{x} + \bar{\mathbf{B}}^{\mathrm{A/B}}\mathbf{b}^{\mathrm{A/B}}, \tag{5.30}$$

and

$$\mathbf{l}_{\mathrm{KBR}} = \mathbf{P}\begin{pmatrix}\mathbf{R}^{\mathrm{B}} - \mathbf{R}^{\mathrm{A}} \\ \dot{\mathbf{R}}^{\mathrm{B}} - \dot{\mathbf{R}}^{\mathrm{A}} \\ \ddot{\mathbf{R}}^{\mathrm{B}} - \ddot{\mathbf{R}}^{\mathrm{A}}\end{pmatrix}\begin{pmatrix}\mathbf{G}^{\mathrm{B}} \\ \mathbf{G}^{\mathrm{A}}\end{pmatrix}\mathbf{x} + \mathbf{P}\begin{pmatrix}\bar{\mathbf{B}}^{\mathrm{B}} - \bar{\mathbf{B}}^{\mathrm{A}} \\ \dot{\bar{\mathbf{B}}}^{\mathrm{B}} - \dot{\bar{\mathbf{B}}}^{\mathrm{A}} \\ \ddot{\bar{\mathbf{B}}}^{\mathrm{B}} - \ddot{\bar{\mathbf{B}}}^{\mathrm{A}}\end{pmatrix}\begin{pmatrix}\mathbf{b}^{B} \\ \mathbf{b}^{A}\end{pmatrix}, \tag{5.31}$$

with the reduced observations

$$\begin{aligned}\mathbf{l}_{\mathrm{POD}}^{\mathrm{A/B}} &= \mathbf{r}^{\mathrm{A/B}} - \mathbf{r}_0^{\mathrm{A/B}}, \\ \mathbf{l}_{\mathrm{KBR}} &= \begin{pmatrix}\rho - \rho_0 \\ \dot{\rho} - \dot{\rho}_0 \\ \ddot{\rho} - \ddot{\rho}_0\end{pmatrix}.\end{aligned} \tag{5.32}$$

For details on the formulas and on the computation of the approximate values $\mathbf{r}_0^{\mathrm{A/B}}$, ρ_0, $\dot{\rho}_0$ and $\ddot{\rho}_0$ please refer to Mayer-Gürr (2006).

5.2 Normal equations

A system of linear equations can be established with the linearised observation equations given in equations (5.30) and (5.31)

$$\delta\mathbf{l}_i = \mathbf{A}_i\delta\mathbf{x} + \mathbf{B}_i\delta\mathbf{b}_i + \mathbf{e}_i, \tag{5.33}$$

where $\mathbf{x}$ denotes the unknown spherical harmonic coefficients and $\mathbf{b}$ represents the boundary values.

Equation (5.33) can be reformulated to

$$\delta\mathbf{l}_i = \underbrace{\begin{pmatrix}\mathbf{A}_i & \mathbf{B}_i\end{pmatrix}}_{\mathbf{H}_i}\underbrace{\begin{pmatrix}\delta\mathbf{x} \\ \delta\mathbf{b}_i\end{pmatrix}}_{\delta\mathbf{z}} + \mathbf{e}_i, \tag{5.34}$$

with the vector of residual observations $\delta\mathbf{l}_i$ and the vector of residual parameters $\delta\mathbf{z} = \mathbf{z} - \mathbf{z}_0$ given by

$$\begin{aligned}\delta\mathbf{z}_i &= \begin{pmatrix}\delta\mathbf{x} \\ \delta\mathbf{b}_i\end{pmatrix}, \\ \delta\mathbf{l}_i &= \mathbf{l}_i - \mathbf{l}_i^0,\end{aligned} \tag{5.35}$$

where the subscript i denotes one arc.

If the noise vector $\mathbf{e}$ is assumed to follow a Gaussian normal distribution with zero mean, the overdetermined system of equations in (5.34) can be solved by a LSA:

$$\mathbf{e}^T\mathbf{P}\mathbf{e} \rightarrow \mathrm{MIN!}, \tag{5.36}$$

with the inverse matrix of cofactors $\mathbf{Q}_{ll}$ used as weight matrix $\mathbf{P}$ for the observations. The covariance matrix

$$\Sigma(\mathbf{l}) = \sigma_0^2 \mathbf{Q}_{ll} = \sigma_0^2 \mathbf{P}^{-1} \tag{5.37}$$

is decomposed into the matrix of cofactors $\mathbf{Q}_{ll}$ and the scalar factor σ_0^2, which is denoted as variance of unit weight or a-priori variance factor.

Minimizing (5.36) yields the normal equations

$$\mathbf{N}\delta\hat{\mathbf{z}} = \mathbf{n} \quad \text{with} \quad \mathbf{N} = \mathbf{H}^T\mathbf{P}\mathbf{H} \quad \text{and} \quad \mathbf{n} = \mathbf{H}^T\mathbf{P}\delta\mathbf{l}. \tag{5.38}$$

Since the normal equation matrix $\mathbf{N}$ contains all observations of all arcs, it can be described by a summation

$$\mathbf{N} = \sum_{i=1}^{m} \mathbf{H}_i^T \mathbf{P}_i \mathbf{H}_i, \tag{5.39}$$

with the total number of arcs m.

In analogy to equation (5.39), the right-hand side vector $\mathbf{n}$ becomes

$$\mathbf{n} = \sum_{i=1}^{m} \mathbf{H}_i^T \mathbf{P}_i \delta\mathbf{l}_i. \tag{5.40}$$

It is assumed that observations of different arcs are uncorrelated, therefore the weight matrix $\mathbf{P}$ has a block-diagonal structure:

$$\mathbf{P} = \begin{pmatrix} \mathbf{P}_1 & & & \\ & \mathbf{P}_2 & & \\ & & \ddots & \\ & & & \mathbf{P}_m \end{pmatrix}. \tag{5.41}$$

Finally, the estimated gravity field and arc-related parameters are given by

$$\begin{aligned} \hat{\mathbf{x}} &= \delta\hat{\mathbf{x}} + \mathbf{x}_0, \\ \hat{\mathbf{b}} &= \delta\hat{\mathbf{b}} + \mathbf{b}_0, \end{aligned} \tag{5.42}$$

where $\mathbf{x}_0$ and $\mathbf{b}_0$ represent approximate values.

The estimate of the variance of unit weight, which is also called a-posteriori variance factor, is obtained by evaluating

$$\hat{\sigma}_0^2 = \frac{\hat{\mathbf{e}}^T\mathbf{P}\hat{\mathbf{e}}}{r}, \tag{5.43}$$

with

$$\hat{\mathbf{e}} = \mathbf{H}\delta\hat{\mathbf{z}} - \delta\mathbf{l}, \tag{5.44}$$

where the redundancy r represents the number of degrees of freedom of the adjustment problem.

5.3 Elimination of parameters

According to equation (5.34) the unknown parameters include the spherical harmonic coefficients $\mathbf{x}$ and the arc-related boundary values $\mathbf{y}$. Therefore, there are six unknowns related to the boundary values of one satellite for each arc. This leads to a large number of parameters, more than unknown gravity field parameters. Since the numerical values of these boundary elements are not of interest, the arc-related unknowns are eliminated from the system of normal equations.
If ranges are used as ll-SST observations an unknown range bias (cf. Section 6.1) has to be estimated, which can be eliminated subsequently.

The system of normal equations for one arc is given by

$$\begin{pmatrix} \mathbf{A}^T\mathbf{A} & \mathbf{A}^T\mathbf{B} \\ \mathbf{B}^T\mathbf{A} & \mathbf{B}^T\mathbf{B} \end{pmatrix} \begin{pmatrix} \delta\hat{\mathbf{x}} \\ \delta\hat{\mathbf{y}} \end{pmatrix} = \begin{pmatrix} \mathbf{A}^T\delta\mathbf{l} \\ \mathbf{B}^T\delta\mathbf{l} \end{pmatrix}, \tag{5.45}$$

with

$$\begin{aligned} &\mathbf{N}_{11} = \mathbf{A}^T\mathbf{A}, \quad \mathbf{N}_{12} = \mathbf{A}^T\mathbf{B}, \quad \mathbf{N}_{22} = \mathbf{B}^T\mathbf{B}, \\ &\mathbf{n}_1 = \mathbf{A}^T\delta\mathbf{l}, \quad \mathbf{n}_2 = \mathbf{B}^T\delta\mathbf{l}. \end{aligned} \tag{5.46}$$

The vector $\delta\hat{\mathbf{x}}$ should be estimated without solving the whole system. The reduced system of normal equations is given by

$$\bar{\mathbf{N}}\delta\hat{\mathbf{x}} = \bar{\mathbf{n}} \quad \text{with} \quad \bar{\mathbf{N}} = \mathbf{N}_{11} - \mathbf{N}_{12}\mathbf{N}_{22}^{-1}\mathbf{N}_{12}^T \quad \text{and} \quad \bar{\mathbf{n}} = \mathbf{n}_1 - \mathbf{N}_{12}\mathbf{N}_{22}^{-1}\mathbf{n}_2. \tag{5.47}$$

Details on the elimination of parameters can be found in Kaula (2000) and in Section 5.3 in Mayer-Gürr (2006).

In contrast to the parameter elimination, additional observation equations can be added to the system of normal equation. Hence, additional parameters (e.g. Love numbers) can be estimated (cf. Section 7.5).

5.4 Variance component estimation

In parameter estimation the a-posteriori variance factor (cf. equation (5.43)) is an estimator for the common variance level of the observations. It can be used as a plausibility check for the a-priori assumptions made. In the stochastic model in equation (5.37) it is assumed that the relations of variance levels among the observations are known, since they are determined by the cofactor matrix $\mathbf{Q}_{ll}$. Here, observations with different accuracies (positions and Ka-band observations) are used within the observation groups. Therefore, the relative weighting between the observations is essential.

Variance component estimation (VCE) enables the estimation of different levels of accuracies for multiple observation groups, which corresponds here to short arcs. Whereas, the internal

relations (between orbit and Ka-band observations) of each arc must be fixed a-priori.

The estimated solution $\delta\hat{\mathbf{x}}$ of the combined observation equations is determined by the normal equation system. The total system is accumulated by the weighted sum of the normal equations of the individual arcs

$$\begin{aligned} &\mathbf{N}\delta\hat{\mathbf{x}} = \mathbf{n}, \\ &\text{with} \quad \mathbf{N} = \sum_k \frac{1}{\hat{\sigma}_k^2}\mathbf{N}_k = \sum_k \frac{1}{\hat{\sigma}_k^2}\mathbf{A}_k^T\mathbf{P}_k\mathbf{A}_k \quad \text{and} \quad \mathbf{n} = \sum_k \frac{1}{\hat{\sigma}_k^2}\mathbf{n}_k = \sum_k \frac{1}{\hat{\sigma}_k^2}\mathbf{A}_k^T\mathbf{P}_k\delta\mathbf{l}_k, \end{aligned} \tag{5.48}$$

where the arc-dependent parameters $\mathbf{y}$ have been eliminated according to Section 5.3.

The weighting is determined by the reciprocal of the normal equation systems individual variances $\frac{1}{\hat{\sigma}_k^2}$. The variance $\hat{\sigma}_k^2$ is given by

$$\hat{\sigma}_k^2 = \frac{\Omega_k}{r_k}, \tag{5.49}$$

with the square sum of the residuals of the k^{th} arc

$$\Omega_k = \hat{\mathbf{e}}_k^T\mathbf{P}_k\hat{\mathbf{e}}_k = \delta\hat{\mathbf{x}}^T\mathbf{N}_k\delta\hat{\mathbf{x}} - 2\mathbf{n}_k^T\delta\hat{\mathbf{x}} + \delta\mathbf{l}_k^T\mathbf{P}_k\delta\mathbf{l}_k, \tag{5.50}$$

and the partial redundancy

$$r_k = m_k - \frac{1}{\hat{\sigma}_k^2}\text{trace}(\mathbf{N}_k\mathbf{N}^{-1}), \tag{5.51}$$

where m_k is the number of observations.

The total redundancy $\sum_k r_k = m - n$ is equal to the sum of the partial redundancies. To determine the k variance components the solutions $\delta\hat{\mathbf{x}}$ and the variance components $\hat{\sigma}_k^2$ themselves are needed. Therefore, the variance component estimation is done iteratively or an a-priori solution is provided. In equation (5.50) and (5.51) the estimated solution and the variances of the previous iteration step are used.

Details on the VCE can be found in Koch and Kusche (2001) and in Mayer-Gürr (2006).

Chapter 6

Processing of real data

In this chapter the used data products and the preprocessing of the real data are described. The available data products are described in Section 6.1. The preprocessing in Section 6.2 includes the synchronization of the data products and the outlier detection within the Ka-band observations.

After preprocessing, the linearised observation equations (given in Section 5.1.3) can be used to estimate the lunar gravity field from real data, i.e. the analysis described in Chapter 5 can be done using the GROOPS software package. The results obtained by the analysis are the spherical harmonic coefficients, which represent the lunar gravity field.
In a next step, the obtained results can be compared to previous lunar gravity field solutions (cf. Section 8).

6.1 Available data products

The LGRS CDR data set contains calibrated and re-sampled Level 1A and 1B science data from each Lunar Gravity Ranging System. For the definitions of the NASA processing levels please refer to Table 2.2 in Section 2.3.

The following Level 1B data products have been used for the real data analysis:

- Satellite orbit solutions in a Moon-centered inertial frame for GRAIL-A and GRAIL-B (GNI1B)
- Ka-band ranging data (KBR1B)

Both data products are available for the duration of GRAIL's PM (March-May 2012) and have a sampling of 5 seconds, but they are not synchronous (cf. Section 6.2.1). The abbreviations of the data products are according to Kahan (2012).

The LGRS CDR data set is available at the Geosciences Node of NASA's PDS [1]. The data set is subdivided into directories by level and by date, i.e. one subdirectory contains all available data products for one level and date.

[1] http://geo.pds.nasa.gov/missions/grail/default.htm

6.1.1 Orbit

Since direct (radio) tracking of the satellites on the lunar farside is impossible, kinematic orbits can not be provided. Additionally, epoch-wise (kinematic) positioning is impossible from non-synchronized observations. Therefore, the only available satellite orbit solutions are reduced-dynamic orbits.

Reduced-dynamic orbits depend to some extent on the gravity field model underlying the orbit estimation. Hence, they are often considered as inappropriate for gravity field determination. Here, the orbit is not directly used for lunar gravity field determination, but "only" for geo-location (cf. Section 5.1).

The orbital solutions for the two spacecraft GRAIL-A and GRAIL-B are available in two different frames:

1. EME2000 Lunar-centered solar system barycentric frame (GNI1B)
2. DE 421 Lunar body-fixed frame (GNV1B)

With the body-fixed coordinates contained in the daily GNV1B ASCII-files, the groundtracks of the satellites can be calculated easily by transforming the given Cartesian coordinates to spherical coordinates (cf. Section 3.5.4). The groundtrack of GRAIL-A for one day during the PM is shown in Figure 6.1. During the 82-day Science Phase the Moon rotates three times underneath the GRAIL orbit.

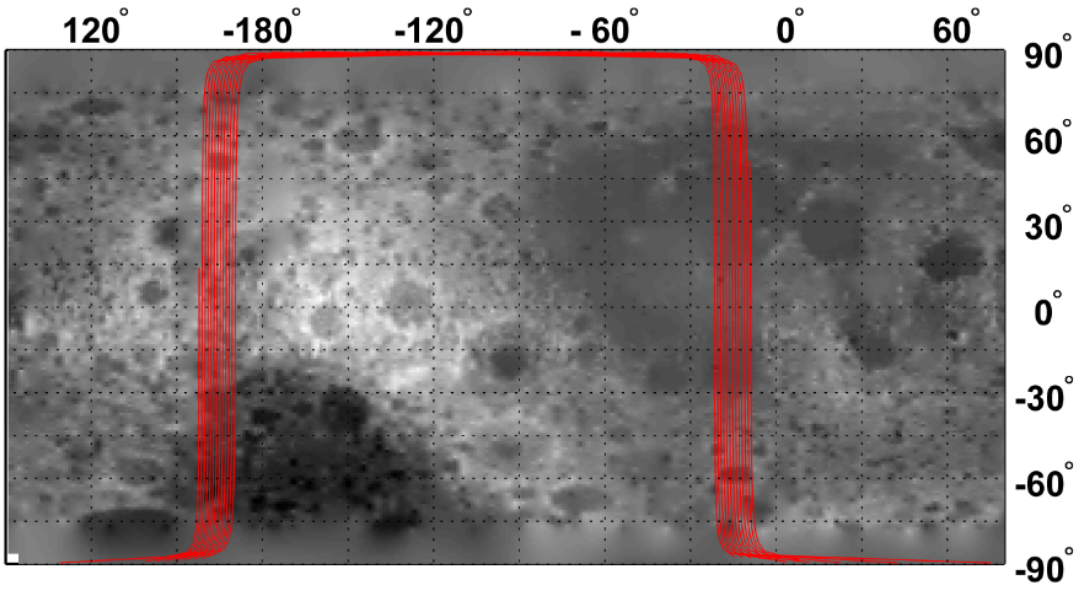

Figure 6.1: Groundtrack of the spacecraft GRAIL-A on 5th March 2012. The projection is a cylindrical Plate Carrée projection, centered about 270° eastern longitude.

Using the GRAIL orbit data for both spacecraft the separation distance and the orbital altitude during the PM phase can be determined. The results are shown in Figure 6.2. During the three 27.3-day mapping cycles the separation distance is varying between 82-218 km and the mean orbit altitude is about 55 km (± 35 km) (cf. Section 2.2.2).

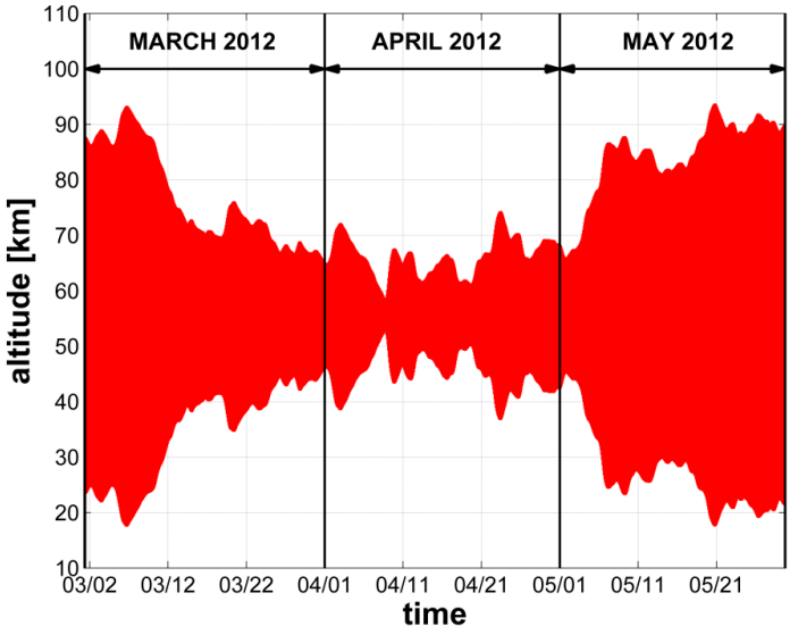

(a) Orbital altitude

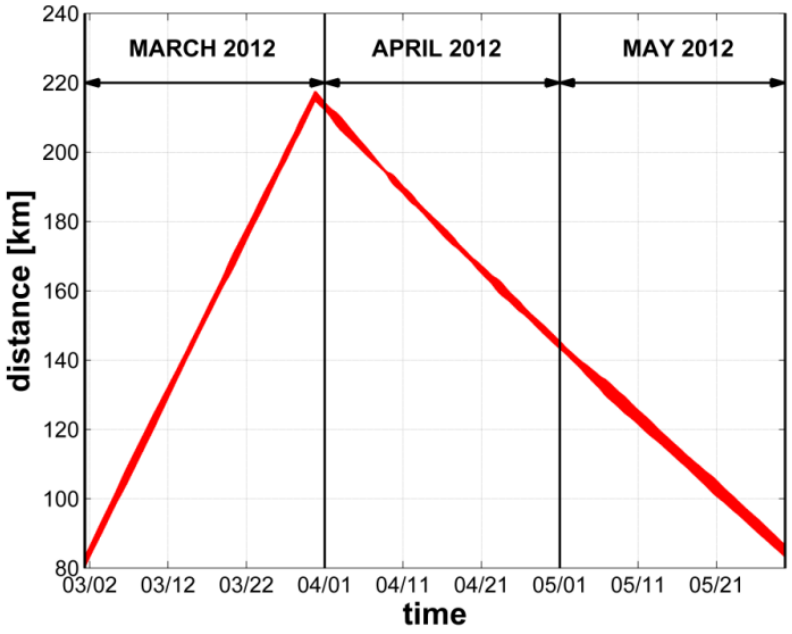

(b) Separation distance

Figure 6.2: Spacecraft separation distance and orbital altitude during GRAIL's PM. Altitudes are relative to the lunar mean radius of 1737.4 km.

The varying separation distance (cf. Fig. 6.2) is optimal for recovering a global lunar gravity field. The determination of local and regional spatial features is not that sensitive to the separation distance, while the maximum separation is ideal for the determination of the long-wavelength components of the gravity field, such as tides and the lunar core parameters. Aside from that, the separation distances are designed to ensure that there is no degradation of the Ka-band signal due to multipath from the lunar surface. Furthermore, a constant separation distance causes a degradation of the gravity field for wavelength equal to the separation distance. Therefore, the separation distance was chosen to vary between 80 km and 220 km. But nevertheless, the spacecraft altitude has most influence on the resolution of the gravity field (Konopliv et al., 2013).

6.1.2 Ka-band observations

The Ka-band data products (KBR1B) provide the biased Dual One Way Range (DOWR) between GRAIL-A and GRAIL-B, which corresponds to the true range plus an unknown bias. The biased range is not corrected for the time of flight or antenna offset from the Center of Mass (CoM). These corrections are contained in the file and have to be applied.
In addition, the ranging data also contains the first and second derivatives of the biased DOWR and the associated time of flight and antenna offset corrections.

The biased DOWR ρ_{DOWR} is formed by

$$\rho_{\mathrm{DOWR}}(t) = c \cdot \frac{\Phi_{\mathrm{AB}}(t) + \Phi_{\mathrm{BA}}(t)}{f_{\mathrm{A}} + f_{\mathrm{B}}}, \tag{6.1}$$

with

$c \ldots$ speed of light,
$\Phi_{\mathrm{AB}} = \varphi_{\mathrm{A}} - \varphi^{\mathrm{B}} \ldots$ differential phase measurement at GRAIL-A,
$\Phi_{\mathrm{BA}} = \varphi_{\mathrm{B}} - \varphi^{\mathrm{A}} \ldots$ differential phase measurement at GRAIL-B,
$\varphi_{\mathrm{A/B}} \ldots$ reference phase of spacecraft A/B,
$\varphi^{\mathrm{A/B}} \ldots$ received phase transmitted by spacecraft A/B,
$f_{\mathrm{A}} \ldots$ Ka-band carrier frequency transmitted by GRAIL-A,
$f_{\mathrm{B}} \ldots$ Ka-band carrier frequency transmitted by GRAIL-B. (6.2)

As mentioned before, the provided Ka-band observations have to be corrected. The corrected range, range rate, and range acceleration are computed by adding the time of flight correction and the antenna offset correction to the DOWR, range rate, or range acceleration observations:

corrected range = biased range + light time correction + antenna offset correction.

For the range rates and range accelerations, corresponding corrections are added accordingly. Further details on the orbit and Ka-band observations can be found in Kahan (2012).

6.2 Preprocessing

6.2.1 Synchronization - Polynomial interpolation

The orbit data and the Ka-band data have to be synchronized, since there is a time-shift of one second between the data sets. The synchronization is achieved by using a interpolation polynomial, i.e. the less accurate orbit data is interpolated to the epochs of the Ka-band data.

The new epoch is computed with a polynomial interpolation of degree M using the close-by $M+1$ equally sampled epochs. The interpolation point, representing the new data point, should be nearly in the middle of the interval, because the polynomial is oscillating at the edges of the interval. Here, a polynomial of degree 7 has been used for the interpolation.

The interpolation of the orbit data is done by evaluating a piecewise adjusted polynomial. Hence, for each interpolated data point a new interpolation polynomial is used (cf. Section 3.7.1)

$$\mathbf{r}(\tau) \approx \sum_{n=0}^{M} \mathbf{a}_n \tau^n, \tag{6.3}$$

where the polynomial coefficients are represented by $\mathbf{a}_n$. The time variable $\tau = t_k + \tau_j$ is defined by the degree of the used polynomial and the sampling Δt of the data points.

The system of linear equations given in equation (6.3) can be written as matrix-vector product

$$\begin{pmatrix} \mathbf{r}(t_k+\tau_0) \\ \vdots \\ \mathbf{r}(t_k+\tau_M) \end{pmatrix} = \underbrace{\begin{pmatrix} 1 & \tau_0 & \tau_0^2 & \dots & \tau_0^M \\ \vdots & \vdots & \vdots & & \vdots \\ 1 & \tau_M & \tau_M^2 & \dots & \tau_M^M \end{pmatrix}}_{\mathbf{W}} \begin{pmatrix} \mathbf{a}_0 \\ \vdots \\ \mathbf{a}_M \end{pmatrix}, \tag{6.4}$$

with

$$\tau_j = 1 - (j - \frac{M+1}{2}) \cdot \Delta t \quad \text{if} \quad M = \text{odd},$$

where $\tau = 0$ corresponds to the interpolation point $\mathbf{r}(t_k)$. The coefficients of the inverse matrix $\mathbf{W}^{-1}$ are denoted as w_{nj}.

The polynomial coefficients $\mathbf{a}_n$ are determined by solving the system of linear equations in (6.4). The solution is given by

$$\mathbf{a}_n = \sum_{j=0}^{M} w_{nj} \mathbf{r}(t_k + \tau_j). \tag{6.5}$$

Substituting equation (6.5) in equation (6.3) gives

$$\mathbf{r}(\tau) = \sum_{n=0}^{M} \tau^n \sum_{j=0}^{M} w_{nj} \mathbf{r}(t_k + \tau_j). \tag{6.6}$$

Since the polynomial is only evaluated for $\tau = 0$, equation (6.6) simplifies to

$$\mathbf{r}(0) = \sum_{j=0}^{M} w_{0j} \mathbf{r}(t_k + \tau_j). \tag{6.7}$$

For each interpolated data point a new polynomial has to be determined, which is then evaluated for $\tau = 0$. The polynomial is shifted point-by-point over the equally sampled orbit data, therefore the coefficients w_{0j} have to be determined only once. The interpolation can only be done if enough data points are close by, i.e. the interpolation is not possible at the edges and in the case of data gaps.

QR decomposition

Within the GROOPS software package the system of linear equations is solved using the QR decomposition (or QR factorization). Therefore, equation (6.3) is rewritten to

$$\mathbf{b} = \mathbf{A}\mathbf{x}. \tag{6.8}$$

The real square matrix $\mathbf{A}$ can be decomposed as

$$\mathbf{A} = \mathbf{Q}\mathbf{R}, \tag{6.9}$$

where $\mathbf{Q}$ is an orthogonal matrix. Due to the orthogonality ($\mathbf{Q}^T\mathbf{Q} = \mathbf{Q}\mathbf{Q}^T = \mathbf{I}$) the inverse matrix $\mathbf{Q}^{-1}$ is equivalent to the transpose matrix $\mathbf{Q}^T$. The matrix $\mathbf{R}$ is an upper triangle matrix.

Substituting equation (6.9) in equation (6.8) yields

$$\mathbf{Q}\mathbf{R}\mathbf{x} = \mathbf{b}. \tag{6.10}$$

Equation (6.10) can be reformulated to

$$\mathbf{R}\mathbf{x} = \mathbf{Q}^T\mathbf{b}. \tag{6.11}$$

With $c := \mathbf{Q}^T\mathbf{b}$ equation (6.11) can be solved by back-substitution.
In general, the QR factorization is more expensive to compute, but it is less sensitive to ill-conditioning than the LU factorization, i.e. it is numerically more stable.

Polynomial interpolation - Validation

For simulated data it can be shown that the polynomial interpolation can be done with sufficient accuracy. Therefore, a simulated data set is reduced in sampling and shifted by one second and then compared to the simulated solution calculated beforehand. The absolute value of the differences between the interpolated positions and the reference orbit are shown in Figure 6.3. The differences are less than 1 mm, i.e. the differences are several magnitudes lower than the orbit accuracy. Therefore, the polynomial interpolation can be used to synchronize the orbit data.

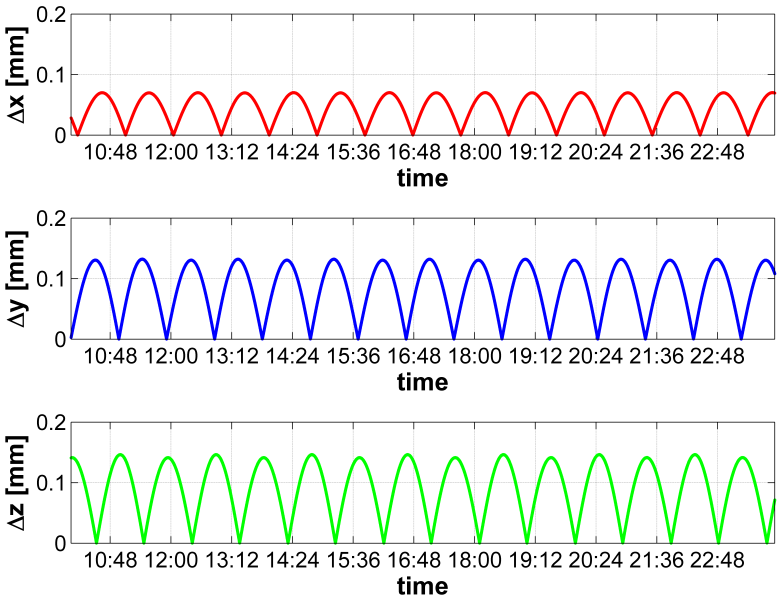

Figure 6.3: Simulated data set: residuals between interpolated and reference orbit

6.2.2 Outlier detection

The preprocessing also includes the detection of large outliers. The detection of blunders is done empirically for the ranges, range rates and range acceleration contained in the Ka-band data product. The comparison with SST-observations derived from the orbit is not reasonable, due to the fact that the orbit is less accurate and may contain outliers as well.

For outlier detection two successive values of the Ka-band observations are compared and if the difference between those values exceeds a certain threshold, the observation is classified as an outlier and is deleted from the data set. The outlier detection is done separately for ranges, range rates and range accelerations; but if a outlier is detected all observations of the corresponding epoch are removed from the data set. It should be noted that two successive values are only compared if the time difference between these values corresponds to the sampling of 5 seconds.

The empirical values for the outlier detection are chosen as follows:

- ranges: 80 [m]
- range rates: 0.5 [m/s]
- range accelerations: 0.0009 [m/s^2]

The range observations may contain jumps due to phase breaks (cf. Section 6.1). Those jumps should be detected, since most of the time outliers occur between those jumps.

Figures 6.4 to 6.6 show the ranges, range rates and range accelerations before (red) and after (green) outlier detection. It is visible, that large blunders can be detected with this method. But to ensure the elimination of all outliers a VCE is done, i.e. the arcs containing outliers are down-weighted (cf. Section 5.4).

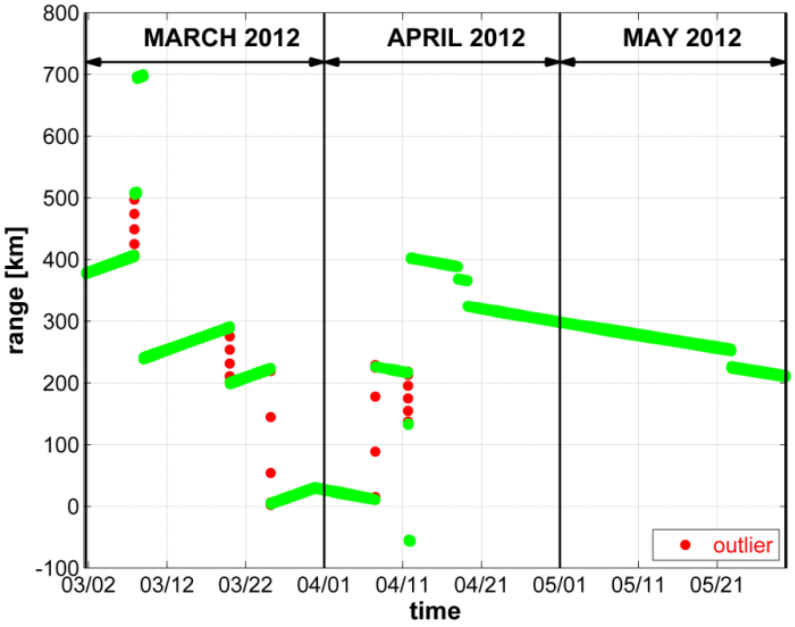

Figure 6.4: Outlier detection - Range

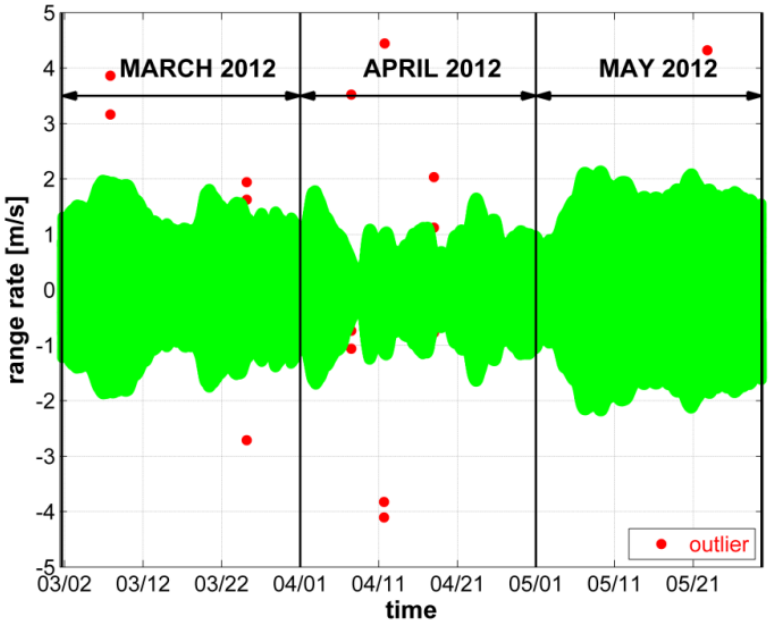

Figure 6.5: Outlier detection - Range rate

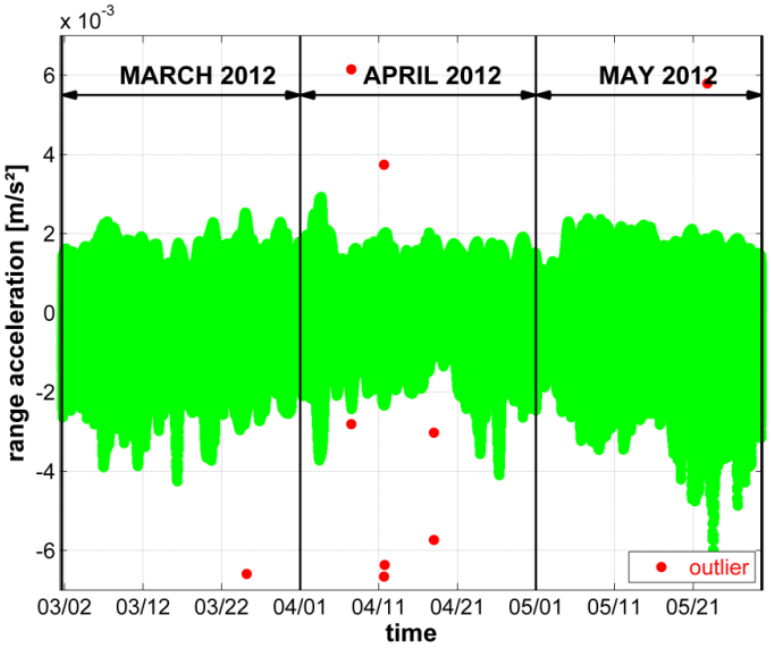

Figure 6.6: Outlier detection - Range acceleration

In total, 120 outliers were detected. This corresponds to less than 0.01% of the total data.

After outlier detection, the observations were subdivided into arcs of a predefined length. If a data gap occurs in one of the data sets a new arc starts after the data gap.

Chapter 7

Results - Simulation studies

The estimation of the spherical harmonic coefficients is based on the simulated orbit and Ka-band observations. Details on the modeling parameters used for the observation simulation are given in Section 7.1.
Several simulation scenarios have been evaluated and are presented in Section 7.2, 7.3 and 7.4. The idea behind the closed-loop simulation scenarios is to prove the correct performance of the algorithm, showing how well the gravity field can be recovered from simulated data. Furthermore, the influence of individual parameters (used in the synthesis and/or analysis) on the results is investigated using different simulation scenarios.
Finally, the lunar Love numbers used as input for the simulation of the lunar tides are considered, showing that the analysis works properly if additional parameters are estimated.

The purpose of the sensitivity studies is to validate the used method and to analyse the achieved results. Besides, these simulations are meant to prepare for the use of real data.

7.1 Simulation - Modeling parameters

7.1.1 Simulated orbit and Ka-band observations

The simulated data set consists of orbit and ll-SST observations for a period of 30 days with a sampling of 5 seconds (0.2 Hz). This corresponds to the first mapping cycle of the GRAIL PM. In Table 7.1 the parameters used for the orbit integration of the two spacecraft GRAIL-A and GRAIL-B are given. To be consistent with the real data, the initial state vectors are obtained from the real orbit data.

The orbit is simulated based on the lunar gravity field model JGL165P1 [1]. The simulation is complete to degree and order (d/o) 165. Therefore, the reference field JGL165P1 is regarded as the "true" gravity field for all conducted simulation studies.
Using the simulated orbit data, the ll-SST observations can be derived (cf. Chapter 4). In a first step, the simulated observations are noise-free.

[1] available online at `http://icgem.gfz-potsdam.de/ICGEM/ICGEM.html`

Table 7.1: Orbital parameters

Gravitational parameter GM	$0.4902801056 \cdot 10^{13}$ $m^3\,s^{-2}$
Lunar radius R	1 738 000 m
Initial state vector	retrieved from real data (GNI1B)
Reference field	JGL165P1
Ephemeris file	JPL DE421
Sampling	5 s
Simulation period	1 month (01-Mar-2012 to 31-Mar-2012)
Inclination	89.9° w.r.t lunar equator
Altitude	~ 50 km (± 35) km
Separation distance	$\sim 80 - 200$ km

In a next step, white noise is added to the observations. In principle, all observations are inaccurate due to some kind of stochastic error. Here, the errors are assumed to come from a random process that causes noise in the data. Hence, the observations are contaminated with white noise with zero mean, scaled by an appropriate standard deviation for the positions and Ka-band observations, respectively. The observations are assumed to be uncorrelated.
Since there is no detailed information about the accuracies of the orbit and Ka-band observations available, the accuracies have to be assumed based on knowledge from other missions.
For the LRO mission the total position accuracy was found to be around 12 m, using Doppler tracking data, crossovers and SLR data (Mazarico et al., 2012). Therefore, white noise of 10 m is added to the orbit positions in each direction, i.e. the along-track, cross-track and radial accuracies are assumed to have an equal noise level. Usually, the orbit accuracy in radial direction is much better than the other two directions, but for simplification all directions are assumed to have the same accuracy.
The Gaussian noise associated with the Ka-band observations is added to the simulated ll-SST data; a constant noise of 1 μm is applied for the ranges. For the range rates a white noise of 1 μm/s is added, based on the knowledge from the GRACE mission.
An overview of the different noise levels added to the simulated observations can be found in Table 7.2.

Table 7.2: Noise levels - Simulated observations

Observation	Noise level
Orbit	10 m in each direction
Ka-band (ranges)	1 μm
Ka-band (range rates)	1 μm/s

7.2 Closed-loop scenario

The performance of the synthesis and analysis can be proven by closed-loop simulation scenarios (cf. Figure 7.1). The orbit is simulated based on a reference gravity field, which is a known lunar gravity field model (JGL165P1). If no non-conservative forces are considered, the orbit perturbations reflect the a-priori reference gravity field. Using the simulated positions and the Ka-band observations between the two spacecraft, the spherical harmonic coefficients of the lunar gravity field can be estimated. Comparing the recovered coefficients to the a-priori chosen reference field shows the absolute accuracy of the used approach. Based on the spherical harmonic coefficients further functionals of the gravitational potential (cf. Section 3.2.1), such as selenoid heights or free-air anomalies, can be derived.

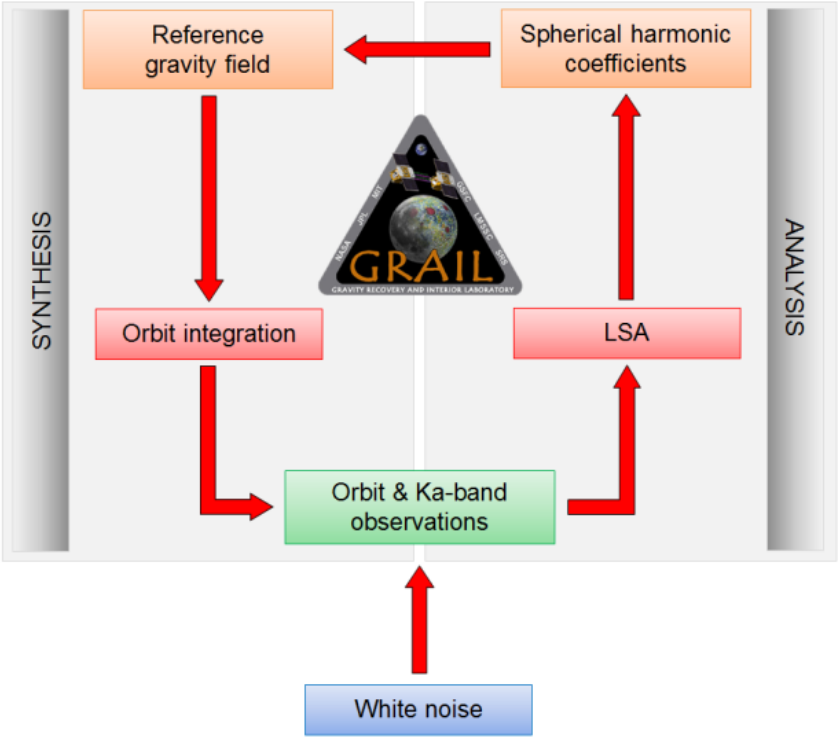

Figure 7.1: Closed-loop simulation scenario

7.2.1 Noise free

In this perfect simulation scenario, all simulated observations are noise free and the weight matrix becomes a unit matrix. Hence, there is no inconsistency due to noise or spectral aliasing. Therefore, noise free simulations are conducted to asses linearisation errors due to the first order Taylor series approximation, which is used to linearize the observation equations.
In the case of noise free observations, the differences to the reference model are in the order of about 10^{-13} to 10^{-16}, which is in the order of numerical rounding errors.

7.2.2 White noise

In this scenario, white noise is added to the simulated observations according to Table 7.2. Since the a-priori unit weight factor is set to one and the errors are known, the arc-wise weight matrix has a block-diagonal structure and can be set up using the equivalent values of the added white noise (10 m for positions, 1 μm for ranges).
Using the correct weight matrix, the obtained results should match perfectly to the a-priori chosen reference gravity field.

In Figure 7.2 the degree variances of the reference gravity field JGL165P1 are given in black. The black dashed line corresponds to the formal errors of the reference gravity field. Additionally, the formal errors of the estimated solutions and the differences of both solutions to the reference gravity field are shown. The estimated gravity field models are calculated from the simulated range.
The expression "d/o 165 (165)" stands for the resolution of the analysis and the reference gravity field. The resolution of the reference gravity field is indicated in brackets.

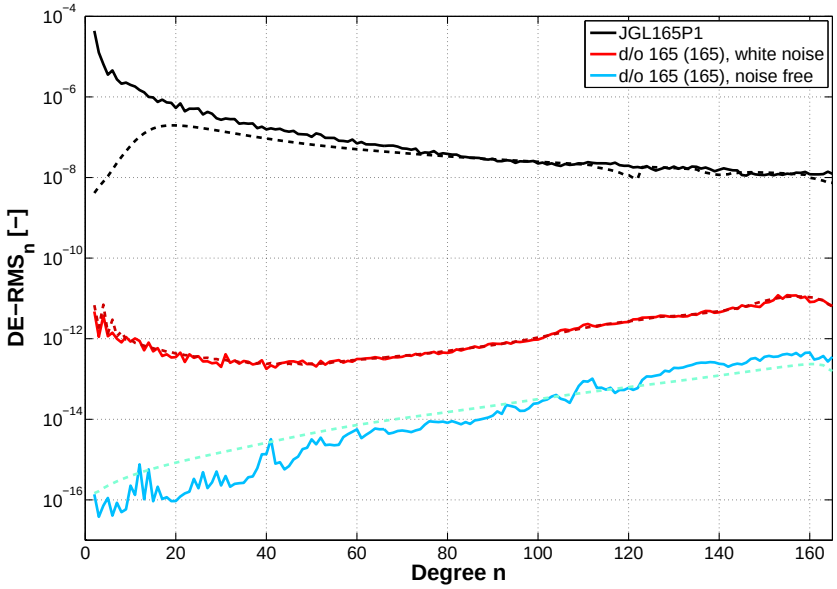

Figure 7.2: DE-RMS$_n$ of closed-loop simulation scenarios - Noise free vs. white noise

In the noise free case, the a-priori reference gravity field JGL165P1 can be estimated with a minimal difference of 10^{-16} per degree. These differences are due to numerical issues, orbit characteristics or errors of numerical integration. Nevertheless, it is the best possible solution.
Adding white noise to the observations, leads to a decreased accuracy of the recovered gravity field solution.
In both cases, the formal errors of the recovered gravity field solution agree with the empirical errors, represented by the differences to the reference gravity field. Furthermore, the a-priori and a-posteriori variance of unit weight are consistent, i.e. the stochastic model can be assumed to be set up correctly. These results lead to the assumption that no model errors exist and that the algorithm is working correctly.

7.2.3 Range versus range rate

A closed-loop simulation scenario with white noise is chosen to compare different types of Ka-band observations (ranges and range rates), where the noise level of the observations is according to Table 7.2. The error degree variances of the estimated spherical harmonic coefficients with respect to the reference gravity field are shown in Figure 7.3. The red curve represents the parameters estimated from ranges and the cyan curve represents the parameters estimated from range rates.

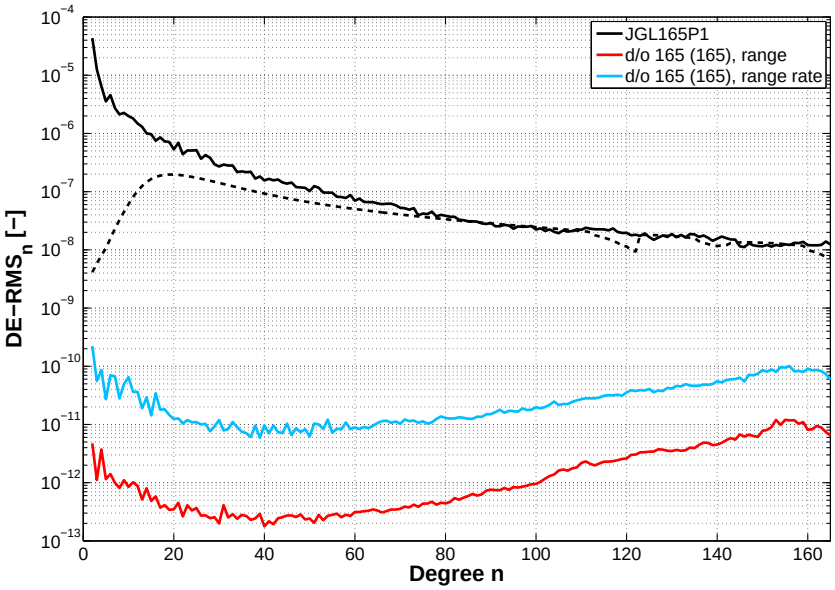

Figure 7.3: DE-RMS$_n$ of the closed-loop simulation scenario - Range vs. range rate

Comparing the two solutions, it should be emphasized, that the offset between the solutions is caused by the incorrect weight factor used for the range rate observations. Since the noise introduced to the range rates is only an assumption and is not gained by numerical differentiation. The ranges are the direct observation from the Ka-band (cf. Section 6.1.2). Therefore, the correct weight factor could be determined by introducing the noise for ranges and generating the noise for the range rates by means of differentiation or error propagation. The noise of the ranges is amplified when the range rates are processed by numerical differentiation.
If the variance-covariance matrix of the observations and consequently the weight matrix is set up correctly, there should occur no differences between the solutions.

The ranges are considered as the direct Ka-band observations, due to that reason the introduced noise corresponds to the weight factor and there is no necessity for an error propagation. Therefore, ranges are used for all further simulation studies.

7.3 Simulation scenario: up to d/o 165, with white noise

The variable input parameters for the analysis include not only the introduced white noise and the type of SST observation used, but also the reference gravity field, the arc length and the weight matrix. In this section the influence of these variable input parameters is examined.

In order to evaluate how sensitive the solution is to different parameters, some additional simulation scenarios have been conducted to analyse, how well the "true" gravity field JGL165P1 can be recovered with evenly distributed noisy orbit and tracking data using:

- different a-priori reference fields,
- different arc lengths (10/30/60/90 minutes) and
- different weighting factors

7.3.1 A-priori reference field

Reference gravity field - JGL165P1

The JGL165P1 lunar gravity field model, which has the highest resolution at present, is used for the synthesis, i.e. the simulation of the orbit and Ka-band observations, up to degree and order (d/o) 165.
For this model several input data sets were used, including the radio tracking of the Lunar Orbiter 1 to 5, Apollo 15 and 16 subsatellites, Clementine, and all the data of the LP spacecraft.

"JGL165P1 model is one of the reliable models among the existing lunar gravity models at least prior to degree 100, which can reveal the character of medium and long wavelength of lunar external gravity field" (Yan et al., 2006, p. 253).

Reference gravity field - Clone

In the case of closed-loop simulations, the a-priori reference field JGL165P1 is used for both the synthesis and analysis. Using real data, the a-priori reference field will show clear differences to the recovered lunar gravity field solution (cf. Section 8.2.2). In contrast to GRAIL, previous missions did not provide a global data set and required regularization methods to enable the recovery of global gravity field models. For these reasons, previous lunar gravity field models can be assumed do not perfectly represent the true signal. Therefore, a Clone of the gravity field model JGL165P1 is used for the analysis instead.
To generate the coefficients of the JGL165P1 Clone the coefficients of the JGL165P1 gravity field model model are deteriorated by their corresponding formal errors. The plus/minus sign of the added formal error is determined according to a random process.

Both reference gravity field models are shown in Figure 7.4. As intended, the DE-RMS$_n$ of the JGL165P1 Clone correspond to the formal errors of the JGL165P1 model.

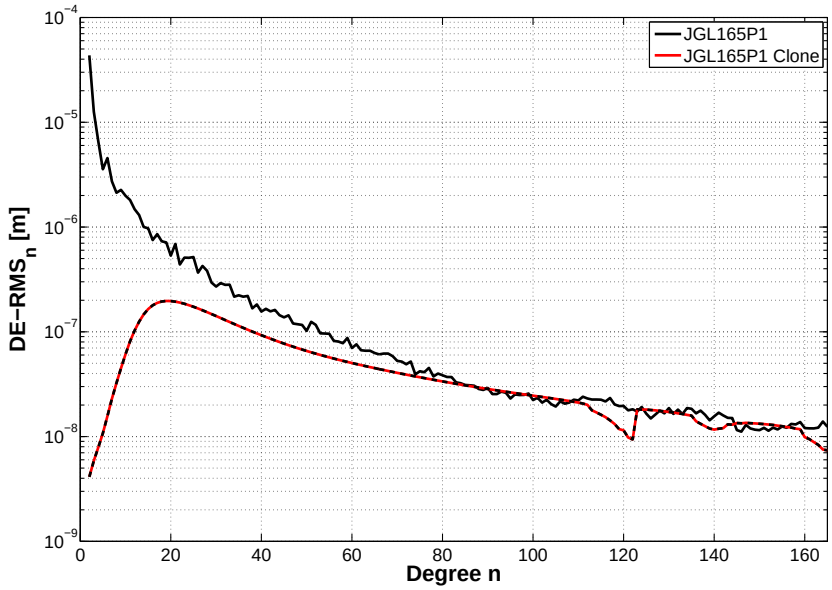

Figure 7.4: DE-RMS$_n$ of the reference gravity field JGL165P1 Clone

Formal versus empirical errors

The analysis up to d/o 165 shows that the solution is influenced by the used a-priori reference gravity field (cf. Figure 7.5). The formal errors of the recovered gravity field solution should agree with the empirical errors, the offset is due to linearisation errors, which in turn are caused by the inaccurate a-priori reference gravity field. If the solution is iterated using the recovered solution as a-priori reference field, the formal errors match the empirical errors (cf. Figure 7.6).

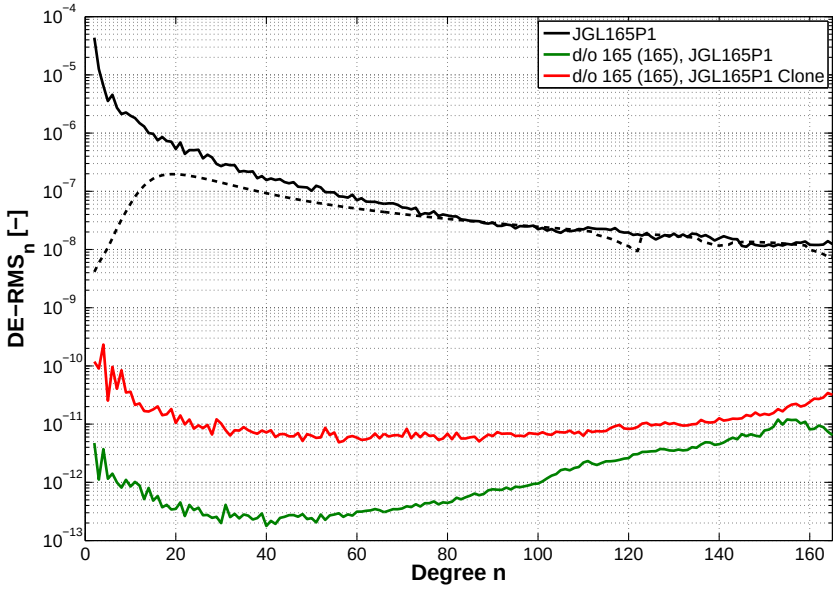

Figure 7.5: DE-RMS$_n$ of the simulation scenario: up to d/o 165, with white noise - JGL165P1 vs. JGL165P1 Clone used as a-priori reference gravity field

All following simulation scenarios use the JGL165P1 Clone as a-priori reference field.

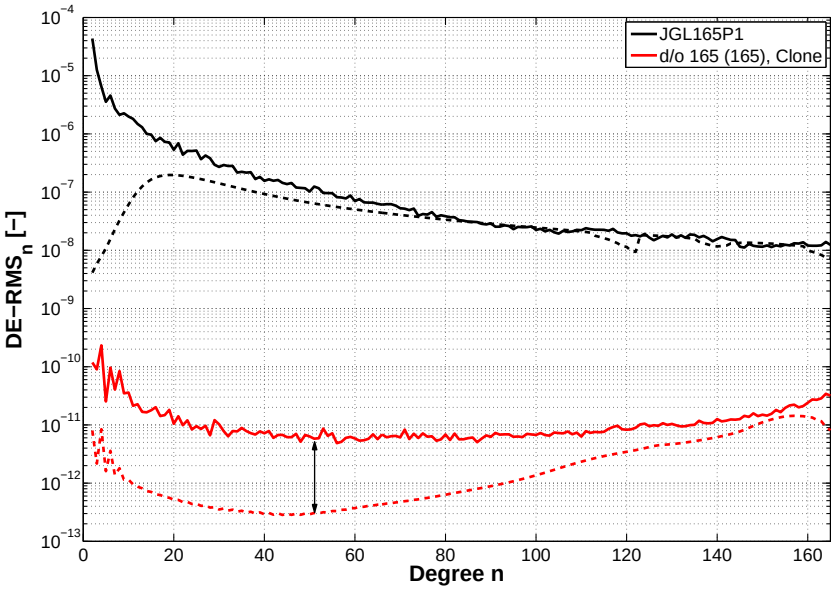

(a) Reference gravity field: JGL165P1 Clone

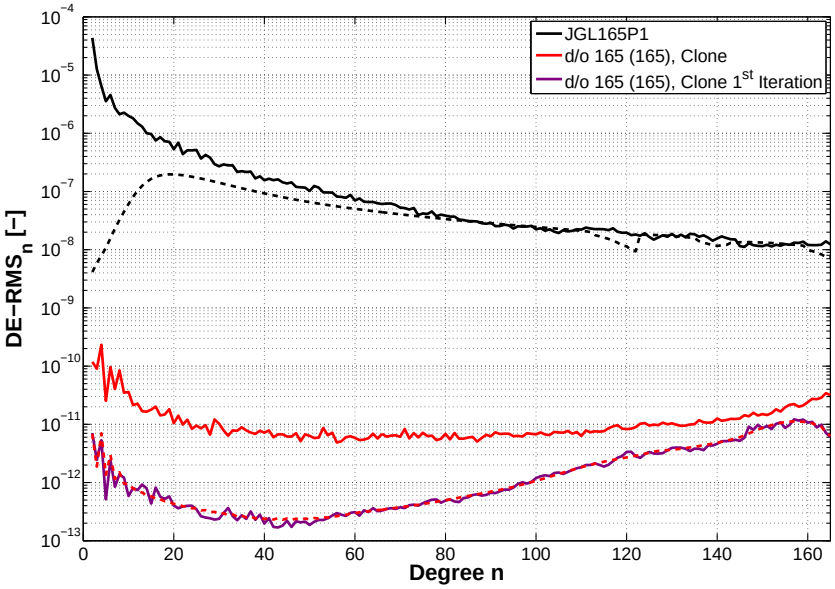

(b) Reference gravity field: JGL165P1 Clone - 1st Iteration

Figure 7.6: DE-RMS$_n$ of the simulation scenario: up to d/o 165, with white noise - Clone

7.3.2 Arc length

The results obtained by the analysis are influenced by the choice of the arc length. Previous results of the satellite mission GRACE showed that a good choice for the arc length is between 1/3 and 1/2 of the satellite revolution time.

If the arc length is chosen too short a large number of arc-related unknowns arise and long wavelengths might be distorted. On the other hand, if the arc length is chosen too long accumulated effects may arise.
Here, short arcs are used, which have the advantage that non-modeled perturbations of the orbit have less influence and the handling of data gaps is easier (cf. Chapter 6).

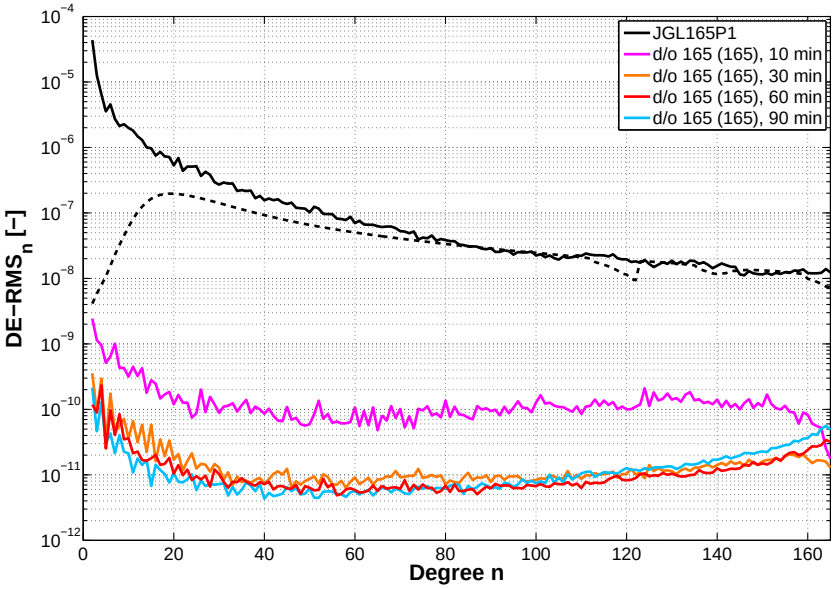

Figure 7.7: DE-RMS$_n$ of the simulation scenario: up to d/o 165, with white noise - Arc length

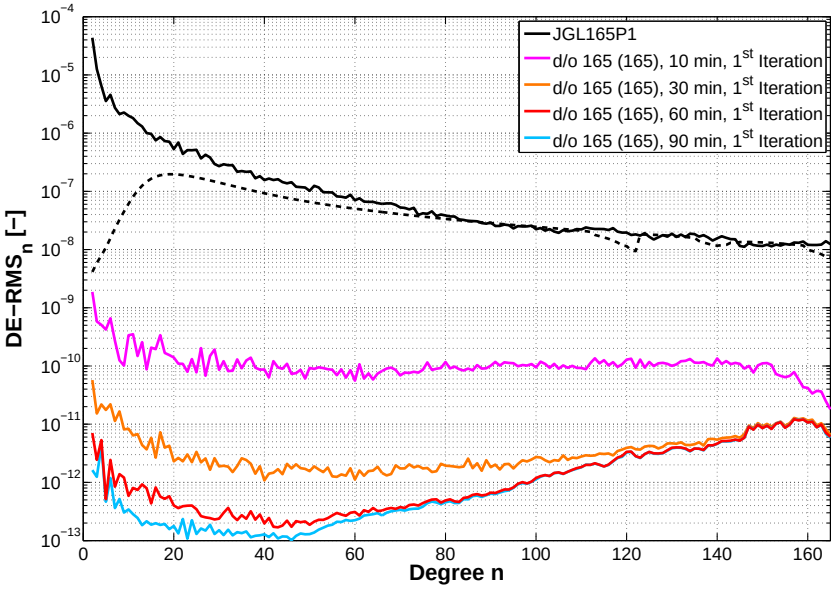

Figure 7.8: DE-RMS$_n$ of the simulation scenario: up to d/o 165, with white noise - Arc length

The effects of different arc lengths are given in Figure 7.7. Here, a simulation scenario up to d/o 165 is used, with the observations containing only white noise. The arc length is varying between 10, 30, 60 and 90 minutes, which corresponds approximately to 1/10, 1/3, 1/2 and 4/5 of the revolution period.
For the sake of completeness, the solutions are iterated once due to the inaccurate a-priori reference gravity field. The results of the 1st iteration using different arc length are given in Figure 7.8.

According to the results, the best arc length for the GRAIL simulation studies is between 60 and 90 minutes.

7.3.3 Stochastic model

For the recovery of the spherical harmonic coefficients it is essential that the relative weighting between the orbit and Ka-band observations is set up correctly (cf. Table 7.2).
If the weight matrix is chosen correctly, the relative weighting between the observations corresponds to 1:10 000 000. The influence of a wrong relative weighting by one or two orders of magnitude is examined, i.e. the position accuracy is changed from 10 m to 1 m, for instance.
The difference between the results are the weight factors that are used for the two observations types. In the following, several results with different weight factors and different noise levels are presented.

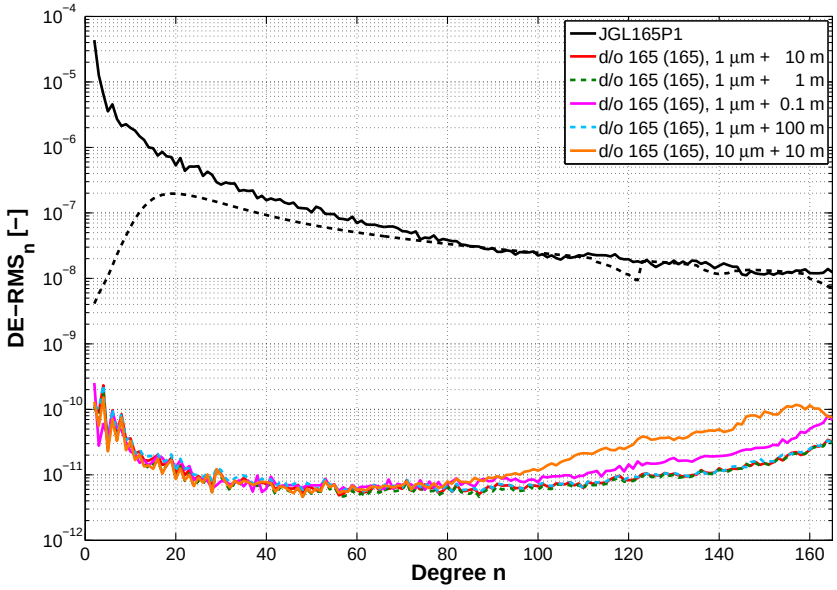

Figure 7.9: DE-RMS$_n$ of the simulation scenario: up to d/o 165, with white noise - Weight factors

In one case, the weight factor for the positions is chosen too optimistic (1 m and 10 cm). The wrong relative weighting leads to an incorrect stochastic model causing differences mainly in the higher degrees (cf. Figure 7.9). If the weight factor of the positions is wrong by one order of magnitude (1 m or 100 m) the differences are very small.
Whereas, in the other case, the weight factor for the ranges is chosen too pessimistic (10 μm) and less emphasis is laid on these data. Hence, the differences to the reference gravity field increase.

The effect from wrong orbit accuracies is relatively small compared to that from wrong Ka-band accuracies. Consequently, the estimation is more sensitive to the Ka-band observations than to the noisy orbit.

7.3.4 Noise level

In a next step, the noise levels of the simulated observations are changed and the weight factors are chosen correctly in accordance with the noise levels. The results are given in Figure 7.10.

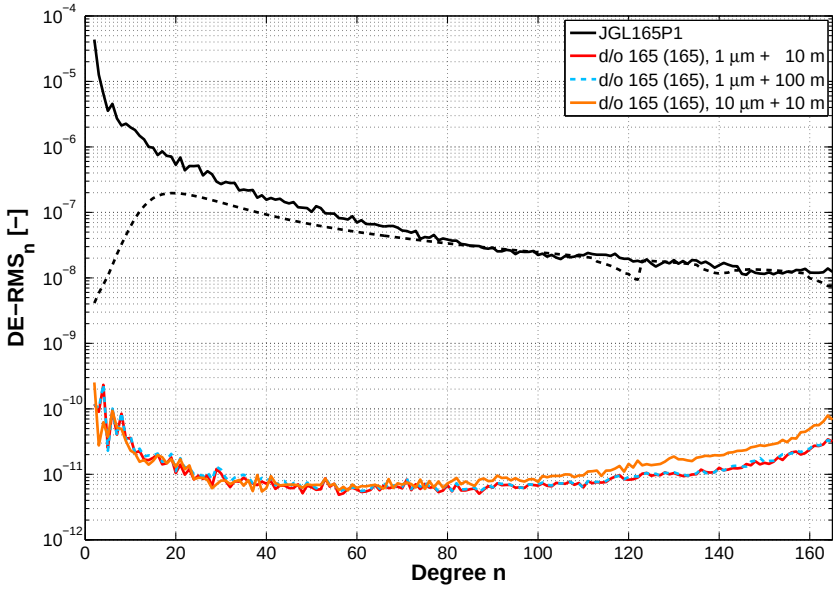

Figure 7.10: DE-RMS$_n$ of the simulation scenario: up to d/o 165, with white noise - Noise levels

Figure 7.10 shows that the relatively low accuracy of the orbit is not the limiting factor. In fact, the system itself is most sensitive to noisy Ka-band observations. Thus, the "bottleneck" of this concept is obviously the accuracy of the Ka-band observations and not the accuracy of the positions.

7.4 Truncated simulation scenario: up to d/o 100, with white noise

Gravity fields derived from real data have infinite resolution. Therefore there will be an omission error due to the unresolved degrees. Besides, the calculation effort increases quadratically with increasing degree and order.

The orbit and Ka-band observations are simulated with the reference gravity field JGL165P1 up to d/o 165, but within the analysis the spherical harmonic coefficients are only resolved up to d/o 100.
The truncation of the spherical harmonic expansion at degree 100 leads to spectral aliasing, which is also denoted as omission error, due to the neglected part of the gravity field. This inconsistency of the simulation scenario is reflected in the DE-RMS$_n$ of the estimated signals.

7.4.1 Arc length & reference field

As shown before (cf. Section 7.3.2), the choice of the arc length influences the error variances of the recovered spherical harmonic coefficients (cf. Figure 7.11).
Here, the influence of the resolution of the a-priori reference field is analyzed. Therefore, the a-priori reference field, used for the analysis, is limited to different degrees and orders. As mentioned before, the resolution of the reference gravity field used for the analysis up to d/o 100 is indicated in brackets, i.e. "d/o 100 (100)" stands for a reference gravity field up to d/o 100.

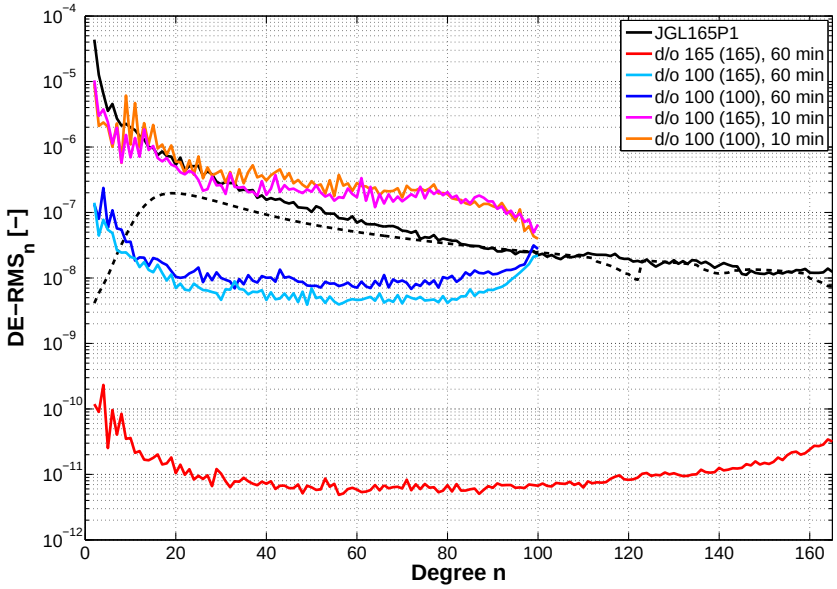

Figure 7.11: DE-RMS$_n$ of the truncated scenario: up to d/o 100, with white noise - Arc length & reference gravity field

As shown in Figure 7.11, the omission error affects the whole spectrum. Comparing different a-priori reference fields, it can be shown that the use of the reference field up to d/o 165 leads to an reduction of the omission error over the whole spectrum.

7.4.2 Reference field & gradient field

If the reference gravity field and gradient field are not truncated, an improved gravity field solution is gained. To asses the influence of the gradient field, several solutions using different degrees of expansion for the gradient field are computed. The contribution of the truncated gradient fields are shown in Figure 7.12. Here, the specifications in brackets stand for the resolution of the gravity field and the gradient field, respectively.
The higher the maximum degree of the gradient field, the better the solution becomes. The influence of the gradient field is probably due to the roughness of the lunar gravity field. The use of a high resolution gravity and gradient field reduces the omission error and noise of the estimated spherical harmonic coefficients.
This shows, that a high-resolution gradient field is important, but also extends the computation time.

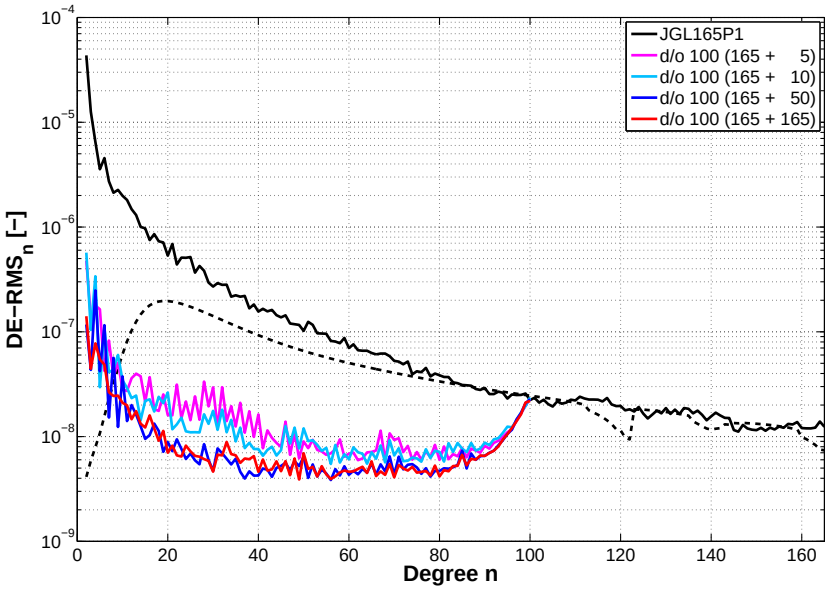

Figure 7.12: DE-RMS$_n$ of the truncated scenario: up to d/o 100, with white noise - Reference gravity field & gradient field

7.5 Estimation of Love numbers

The Moon's response to the gravitational attraction of the Earth and Sun is described by Love numbers (cf. Section 3.4). The strongest influence on the gravitational potential is caused by the second degree tides and can be expressed by the Love number k_2.
If the solid Moon tides are taken into account in the synthesis, i.e. the tidal accelerations are simulated, the values of k_2 and k_3 can be re-estimated in the analysis. The a-priori value of the Love number k_2 is 0.0213, following Goossens and Matsumoto (2008). The a-priori value of the Love number k_3 is set to 0.0073. Since the size and the composition of the lunar core is not clearly determined yet, the lunar Love number can help to improve models of the deep lunar interior.
If the simulated observation data is containing white noise and the JGL165P1 model is used as reference gravity field for the analysis, the estimated values for the Love numbers k_2 and k_3 and their variances are given by:

- $k_2 = 0.02135 \pm 0.000057$
- $k_3 = 0.00735 \pm 0.000397$

7.5.1 Real data analysis

For the real data analysis the lunar Love numbers have not been successfully recovered yet. The non-gravitational accelerations, such as lunar albedo, solar radiation pressure and spacecraft thermal acceleration, are not modeled. Therefore, the lunar Love numbers may be drowned by these non-gravitational accelerations and can not be recovered correctly.
According to (Park et al., 2012) the non-gravitational forces acting on the spacecraft should be represented by models, since they are directly related to the formal uncertainties of the estimated low degree coefficients.

Chapter 8

Results - Real data

The gravity field solution from real data analysis is presented in this chapter. The recovered lunar gravity field solution is compared to the reference gravity field JGL165P1, which has the highest available resolution and accuracy at present.

A gravity field model up to degree and order 200 is estimated, which corresponds to a spatial resolution of about 27 kilometers. Compared to previous models the higher spatial resolution and the improved signal quality reveals many features previously not resolved.

8.1 Analysis parameters

The real data sets have been preprocessed, including the synchronization of the data sets and the outlier detection, according to Chapter 6.

The parameters used for the real data analysis are given in Table 8.1. The orbit and Ka-band observations are subdivided into short-arcs with a length of 60 min. The arc length is chosen according to the results of the simulation studies (cf. Section 7.3.2). The lunar gravity field model JGL165P1 (cf. Section 7.3.1) is used as reference gravity and gradient field up to degree and order 165. Moreover, the tidal accelerations of celestial bodies (Earth, Sun and planets) and the solid Moon tides are modeled.
Since there is no exact information about the accuracies of the orbit and Ka-band observations available, the relative weighting between the observations has to be done empirically. The positions are assumed to have an accuracy of 10 m, whereas the range rates are assumed to have an accuracy of 1 μm/s. The comparably low accurate orbit observations are not a limiting factor to the result, since they are down-weighted compared to the range rates and have therefore less influence (cf. Section 7.3.3).
For the analysis, the whole three month of the GRAIL Science Mission are used, otherwise with one month data the resolution up to d/o 200 would not be possible due to the data coverage.
As observation type range rates are used instead of ranges, since the noise behaviour of the range rates is approximated better by white noise.

Table 8.1: Analysis parameters

Gravitational parameter GM	$0.4902801056 \cdot 10^{13}$ $\mathrm{m^3\,s^{-2}}$
Lunar radius R	1 738 000 m
Reference field	JGL165P1 (up to d/o 165)
Ephemeris file	JPL DE405 and JPL DE421
Sampling	5 s
Period	3 month (01-Mar-2012 to 29-May-2012)
Ka-band observation type	range rates
Arc Length	60 min
Position $\sigma_{\mathbf{r}}$	10 m
Range rate $\sigma_{\dot{\rho}}$	1 μm
Max. degree n	200

8.2 Results

8.2.1 Iterations

In a first step, a gravity field solution up to d/o 200 is recovered from the preprocessed 3 month of real data with the JGL165P1 used as reference gravity field. As the data still contains outliers, stripes are visible in the derived selenoid heights (not shown here). Therefore, the solution has to be iterated using VCE (cf. Section 5.4). Here, the recovered gravity field solution serves as input (= approximate solution) for the next iteration step. Within the VCE arcs containing outliers are down-weighted appropriately.

Figure 8.1 shows the recovered spherical harmonic coefficients, as well as the corresponding formal errors in comparison to the reference gravity field JGL165P1. After several iterations, the signal follows rather the empirical power law than before. Moreover, the stripes vanish, since the arcs containing the outliers are down-weighted and have less influence on the estimated solution (not shown here).

Since the less accurate ephemeris file DE405 is used instead of DE421 (cf. Appendix A.3), the analysis is repeated using the DE421 ephemeris file. The iterated gravity field solution serves as a-priori reference gravity field for the analysis. The solution of the 2^{nd} iteration is given in cyan and the improved solution is given in red. Additionally, the scaled Kaula rule for the Moon $2.5 \cdot 10^{-4} n^{-2}$ is given in grey (cf. Figure 8.2).

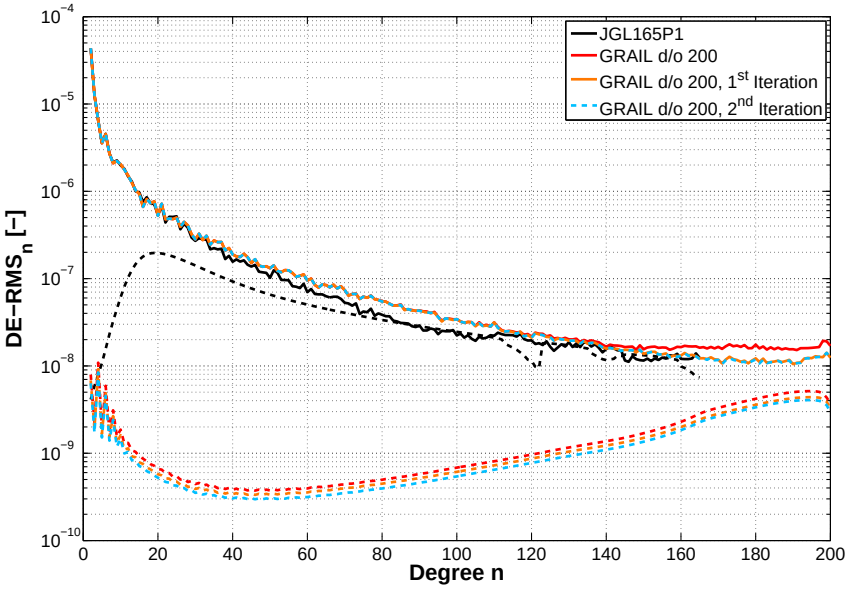

Figure 8.1: Recovered gravity field solution - Iterations

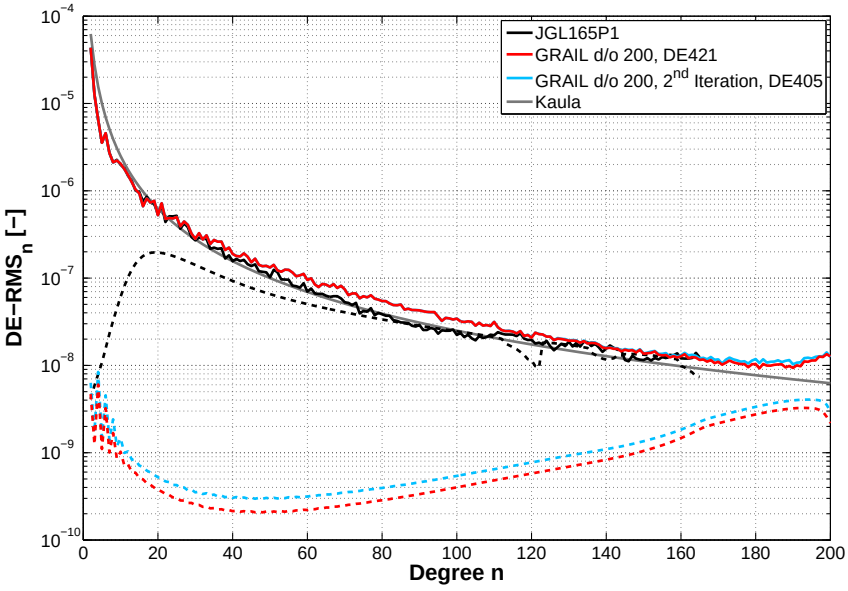

Figure 8.2: Recovered gravity field solution - DE421

8.2.2 Comparison to JGL165P1

Degree variances - DE-RMS$_n$

Finally, the recovered gravity field solution, denoted as GRAIL d/o 200, is compared to the gravity field solution JGL165P1. Therefore, the RMS of the degree-wise error variances in selenoid heights is computed and presented in Figure 8.3.

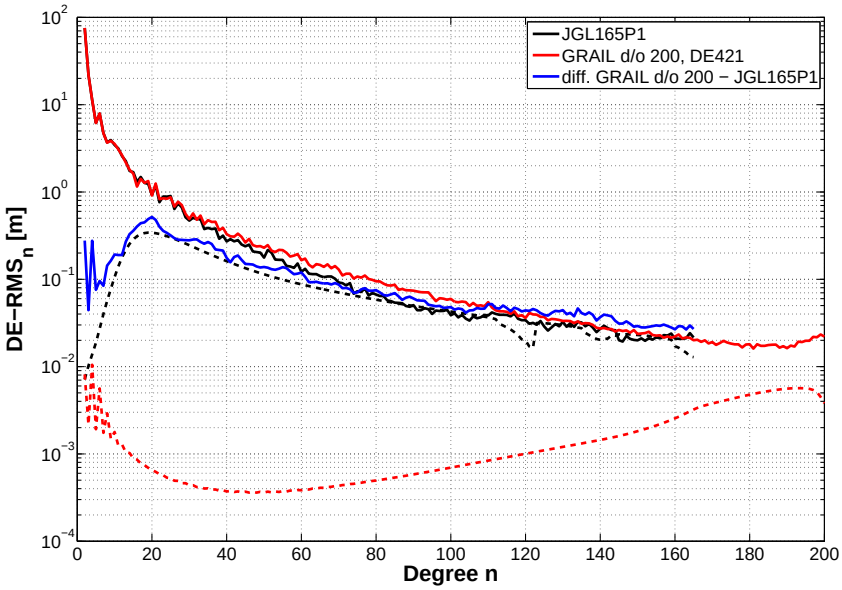

Figure 8.3: DE-RMS$_n$ of the recovered gravity field solution - GRAIL d/o 200

The error variances follow more or less the formal errors of the gravity field model JGL165P1. Since the formal errors of the recovered solution do not intersect the signal curve, the maximum potential has not been achieved yet.
Compared to the JGL165P1 model, GRAIL improves the gravity field solution by up to two orders of magnitude. Hence, the GRAIL mission provides the best lunar gravity field up to date.

Moreover, the solution can be compared to the lunar gravity field recovered from the GRAIL mission by the NASA. Unfortunately, the gravity field solutions from Zuber et al. (2013) and Konopliv et al. (2013) are not available yet, as they have not been published officially. With the availability of the NASA lunar gravity field, the solution can be validated externally.
In general, the signal curves seem to match quite good, as far as this can be said from the published figures (cf. Zuber et al., 2013; Konopliv et al., 2013, p. 669 and p. 57, respectively).

Spherical harmonic coefficients

The spherical harmonic coefficients of the recovered solution in Figure 8.4 show that the largest uncertainties occur in the sectoral coefficients. This phenomenon can be explained from the orbit design of the two twin satellites: the satellites orbit the Moon behind each other in near polar orbits. Consequently, the best coverage is achieved for the zonal areas as the Moon rotates. This may also lead to a North-South striping pattern.

Tthe spherical harmonic coefficients of the JGL165P1 show that the analysis was done stepwise.

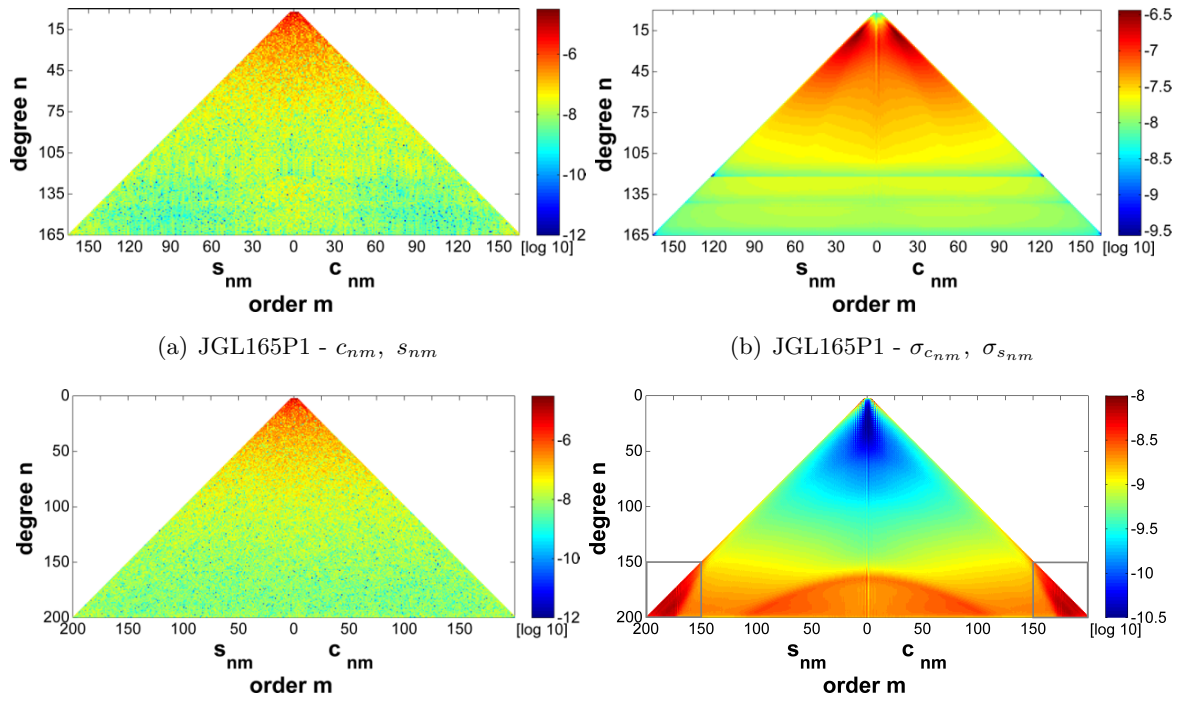

(a) JGL165P1 - $c_{nm},\ s_{nm}$

(b) JGL165P1 - $\sigma_{c_{nm}},\ \sigma_{s_{nm}}$

(c) GRAIL d/o 200 - $c_{nm},\ s_{nm}$

(d) GRAIL d/o 200 - $\sigma_{c_{nm}},\ \sigma_{s_{nm}}$

Figure 8.4: Spherical harmonic coefficients - JGL165P1 vs. GRAIL d/o 200

Figure 8.5 shows the GRAIL-A groundtrack during the 3 month PM with a sampling of 5 seconds for a limited area of 6° x 6°. The projection is a Robinson projection centered around 270° eastern longitude.

As already mentioned, the recovered gravity field solution is resolved up to d/o 200, which corresponds to a spatial resolution of 27 kilometers. Along the equator 1° corresponds to 30 kilometers on the lunar surface. Due to the limited horizontal coverage, the formal errors of the sectoral coefficients increase with increasing degree and order, starting from d/o 180 onwards. This characteristic behaviour is highlighted by the grey boxes in Figure 8.4.

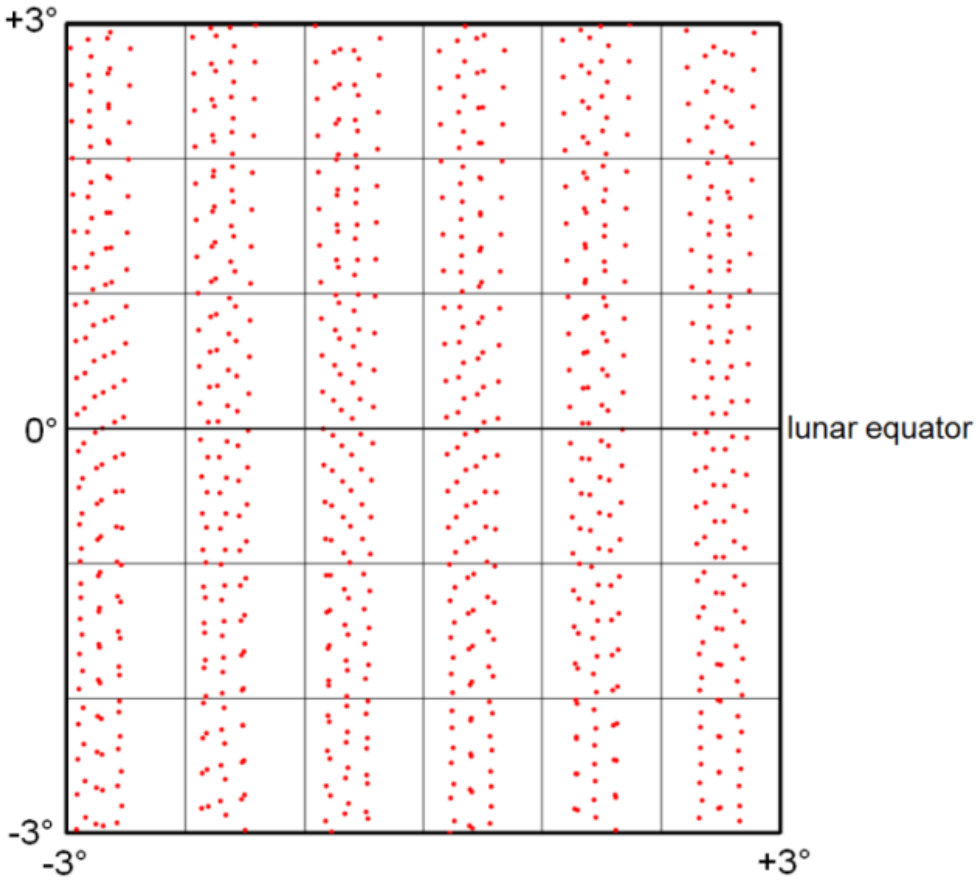

Figure 8.5: GRAIL groundtrack during PM for a limited area of 6° x 6°

Selenoid heights

Figure 8.6 shows the selenoid heights from JGL165P1 and from the reconstructed gravity field solution GRAIL d/o 200. The projection is a Mollweide projection centered around 270° eastern longitude, leaving the nearside on the right and the farside on the left of the figure. A grid of 0.5° is used. The reference field consists of the central term of the selenopotential and has been subtracted.

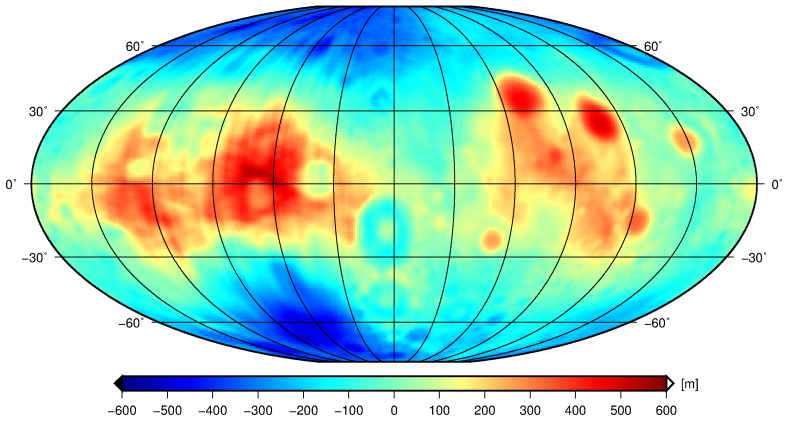

(a) JGL165P1

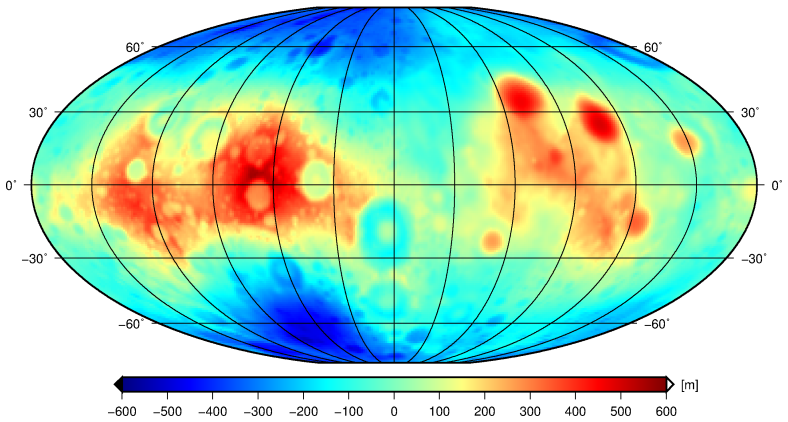

(b) GRAIL d/o 200

Figure 8.6: Selenoid heights from JGL165P1 and GRAIL d/o 200

Evidently, the availability of global ll-SST observations improves the spatial resolution of the lunar nearside and farside compared to the reference gravity field model JGL165P1 (cf. Figure 8.7). Compared to JGL165P1, the model displays features previously not resolved, as well as more pronounced high-frequency variations. Both of these facts are attributed to the improved high-resolution gravity field model.

The largest differences between both models can be found on the lunar farside. However, there also occur smaller differences on the nearside, revealing some North-South striping pattern. To show more details, the colorbars in Figure 8.7 do not cover the full range of differences.

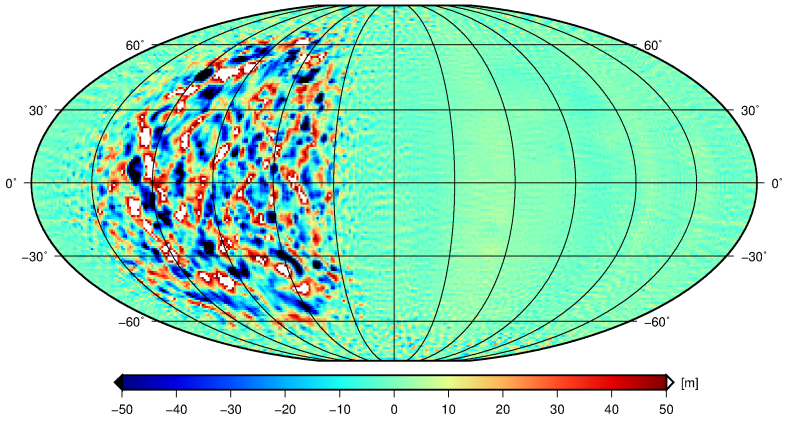

(a)

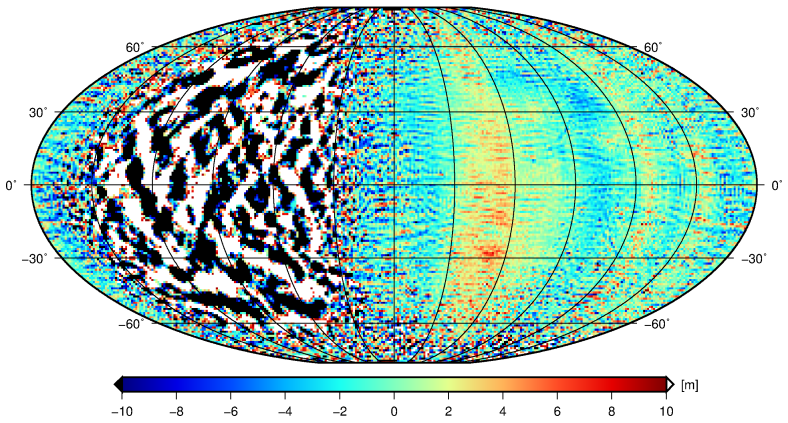

(b)

Figure 8.7: Differences in selenoid heights: GRAIL d/o 200 - JGL165P1

Free-air anomalies

According to the Meissl-Scheme (cf. Figure 3.2, p. 17), the free-air anomalies show the high-frequent part of the gravity field. Hence, more detailed short-wavelength structures on the lunar surface become visible.
Figure 8.8 shows the free-air anomalies from JGL165P1 and from the reconstructed gravity field solution GRAIL d/o 200. The projection is a Mollweide projection centered around 270° eastern longitude, leaving the nearside on the right and the farside on the left of the figure. A grid of 0.5° is used. The reference field consists of the central term of the selenopotential and has been subtracted.

By comparing lunar basins and mascons with the gravitational signature, a strong correlation between the lunar gravity field and the topography is revealed (cf. Appendix A.2).

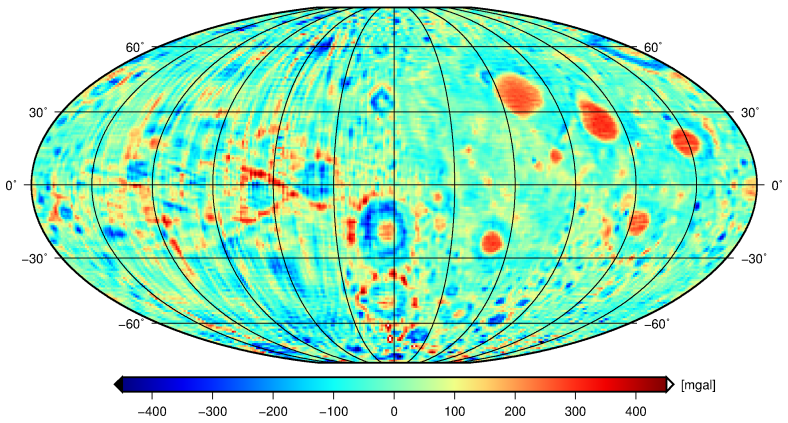

(a) JGL165P1

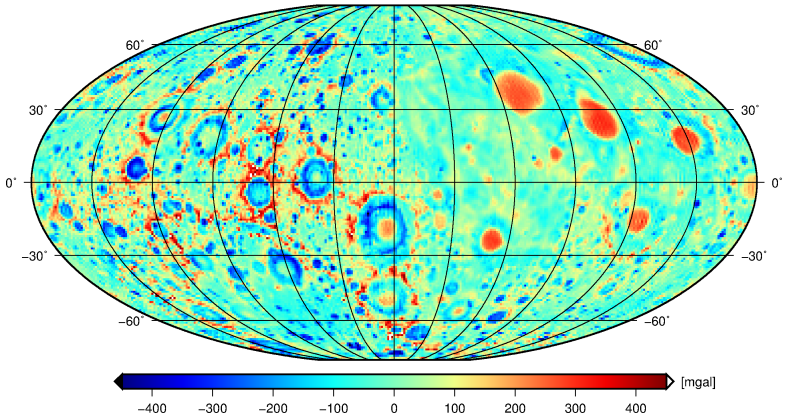

(b) GRAIL d/o 200

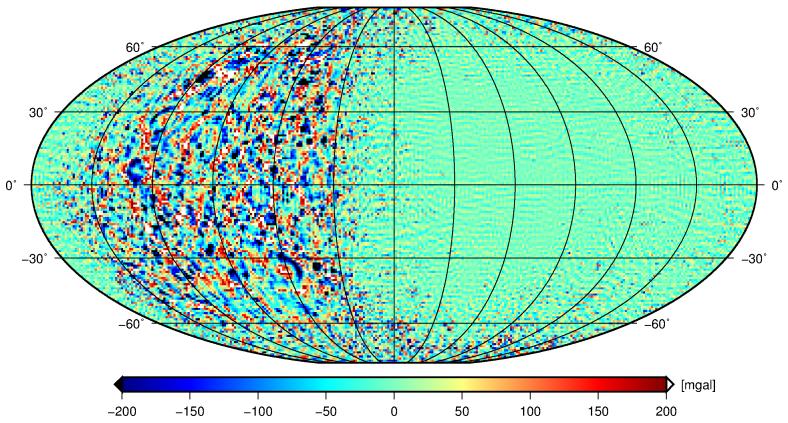

(c) Differences

Figure 8.8: Free-air anomalies from JGL165P1 and GRAIL d/o 200

8.3 Validation

To validate the achieved results, the recovered gravity field solution is used to simulate ll-SST observations for the GRAIL PM. Therefore, the orbits of GRAIL-A and GRAIL-B are simulated with the initial state vectors from the real data using the GRAIL d/o 200 model as reference gravity field. In a next step, the simulated orbits are used to simulate the ll-SST observations (according to Section 4). The differences between the simulated range rates based on the recovered gravity field model and the real data are given by the residuals.
In addition, ll-SST observations are also simulated from the reference gravity field model JGL165P1. For both models the obtained residuals to the real data are compared to validate the solution.

Figure 8.9 shows the residuals of the simulated range rates of both models (JGL165P1 and GRAIL d/o 200) with respect to the real data over a period of 5 days. Comparing both models, the recovered gravity field model clearly improves the simulated ll-SST observations and therefore reduces the residuals.

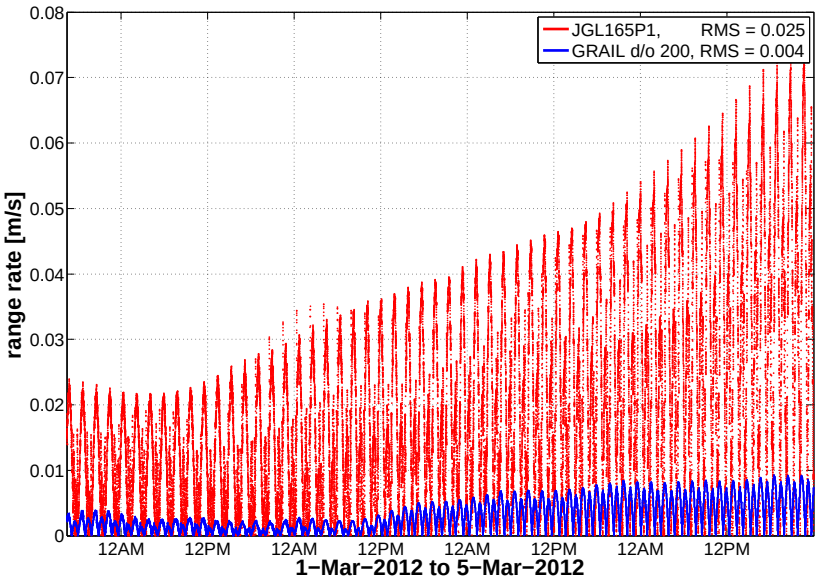

Figure 8.9: Range rate residuals - JGL165P1 vs. GRAIL d/o 200

Chapter 9

Conclusions & outlook

9.1 Conclusions

The prime objective of this work was to recover a global lunar gravity field from GRAIL real data. To achieve this objective it is previously necessary to asses the performance of GRAIL by means of various sensitivity studies.
In a first step, the synthesis, the orbit and Ka-band observations have to be simulated. In a second step, the analysis, the mathematical model of the integral equation approach is set up and the spherical harmonic coefficients, representing the lunar gravity field, are estimated.

The following conclusions can be drawn from the simulation studies and the real data analysis.

Compared to other approaches, the integral equation approach avoids combining the highly accurate Ka-band observations with the comparably low accurate orbit. The only drawback is the associated high computational effort.
The relative weight between the observations has a significant influence on the result. Although the GRAIL mission has relatively low accurate orbits, the result is not limited significantly to the accuracies of the orbit, but is limited to the accuracy of the more influential Ka-band observations. Nevertheless, an improvement of the orbit determination, especially for the farside, would be preferable.

As shown in Chapter 8, the recovered gravity field model solution from GRAIL real data is very promising. Compared to previous missions, GRAIL realized for the first time the ll-SST principle for an artificial satellite orbiting the Moon. The availability of global inter-satellite tracking data improves the spatial and spectral resolution on the lunar nearside and farside compared to previous lunar gravity field models. The GRAIL PM, for which results are presented here, dramatically improves the gravity field solution by up to two orders of magnitude. The estimated model extends to degree and order 200, corresponding to a spatial resolution of about 27 kilometers on the lunar surface. Hence, the GRAIL mission provides the best lunar gravity field up to date.

Importantly, the GRAIL mission enables the estimation of a global high-resolution gravity field model without any regularization.
This is a significant advantage compared to previous models, since the introduction of a-priori information to the solution can be avoided. It also means that there is no need for a regularization parameter, which greatly affects the solution.

9.2 Outlook

The work presented in this thesis has shown that the recovery of the lunar gravity field from GRAIL real data using the integral equation approach is capable of extracting a global high-resolution gravity field model of the Moon, which contains the high-frequency gravity field signal for the first time.
Due to the computational effort the estimation is limited to degree and order 200. Since the formal errors do not intersect the signal curve, the solution could be still improved by estimating up to a higher resolution.

Furthermore, the solution could be refined from a mathematical point of view. The stochastic model could be improved by not assuming white noise and introducing more realistic weight factors for the observations instead.

To improve the solution, the times of maneuvers (Angular Momentum Dumps (AMDs)), which have a typical duration of 1-2 minutes, should be considered when defining the time boundaries of the short arcs. Otherwise, unmodeled accelerations from the AMDs may corrupt the gravity field solution (Konopliv et al., 2013).

In future, additional 3 month of data from the extended mission phase with even lower orbit altitudes will be available and should be used for the real data analysis as well.

Open issues include the setup of a validation scheme and the modeling of non-gravitational accelerations such as solar radiation pressure and lunar albedo. These accelerations should be taken into account, since an accurate modeling of the non-gravitational forces acting on the spacecraft is necessary for an improvement of the solution.
Up to now, the real data analysis does not include orbit determination and the GRAIL orbits provided by NASA's PDS are used. Consequently, orbit determination can be considered as an open issue too.

List of abbreviations

AMDs	Angular Momentum Dumps
CCAF	Cape Canaveral Air Force Station
CDR	Calibrated Data Record
CoM	Center of Mass
CRS	Celestial Reference System
DLR	German Aerospace Center
d/o	degree and order
DOWR	Dual One Way Range
DSN	Deep Space Network
DT	Dynamical Time
EM	Extended Mission
EME2000	Earth-Centered Earth Mean Equator and Equinox of Epoch J2000
E/PO	Education and Public Outreach
ET	Ephemeris Time
GNSS	Global Navigation Satellite System
GPS	Global Positioning System
GRACE	Gravity Recovery And Climate Experiment
GRAIL	Gravity Recovery and Interior Laboratory
GROOPS	Gravity Recovery Object Oriented Programming System
hl-SST	High-Low Satellite-to-Satellite Tracking
ICRS	International Celestial Reference System
JD	Julian Date
JPL	Jet Propulsion Laboratory
LGRS	Lunar Gravity Ranging System

ll-SST Low-Low Satellite-to-Satellite Tracking
LOI Lunar Orbit Insertion
LOS Line-Of-Sight
LP Lunar Prospector
LRO Lunar Reconnaissance Orbiter
LSA Least Squares Adjustment

MJD Modified Julian Date
MoonKAM Moon Knowledge Aquired by Middle school students
MRO Mars Reconnaissance Orbiter

NASA National Aeronautics and Space Administration

ORP Orbit Period Reduction

PDS Planetary Data System
PM Primary Mission

RMS Root Mean Square
RSB Radio Science Beacon

SDS Science Data System
SELENE Selenological and Engineering Explorer

TAI Atomic Time
TDB Barycentric Dynamic Time
TDT Terrestrial Dynamic Time
TGP Tide Generating Potential
TLC Trans-Lunar Cruise
TSF Transition to Science Formation
TT Terrestrial Time
TTS Time Transfer System

USO Ultra-Stable Oscillator

Appendix A

The Moon

A.1 Bulk parameters - Moon/Earth comparison

The bulk parameters of the Moon and the Earth and the orbital parameters (for the orbit about the Earth) are given in Table A.1.
The orbit of the Moon changes over the course of the year so the distance from the Moon to Earth roughly ranges from 357 000 km to 407 000 km.

Table A.1: Bulk & orbital parameters of the Moon
Source: http://nssdc.gsfc.nasa.gov/planetary/factsheet/moonfact.html

	Bulk parameters	
	Moon	Earth
Mass	0.07349 10^{24} kg	5.9736 10^{24} kg
Equatorial radius	1738.1 km	6378.1 km
Polar radius	1736.0 km	6356.8 km
Ellipticity (Flattening)	0.0012	0.0034
Mean density	3350 kg/m^3	5515 kg/m^3
Surface gravity	1.62 m/s^2	9.80 m/s^2
GM	0.0049 10^6 km^3/s^2	0.3986 10^6 km^3/s^2
J2	202.7 10^{-6}	1082.63 10^{-6}
	Orbital parameters	
	Moon	
Semimajor axis	0.3844 10^6 km	
Mean perigee	0.3633 10^6 km	
Mean apogee	0.4055 10^6 km	
Revolution period	27.3217 days	
Mean orbital velocity	1.023 km/s	
Inclination to ecliptic	5.145°	
Inclination to equator	18.28° – 28.58°	
Orbit eccentricity	0.0549	
Sidereal rotation period	655.728 hrs	
Recession rate from Earth	3.8 cm/yr	

A.2 Selenography

The topography of the Moon, which is also denoted as selenography, from the SELENE laser altimeter is given in Figure A.1. The projections is a cylindrical projection centered around 0° longitude.

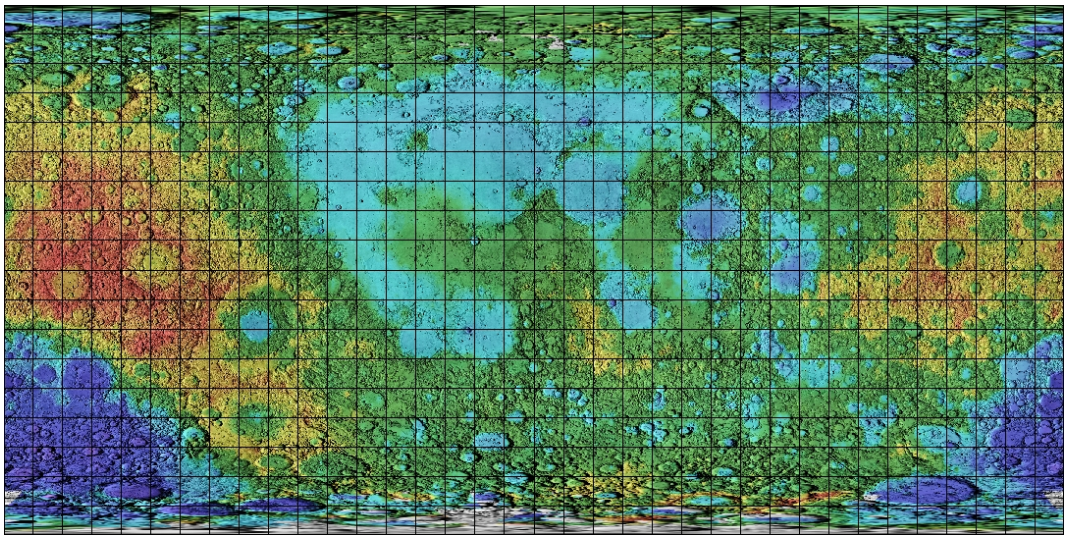

Figure A.1: Topographic map of the Moon from the Kaguya (SELENE) laser altimeter (online available at http://www.mapaplanet.org/explorer/help/data_ set.html# moon_ kaguya_ lalt

A.2.1 Major basins

The locations of the major lunar basins are given in Figure A.2. The nearside is on the right side of the figure and the farside on the left. Lightly shaded or hatched areas indicate basins, whereas shaded areas indicate principal mascons. Unclassified areas are marked by dashed lines.

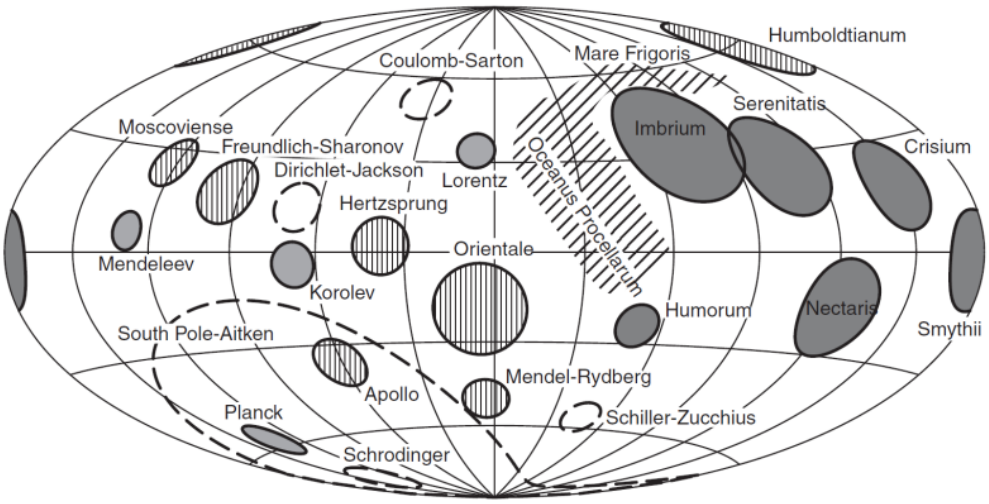

Figure A.2: Locations of the major lunar basins (Source: Namiki et al. (2009, p. 902))

A.3 Lunar librations - JPL DE421

The lunar libration angles calculated from the JPL DE421 ephemeris file are given in Figure A.3. Since the DE421 ephemeris are considered the best available lunar ephemeris at present, the differences to the previous ephemeris DE405 are given in Figure A.4.

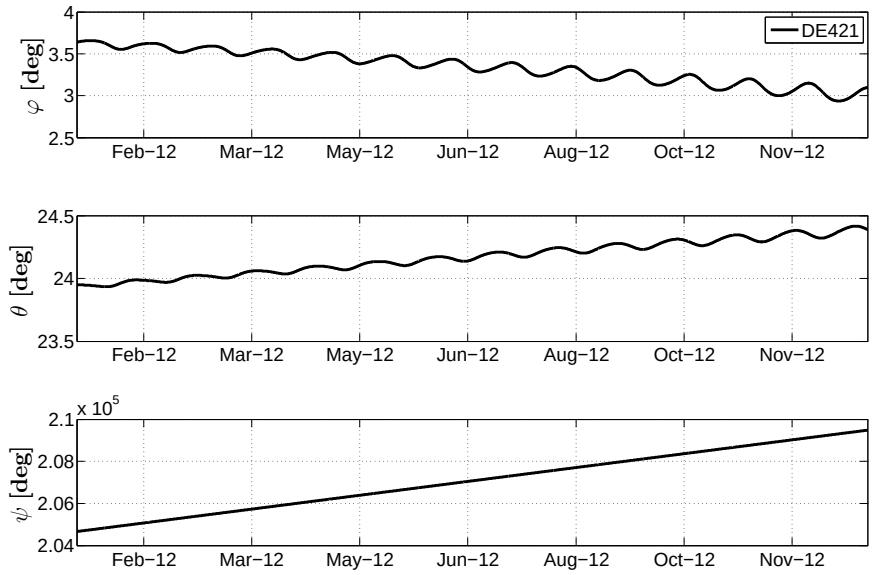

Figure A.3: JPL DE421: Lunar libration angles for a period of one year (01-Jan-2012 to 01-Jan-2013)

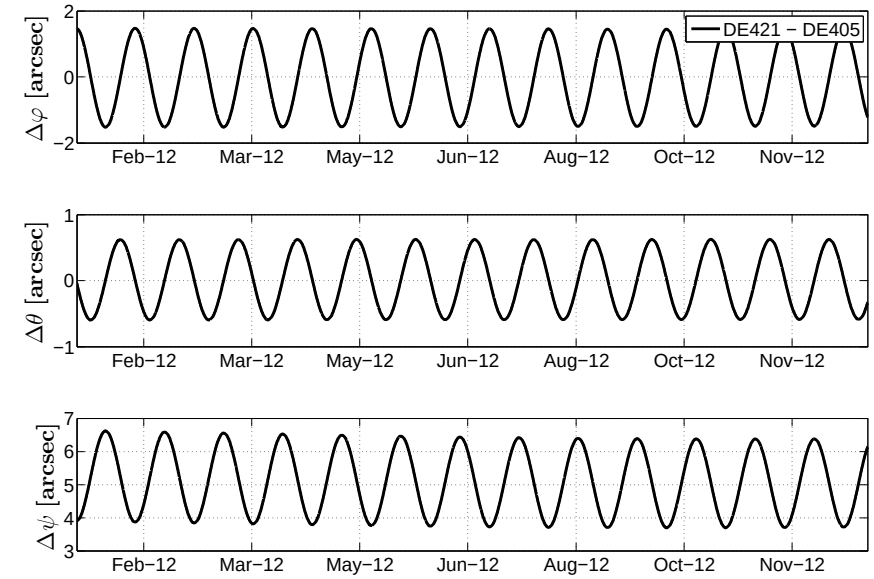

Figure A.4: JPL DE421 vs. JPL DE405: Differences in lunar libration angles for a period of one year (01-Jan-2012 to 01-Jan-2013)

Appendix B

Keplerian elements $\Leftrightarrow$ state vector

In total a set of six independent parameters is needed to describe the motion of a satellite if a unperturbed satellite orbit is assumed. This parameters can be either given as Keplerian elements or as state vector. The transformations between those two representations are given in the following sections.

B.1 Keplerian elements $\rightarrow$ state vector

The six Keplerian elements (cf. Figure B.1) are

- **Semi-major axis** a
- **Eccentricity** e
- **Inclination** i: angle of intersection between the orbital and equatorial plane
- **Right ascension of the ascending node** Ω: angle between the vernal equinox and the direction of the ascending node
- **Argument of perigee** ω: angle between the direction of the ascending node and the direction of the perigee
- **True anomaly** ν or **mean anomaly** M or **eccentric anomaly** E

The first two orbital elements a and e define the form of the orbit, the next three elements i, Ω and ω describe the orientation of the orbit in space and finally the last element ν or M or E defines the position of the satellite along the orbit.
From these elements the position vector $\mathbf{r}$ and the velocity vector $\dot{\mathbf{r}}$ can be calculated uniquely. Vice versa there is one set of Keplerian elements that corresponds to an initial state vector $\mathbf{y}$ with initial values for the position and velocity (cf. Section B.2).

The position vector $\mathbf{r}$ and the velocity vector $\dot{\mathbf{r}}$ in a body-fixed frame can be expressed by

$$\mathbf{r} = a\ (\cos E - e)\ \mathbf{P} + a\ \sqrt{1-e^2}\ \sin E\ \mathbf{Q}, \tag{B.1}$$

$$\dot{\mathbf{r}} = \frac{\sqrt{GMa}}{r}\ (-\sin E\ \mathbf{P} + \sqrt{1-e^2}\ \cos E\ \mathbf{Q}), \tag{B.2}$$

with the unit vector **P** pointing towards the perigee and the perpendicular unit vector **Q** corresponding to a true anomaly $\nu = 90°$.

$$\mathbf{P} = \begin{pmatrix} +\cos\omega\ \cos\Omega - \sin\omega\ \cos i\ \sin\Omega \\ +\cos\omega\ \sin\Omega + \sin\omega\ \cos i\ \cos\Omega \\ +\sin\omega\ \sin i \end{pmatrix} \tag{B.3}$$

$$\mathbf{Q} = \begin{pmatrix} -\sin\omega\ \cos\Omega - \cos\omega\ \cos i\ \sin\Omega \\ -\sin\omega\ \sin\Omega + \cos\omega\ \cos i\ \cos\Omega \\ +\cos\omega\ \sin i \end{pmatrix} \tag{B.4}$$

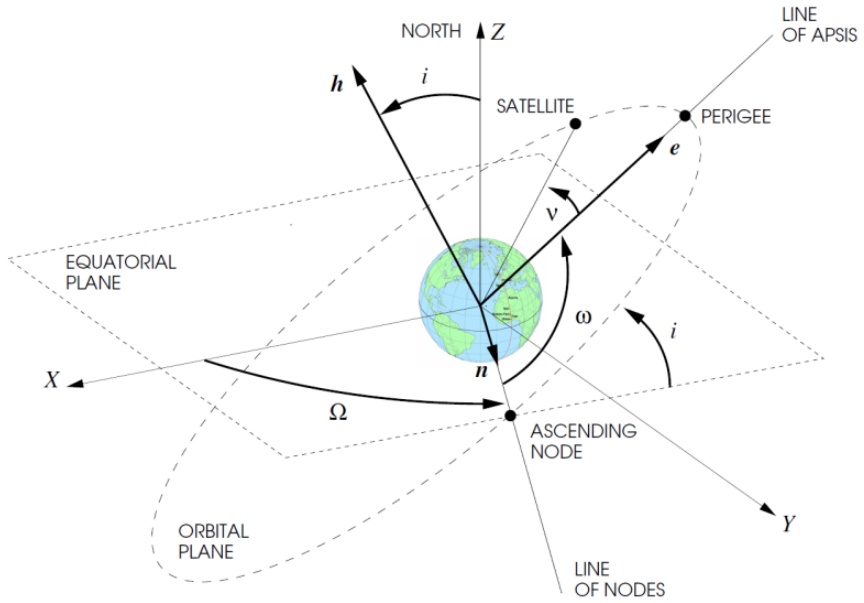

Figure B.1: Keplerian elements w.r.t the Earth (Source: Casella and Lovera (2008, p. 1043))

B.2 State vector → Keplerian elements

The initial values of the position and velocity (in a body-fixed frame) are given by

$$\mathbf{r} = \{x, y, z\}^T, \tag{B.5}$$

$$\dot{\mathbf{r}} = \{\dot{x}, \dot{y}, \dot{z}\}^T. \tag{B.6}$$

First, the areal velocity vector can be calculated

$$\mathbf{h} = \mathbf{r} \times \dot{\mathbf{r}} = \{h_1, h_2, h_3\}^T, \tag{B.7}$$

with its norm $h = \mid \mathbf{h} \mid$

With equation (B.7) the inclination i and the right ascension of the ascending node Ω are obtained by

$$i = \arctan\left(\frac{\sqrt{h_1^2 + h_2^2}}{h_3}\right), \tag{B.8}$$

$$\Omega = \arctan\left(\frac{h_1}{-h_2}\right). \tag{B.9}$$

The semi-major axis a and the eccentricity e are given by

$$a = \left(\frac{2}{r} - \frac{v^2}{GM}\right)^{-1}, \tag{B.10}$$

$$e = \sqrt{1 - \frac{h^2}{GM\ a}}, \tag{B.11}$$

with $r = \mid \mathbf{r} \mid$ and $v = \mid \dot{\mathbf{r}} \mid$. GM corresponds to the gravitational parameter.

The true anomaly ν can be calculated trough

$$\nu = \arctan\left(\frac{a(1-e^2)\ \mathbf{r} \cdot \dot{\mathbf{r}}}{h[a(1-e^2) - r]}\right). \tag{B.12}$$

With equation (B.12) the eccentric anomaly E can be determined

$$E = \arctan\left(\frac{\sqrt{1-e^2}\ \sin\nu}{\cos\nu + e}\right). \tag{B.13}$$

The eccentric anomaly E can be used to obtain the mean anomaly M

$$M = E - e\ \sin E. \tag{B.14}$$

In order to determine the argument of the perigee ω the argument of latitude u has to be determined first

$$u = \arctan\left(\frac{z/\sin i}{x\ \cos\Omega + y\ \sin\Omega}\right), \tag{B.15}$$

this finally yields

$$\omega = u - \nu. \tag{B.16}$$

List of Figures

List of Tables

Bibliography

E. L. Akim. Determination of the gravitational field of the Moon from the motion of the artificial lunar satellite 'Luna 10'. *Doklady Akdademii Nauk SSSR*, 170:799–802, 1966. originally Russian, English translation in Soviet Physics – Doklady, Vol. 11, No. 10, 1967.

B. A. Archinal, M. F. A'Hearn, E. Bowell, A. Conrad, G. J. Consolmagno, R. Courtin, T. Fukushima, D. Hestroffer, J. L. Hilton, G. A. Krasinsky, G. Neumann, J. Oberst, P. K. Seidelmann, P. Stooke, D. J. Tholen, P. C. Thomas, and I. P. Williams. Report of the IAU Working Group on Cartographic Coordinates and Rotational Elements: 2009. *Celestial Mechanics and Dynamical Astronomy*, 109:101–135, 2011.

S. W. Asmar, A. S. Konopliv, M. M. Watkins, J. G. Williams, R. S. Park, G. Kruizinga, M. Paik, D. N. Yuan, E. Fahnenstock, D. Strekalov, N. Harvey, W. Lu, D. Kahan, K. Oudrhiri, D. E. Smith, and M. T. Zuber. The Scientific Measurement System of the Gravity Recovery and Interior Laboratory (GRAIL) Mission. *Space Science Reviews*, 2013.

F. Casella and M. Lovera. High-accuracy simulation of orbital dynamics: An object-oriented approach. *Simulation Modelling Practice and Theory*, 16(8):1040–1054, 2008.

R. Floberghagen. *Lunar Gravimetry - Revealing the Far-Side*. Kluwer Academic Publishers, Dordrecht, The Netherlands, 2002.

W. M. Folkner, J. G. Williams, and D. H. Boggs. The Planetary and Lunar Ephemeris DE 421. *The Interplanetary Network Progress Report*, 42-178:1–34, 2009a. available online at `http://ipnpr.jpl.nasa.gov/progress_report/42-178/178C.pdf`.

W. M. Folkner, J. G. Williams, and D. H. Boggs. The Planetary and Lunar Ephemeris DE 421. *IPN Progress Report*, 2009b.

S. Goossens and K. Matsumoto. Determination of the lunar k2 Love Number from satellite tracking data. *Lunar and Planetary Science XXXIX*, 2008.

G. G. Havens and J. G. Beerer. Designing Mission Operations for the Gravity Recovery and Interior Laboratory Mission. In *12th International Conference on Space Operations*, Stockholm, Sweden, 2012.

W. A. Heiskanen and H. Moritz. *Physical Geodesy*. W. H. Freeman, San Francisco, 1967.

T. Hoffman, C. E. Bell, and H. W. Price. Systematic reliability improvements on the GRAIL project. In *Aerospace Conference, 2010 IEEE*, 2010.

B. Hofmann-Wellenhof, K. Legat, and M. Wieser. *Navigation - principles of positioning and guidance*. Springer, Wien New York, 2003.

K. H. Ilk. *Ein Beitrag zur Dynmaik ausgedehnter Körper - Gravitationswechselwirkungen*. Band 228 der Reihe C. Deutsche Geodätische Kommission, München, 1983a.

D. Kahan. GRAIL DATA PRODUCT SOFTWARE INTERFACE SPECIFICATION. JPL D-76383, Version 1.1, California Institute of Technology, 2012. `http://pds-geosciences.wustl.edu/grail/grail-l-lgrs-3-cdr-v1/grail_0101/document/dpsis.pdf`.

W. M. Kaula. *Theory of Satellite Geodesy - Applications of Satellites to Geodesy*. Dover Publications, 2000.

K. R. Koch and J. Kusche. Regularization of geopotential determination from satellite data by variance components. *Journal of Geodesy*, 76(5):641–652, 2001.

A. S. Konopliv, A. B. Binder, L. L. Hood, A. B. Kucinskas, W. L. Sjogren, and J. G. Williams. Improved gravity field of the Moon from Lunar Prospector. *Science*, 281:1476–1480, 1998.

A. S. Konopliv, R. S. Park, D. N. Yuan, S. W. Asmar, M. M. Watkins, J. G. Williams, E. Fahnestock, G. Kruizinga, M. Paik, D. Strekalov, N. Harvey, D. E. Smith, and M. T. Zuber. The JPL Lunar Gravity Field to Spherical Harmonic Degree 660 from the GRAIL Primary Mission. *Journal of Geophysical Research: Planets*, 118(4), 2013.

LRO Project. *A Standardized Lunar Coordinate System for the Lunar Reconnaissance Orbiter and Lunar Datasets*, 2008. LRO Project and LGCWG White Paper. Version 5. available online at `http://lunar.gsfc.nasa.gov/library/LunCoordWhitePaper-10-08.pdf`.

T. Mayer-Gürr. *Gravitationsfeldbestimmung aus der Analyse kurzer Bahnbögen am Beispiel der Satellitenmission CHAMP und GRACE*. PhD thesis, Institut für Geodäsie und Geoinformation 9, University of Bonn, 2006.

E. Mazarico, D. D. Rowlands, G. A. Neumann, D. E. Smith, M. H. Torrence, F. G. Lemoine, and M. T. Zuber. Orbit determination of the Lunar Reconnaissance Orbiter. *Journal of Geodesy*, 86:193–207, 2012.

O. Montenbruck and E. Gill. *Satellite Orbits - Models, Methods, and Applications*. Springer, Berlin Heidelberg New York, 2nd corrected edition, 2001.

P. M. Muller and W. L. Sjogren. Mascons: Lunar Mass Concentrations. *Science*, 161(3842): 680–684, 1968.

N. Namiki, T. Iwata, K. Matsumoto, H. Hanada, H. Noda, S. Goossens, M. Ogawa, N. Kawano, K. Asari, S. I. Tsuruta, Y. Ishihara, Q. Liu, F. Kikuchi, T. Ishikawa, S. Sasaki, C. Aoshima, K. Kurosawa, S. Sugita, and T. Takano. Farside Gravity Field of the Moon from Four-Way Doppler Measurements of SELENE (Kaguya). *Science*, 323(5916):900–905, 2009.

NASA Press Kit. *Gravity Recovery and Interior Laboratory (GRAIL) Launch*, 2011. available online at `http://www.jpl.nasa.gov/news/press_kits/graiLaunch.pdf`.

R. Olds. LIB-10: ACS Hardware Coordinate Frame Definitions and Transformations. GRA-AC-09-0013, Lockheed Martin, 2009. available online at `http://pds-geosciences.wustl.edu/grail/grail-l-lgrs-3-cdr-v1/grail_0101/document/lib_10_grail_coord_trans_rev1.pdf`.

R. S. Park, S. W. Asmar, E. G. Fahnestock, A. S. Konopliv, W. Lu, and M. M. Watkins. Gravity Recovery and Interior Laboratory Simulations of Static and Temporal Gravity Field. *Journal of Spacecraft and Rockets*, 49(2):390–400, 2012.

G. Petit and B. Luzum. IERS conventions (2010). IERS technical note No. 36, International Earth Rotation und Reference Systems Service (IERS), 2010.

R. B. Roncoli. Lunar Constants and Models Document. *JPL Technical Document D-32296*, 2005.

M. Schneider. A General Method of Orbit Determination. *Library Translation*, 1968. Band 1279, Royal Aircraft Establishment, Ministry of Technology, Farnborough, England.

G. Seeber. *Satellite geodesy - Foundations, Methods, and Applications*. de Gruyter, Berlin New York, 1989.

P. K. Seidelmann. *Explanatory Supplement to the Astronomical Almanac*. University Science Books, 1992.

S. R. Spath. Small Spacecraft Design for the GRAIL Mission. In *26th Annual AIAA/USU Conference on Small Satellites*, 2012.

D. B. Taylor, S. A. Bell, J. L. Hilton, and A. T. Sinclair. NAO TECHNICAL NOTE, No. 74. Technichal note, HM Nautical Almanac Office, 2010.

M. A. Wieczorek, G. A. Neumann, F. Nimmo, W. S. Kiefer, G. J. Taylor, H. J. Melosh, R. J. Phillips, S. C. Solomon, J. C. Andrews-Hanna S. W. Asmar, A. S. Konopliv, F. G. Lemoine, D. E. Smith, M. M. Watkins, J. G. Williams, and M. T. Zuber. The Crust of the Moon as Seen by GRAIL. *Science*, 339:671–675, 2013.

J. G. Williams, D. H. Boggs, and W. M. Folkner. DE421 Lunar Orbit, Physical Librations, and Surface Coordinates. Technical report, JPL, California Institute of Technology, 2008.

J. G. Yan, F. Li, and W. Wang. Analyzing the character of lunar gravity field by LP165P model and its effect on lunar satellite orbit. *Chinese Journal of Geophysics*, 49(2):348–355, 2006.

M. T. Zuber, D. E. Smith, L. Alkalai, D. H. Lehman, and M. M. Watkins. Outstanding Questions on the internal structure and thermal evolution of the Moon and future prospects from the GRAIL mission. In *Abstracts of Papers Submitted to the Lunar and Planetary Science Conference*, 2008. Thirty-ninth lunar and planetary science; Houston, TX, United States. Abstract 1074.

M. T. Zuber, D. E. Smith, M. M. Watkins, S. W. Asmar, A. S. Konopliv, F. G. Lemoine, H. J. Melosh, G. A. Neumann, R. J. Phillips, S. C. Solomon, M. A. Wieczorek, J. G. Williams, S. J. Goossens, G. Kruizinga, E. Mazarico, R. S. Park, and D. N. Yuan. Gravity Field of the Moon

from the Gravity Recovery and Interior Laboratory (GRAIL) Mission. *Science*, 339:668–671, 2013.